FIRST-PRINCIPLES STUDY ON THE PERFORMANCE OF TRANSITION METAL DECORATED V_2CO_2 AS CATHODE MATERIALS OF ALUMINUM-SULFUR BATTERIES

PAKUNA PANBO

มหาวิทยาลัยเทคโนโลยีสุรนารี

A Thesis Submitted in Partial Fulfillment of the Requirements for the
Degree of Master of Science in Chemistry
Suranaree University of Technology
Academic Year 2025

การศึกษาประสิทธิภาพของ V_2CO_2 ที่เสริมด้วยโลหะทรานซิสชันเพื่อเป็นวัสดุแคโทดของแบตเตอรีชนิดอลูมิเนียมซัลเฟอร์ด้วยวิธีคำนวณเฟิร์สต์พรินซิเพิล

นายปคุณา ปานโบว์

มหาวิทยาลัยเทคโนโลยีสุรนารี

วิทยานิพนธ์นี้เป็นส่วนหนึ่งของการศึกษาตามหลักสูตรปริญญาวิทยาศาสตรมหาบัณฑิต
สาขาวิชาเคมี
มหาวิทยาลัยเทคโนโลยีสุรนารี
ปีการศึกษา 2568

FIRST-PRINCIPLES STUDY ON THE PERFORMANCE OF TRANSITION METAL DECORATED V_2CO_2 AS CATHODE MATERIALS OF ALUMINUM-SULFUR BATTERIES

Suranaree University of Technology has approved this submitted in partial fulfillment of the requirements for the Degree of Master of Science.

Thesis Examining Committee

(Dr. Anchalee Junkaew)
Chairperson

(Assoc. Prof. Dr. Suwit Suthirakun)
Member (Thesis Advisor)

(Prof. Dr. Kritsana Sagarik)
Member

(Assoc. Prof. Dr. Anyanee Kamkaew)
Member

(Assoc. Prof. Dr. Kamonwad Ngamcheua)
Member

(Assoc. Prof. Dr. Yupaporn Ruksakulpiwat)
Acting Vice-Rector for Academic Affairs
and Quality Assurance

(Prof. Dr. Santi Maensiri)
Acting Dean of Institute of Science

มหาวิทยาลัยเทคโนโลยีสุรนารี

ปคุณา ปานโบว์ : การศึกษาประสิทธิภาพของ V_2CO_2 ที่เสริมด้วยโลหะทรานซิสชันเพื่อเป็นวัสดุแคโทดของแบตเตอรีชนิดอลูมิเนียมซัลเฟอร์ด้วยวิธีคำนวณเฟิร์สต์พรินซิเพิล (FIRST-PRINCIPLES STUDY ON THE PERFORMANCE OF TRANSITION METAL DECORATED V_2CO_2 AS CATHODE MATERIALS OF ALUMINUM-SULFUR BATTERIES).
อาจารย์ที่ปรึกษา : รองศาสตราจารย์ ดร.สุวิทย์ สุธีรากุล, 120 หน้า

คำสำคัญ : แบตเตอรี่อลูมิเนียม-ซัลเฟอร์ตัวเร่งปฏิกิริยาอะตอมเดี่ยว โลหะทรานซิชันสองมิติ MXene ทฤษฎีฟังก์ชันนอลความหนาแน่น การคำนวณหลักการแรก

แบตเตอรี่อะลูมิเนียม-ซัลเฟอร์ (Al-S) กำลังได้รับความสนใจในฐานะระบบกักเก็บพลังงานยุคใหม่ที่มีความจุสูงและคุ้มค่า จากปริมาณที่พบได้มากของอะลูมิเนียมและซัลเฟอร์ อย่างไรก็ตาม ความท้าทายที่สำคัญ โดยเฉพาะอย่างยิ่งปรากฏการณ์โพลีซัลไฟด์ชัตเติล (polysulfide shuttle effects) และศักย์ไฟฟ้าเกิน (overpotential) เป็นอุปสรรคต่อการประยุกต์ใช้งานจริงในวงกว้างและความเป็นไปได้ในเชิงพาณิชย์ ในการศึกษานี้ศักยภาพของตัวเร่งปฏิกิริยาโลหะแทรนซิชันแบบอะตอมเดี่ยว (SA) และอะตอมคู่ (DA) ที่รองรับบน V_2CO_2 MXenes ถูกศึกษาเพื่อใช้เป็นวัสดุแคโทดสำหรับแบตเตอรี่ Al-S โดยใช้การคำนวณทฤษฎีฟังก์ชันนัลความหนาแน่น (DFT) บนพื้นฐานหลักการแรกอย่างละเอียด มีการวิเคราะห์พลังงานการจับและพลังงานอันตรกิริยาของ S_8 และสปีชีส์ Al_2S_n ต่าง ๆ (Al_2S_{18}, Al_2S_{12}, Al_2S_6, Al_2S_3) อย่างเป็นระบบ และสร้างแผนภาพพลังงานอิสระกิ๊บส์ของปฏิกิริยารีดักชันซัลเฟอร์ (SRR) เพื่อทำแผนที่เส้นทางของปฏิกิริยาทั้งหมด และการวิเคราะห์การสลายตัวของอะลูมิเนียมซัลไฟด์ (Al_2S_3) ผลการศึกษาแสดงให้เห็นว่า DA@V_2CO_2 โดยเฉพาะอย่างยิ่ง d-Cr- และ d-Cr-V_O สามารถลดกำแพงพลังงานสำหรับขั้นตอนทางอิเล็กทรอนิกส์ที่สำคัญของ SRR ได้ ซึ่งช่วยเพิ่มประสิทธิภาพการเร่งปฏิกิริยาโดยรวม เมื่อเทียบกับ V_2CO_2, SA@V_2CO_2 และ DA@V_2CO_2 ซึ่งเป็นปัจจัยที่ส่งผลกระทบอย่างยิ่งต่อความแรงในการดูดซับและกลไกของปฏิกิริยา ผลการวิจัยนี้ชี้ให้เห็นว่า V_2CO_2 MXenes ที่ปรับปรุงด้วยโลหะแทรนซิชันเหล่านี้มีแนวโน้มที่ดีในการเป็นวัสดุกักเก็บซัลเฟอร์ (Sulfur hosts) ที่มีประสิทธิภาพในแบตเตอรี่ Al-S โดยช่วยปรับปรุงการรีดักชันของซัลเฟอร์และมีศักยภาพในการยับยั้งปรากฏการณ์ชัตเติล ซึ่งท้ายที่สุดจะช่วยเพิ่มประสิทธิภาพของแบตเตอรี่และอายุการใช้งานในระยะยาว

สาขาวิชาเคมี
ปีการศึกษา 2568

ลายมือชื่อนักศึกษา ปคุณา ปานโบว์
ลายมือชื่ออาจารย์ที่ปรึกษา

PAKUNA PANBO : FIRST-PRINCIPLES STUDY ON THE PERFORMANCE OF TRANSITION METAL DECORATED V_2CO_2 AS CATHODE MATERIALS OF ALUMINUM-SULFUR BATTERIES. THESIS ADVISOR : ASSOC. PROF. SUWIT SUTHIRAKUN, Ph.D. 120 PP.

Keywords : Aluminum-sulfur batteries, Single-atom catalysts, MXene, Density functional theory (DFT), First-principles study

Aluminum-sulfur (Al-S) batteries are gaining significant attention as next-generation, high-capacity, cost-effective energy storage systems. However, critical challenges, most notably polysulfide shuttle effects, and high sulfur reduction energy barriers, hinder their widespread practical application and commercial viability. In this study, The potential of single-atom (SA) and dual-atom (DA) transition metal catalysts supported on V_2CO_2 MXenes were investigated as cathode materials for Al-S batteries, using density functional theory (DFT) calculations. The study systematically analyzed the adsorption and interaction energy of S_8 and Al_2S_n species (Al_2S_{18}, Al_2S_{12}, Al_2S_6, Al_2S_3), constructed Gibbs free energy profiles of sulfur reduction reactions (SRR) to map the complete reaction pathway and the decomposition of Al_2S_3. The results demonstrate that DA@V_2CO_2, especially d-Cr- and d-Cn-V_O, significantly reduce the energy barriers for the crucial electronic step of SRR, enhancing the overall catalytic performance compared to bare, SA@V_2CO_2, DA@V_2CO_2. Our findings suggest that these 3d-transition metal decorated V_2CO_2 MXenes hold promise as good cathode materials in Al-S batteries, offering improved sulfur reduction and the adsorption strength to suppress the shuttle effect, enhancing long-term battery performance and cycle life.

School of Chemistry
Academic Year 2025

Student's Signature ปคุณา ปานโบว์
Advisor's Signature

ACKNOWLEDGEMENTS

I would like to express my appreciation to my thesis advisor, Assoc. Prof. Dr. Suwit Suthirakun, for his patience, kind support, guidance, discussion, and encouragement throughout this thesis. I am deeply grateful for his mentorship, which has been essential to my development as both a professional and a person In addition, I would like to thank the members of my thesis committee, including Dr. Anchalee Junkaew, Prof. Dr. Kritsana Sagarik, Assoc. Prof. Dr. Anyanee Kamkaew, and Assoc. Prof. Dr. Kamonwad Ngamcheua, for their contributions, which refined this research. Furthermore, I thank to the Development and Promotion of Science and Technology Talents Project (DPST, THAILAND) for granting me the scholarship that made my master's degree program possible. I am also thankful to the NSTDA Supercomputer Center (ThaiSC) and the Institute of Science, Suranaree University of Technology, for providing access to computational resources, which were necessary for the success of this research. I extend my appreciation to the faculty and staff of the School of Chemistry, Institute of Science, Suranaree University of Technology, for their guidance throughout my academic journey. Special thanks go to Lappawat Ngamwongwan and Wongsathorn Kaewraung for their valuable time spent teaching and suggestions on computational techniques. I am also grateful to my friends and alumni in the Computational Materials Science and Catalysis (COMSCAT) Group for their assistance and friendship. Finally, I would like to express my thanks to my family, Nadia, Salmonz the cat, and my friends for their love, kind support, and encouragement.

Pakuna Panbo

มหาวิทยาลัยเทคโนโลยีสุรนารี

CONTENTS

Page

ABSTRACT IN THAI I

ABSTRACT IN ENGLISH II

ACKNOWLEDGEMENTS III

CONTENTS IV

LIST OF TABLES VII

LIST OF FIGURES VIII

LIST OF ABBREVIATIONS XII

CHAPTER

I INTRODUCTION 1

1.1 Research objectives 4

1.2 Scope and limitation of the study 5

1.3 References 6

II LITERATURE REVIEW 9

2.1 Aluminum-sulfur batteries 12

2.2 Cathode materials for Al-S batteries 13

2.3 MXene for metal-sulfur batteries 18

2.4 Single atom as catalyst on MXenes 23

2.4.1 Adsorption on the surface 23

2.4.2 Anchoring at the metal vacancies 25

2.4.3 Anchoring at the T Vacancies 26

2.5 The studies of suppression of shuttle effect for metal-sulfur batteries 29

2.6 The studies of sulfur reduction reaction and conversion of small polysulfides for metal-sulfur batteries 30

2.7 References 32

CONTENTS (Continued)

Page

III COMPUTATIONAL DETAILS 40

3.1 Schrödinger equation for many particles 41

3.2 Density functional theory 42

3.2.1 The Hohenberg-Kohn theorems 43

3.2.2 The Kohn-Sham equation 44

3.2.3 Exchange-correlation functional 46

3.2.4 Pseudopotential and wavefunction 48

3.2.5 Self-consistent field approach 50

3.3 Geometry optimization 51

3.4 vdW correction 52

3.5 Climbing image-nudged elastic band method 54

3.6 Gibbs free energy (G) calculation 56

3.7 Smooth Overlap of Atomic Positions (SOAP) 58

3.8 Crystal orbital Hamilton population (COHP) 60

3.9 Summary of computational details 61

3.10 References 63

IV INVESTIGATION OF CATHODE PERFORMANCE IN ALUMINUM-SULFUR BATTERIES: DFT, AND COMPUTATIONAL STUDY 65

4.1 The structural and electronic properties for V_2CO_2 MXene 65

4.2 Adsorption Energy of Sulfur Species (S_8, Al_2S_n) 69

4.3 Gibbs free energy profiles of sulfur reduction reactions 79

4.4 Decomposition of Al_2S_3 85

4.5 References 88

V CONCLUSIONS 90

APPENDICES 92

APPENDIX A THE CONFIGURATION AND PROPERITES FOR 3D TRANSITION METAL ATOMS DECORATED V_2CO_2 93

CONTENTS (Continued)

Page

APPENDIX B PUBLICATION AND PRESENTATION 103
CURRICULUM VITAE 104

มหาวิทยาลัยเทคโนโลยีสุรนารี

LIST OF TABLES

Table **Page**

2.1 Studied sulfur cathode materials for Al–S batteries.....14
2.2 Synthesis conditions for different MXene and their potential application.....20
2.3 Studied MXenes as Electrode Material for Batteries.....21

มหาวิทยาลัยเทคโนโลยีสุรนารี

LIST OF FIGURES

Figure **Page**

2.1 Comparison of metal-sulfur batteries and their components. (a) capacities of different metal including Li, K, Na, Mg, Al, and S in terms of gravimetric and volumetric. (b) Theoretical capacities and energy densities of each metal-sulfur batteries. (c) Comparison of abundance and cost of metal and S..... 10

2.2 Development of Li–S and Al–S batteries and expectation..... 10

2.3 The charge and discharge mechanism of Al-S batteries 11

2.4 The sulfur reduction process and key intermediates..... 12

2.5 Synthesizable elements used in MAX processes. b) The illustration of MXene synthesis process. (c) The step of etching Ti_3AlC_2 using HF etchant..... 19

2.6 Illustrations of MXene synthesis. (a) Schematic of Co–$Ti_3C_2T_x$ single-atom catalysts (SA). (b) Synthesis of Ir from nanoparticles to flattened layer and on Mo_2 TiC_2T_x. (c) The production of SA–Cu–MXene with selective etching quaternary MAX..... 24

2.7 (a) All possible binding sites of single-metal atoms on M_2C. (b) An atomistic model of transition metal (TM) on M_2C..... 25

2.8 a) Self–reduction–stabilization process for the preparation of $Pt_1/Ti_{3-x}C_2T_y$. (b) Magnified HAADF image of $Pt_1/Ti_{3-x}C_2T_y$. (c) Corresponding intensity maps. (d) Synthesis process of the SASe–Ti_3C_2. (e) Schematic representation of the Mo_2CT_x:Fe structure. 26

2.9 (a) Top view of the pristine Mo_2CO_2 sheet. (b) Side view of the optimized $M/Mo_2CO_{2\text{-sigma}}$ structure. (c) The synthesis of Cu–SA/$Ti_3C_2T_x$. (d) The synthesis of Co@V_2CO_2..... 27

2.10 Key intermediates and reduction steps of S_8 and Al_2S_n on SA@$Ti_3C_2O_2$ with Structural details and SA@$Ti_3C_2O_2$..... 28

LIST OF FIGURES (Continued)

Figure **Page**

2.11 a) The adsorption energy of Li polysulfides on 2D-$Ti_3C_2O_2$ cathode material for Li-S batteries. (b) Comparative binding energy of Al2Sn (x =6, 12, and 18) molecules with graphene, the Cu-BHT monolayer and $EMIM^+AlCl_4$ electrolyte.....30

2.12 (a) The Gibbs free energy profiles of lithium polysulfides on SA-Zn-MXene and its pristine. (b) Free energy diagram of SRR for Ga-doped SmMn2O5 (001) slab at U = 0 V and equilibrium potential (U = 2.02V). (c) SRR overpotential and rate-limiting step of SmMnMO (M = V, Mo, Fe, Cr, Mg, Ga) system..... 31

2.13 (a) The simulated decomposition pathway of Al_2S_3 on SACo@NC. (b) The calculated energy curves for the decomposition of Al_2S_3 on Gr and SATM@NC (c) Li_2S and (d) Al_2S_3 molecules on Gr, Fe-N-C and Fe-NO-C.....32

3.1 Comparison of wavefunctions in a nuclear Coulomb potential (blue) and a pseudopotential (red).....49

3.2 Flowchart showing the process of solving the Kohn-Sham equation.....50

3.3 Schematic representation of the optimization process in DFT calculations.....52

3.4 Schematic of the potential energy surface (PES) and NEB calculation, showing the initial reaction pathway (white line) and the optimized reaction pathway (black line) 56

4.1 Optimized structures of V_2CO_2 and adsorption configurations: (a) Top views of the optimized 3×3×1 V_2CO_2. (b) Possible binding sites for SA@V_2CO_2. (c) DA@V_2CO_2 configurations: d-DA (left) without oxygen vacancy and d-DA-vo (right) with surface oxygen vacancy. (c) Binding energies of SA and DA on V_2CO_2 surfaces for various transition metal.....67

4.2 Projected Density of States (PDOS) for the bare V_2CO_2 surface, SA (Co), and DA (d-Cr and d-Mn-V_O). Fermi level (E_F) is adjusted to 0 eV. Light blue, V; brown, C; red, O; sky blue, Co; neon, d-Cr; violet, d-Mn-V_O.....69

LIST OF FIGURES (Continued)

Figure **Page**

4.3 (a) Adsorption of S_8, and Al_2S_n species on the bare V_2CO_2 surface, showcasing side views of each configuration. (b) and (c) Adsorption of the same species on Fe@V_2CO_2, and Cu@V_2CO_2 with the SA positioned at the hollow O_{topV} site. And the hollow O_{topC} site respectively (d) and (e) Adsorption of the species on V_2CO_2 surfaces modified with DA configurations, both with and without oxygen vacancies (d-Cr@V_2CO_2 and d-Cr-V_O@V_2CO_2).....72

4.4 Analysis of polysulfide adsorption on bare and SA and DA systems. (a) Interaction energies (E_{int}) of large, soluble sulfur species (S_8, Al_2S_{18}, and Al_2S_{12}) on bare, SA, and DA@V_2CO_2. (b) Correlation between the interaction energy (E_{int}) and the corresponding adsorption energy (E_{ads}) and deformation energy (E_{def}) for all sulfur species across all surfaces. The species are color-coded as follows: S_8 (dark purple), Al_2S_{18} (medium blue), Al_2S_{12} (light green), Al_2S_6 (yellow green), and Al_2S_3 (yellow).....74

4.5 The relationship between charge transfer and interaction energy for Al_2S_n species. The plot shows the relationship between the calculated charge difference on the Al_2S_n species and the corresponding interaction energy (E_{int}) on the bare, SA, and DA@V_2CO_2. Each system is represented by a unique color, and each Al_2S_n species is represented by a unique marker shape, as defined in the legend.....76

4.6 Correlation between the SOAP value and the corresponding adsorption energy (E_{ads}) and charge difference for S_8 and Al_2S_n species across all surfaces. The species are color-coded as follows: S_8 (dark purple), Al_2S_{18} (medium blue), Al_2S_{12} (light green), Al_2S_6 (yellow green), and Al_2S_3 (yellow).....78

4.7 Sulfur reduction reaction (SRR) performance of the bare V_2CO_2. Gibbs free energy diagram of SRR for V_2CO_2. at U = 0 V and equilibrium potential (U = 0.83 V).....81

LIST OF FIGURES (Continued)

Figure **Page**

4.8 SRR performance of 3d-TMs as SA@V_2CO_2. Gibbs free energy diagram of the sulfur reduction reaction (SRR) for SA@V_2CO_2 at U = 0 V and at the equilibrium potential (U = 0.83 V). The diagram illustrates the energy profiles and highlights the impact of different 3d-transition metals on SRR performance.....82

4.9 SRR performance of 3d-TMs as DA@V_2CO_2 surfaces. Gibbs free energy diagram of the sulfur SRR for DA@V_2CO_2 at U = 0 V and at the equilibrium potential (U = 0.83 V).....84

4.10 (a) A comparison of the calculated limiting potential and overpotential (η^{SRR}) across all catalyst systems. (b) The relationship between the interaction energies (E_{int}) of Al_2S_{12} and Al_2S_6 and the calculated η^{SRR} on the bare, SA, and DA systems.....85

4.11 The decomposition of Al_2S_3 on bare, Cr@V_2CO_2, and Mn and Cr-@V_2CO_2 with and without V_O. (a) Schematic of S breaking and Al breaking. (b) The relative corresponding of energy with the decomposition step of Al_2S_3 in each system. (c) The correlation between energy barrier and reaction energy..... 87

มหาวิทยาลัยเทคโนโลยีสุรนารี

LIST OF ABBREVIATIONS

2D	= Two-dimensional
AIMD	= Ab initio molecular dynamics
Al_2S_n	= Aluminum polysulfide species
CI-NEB	= Climbing image-nudged elastic band
CNF	= Carbon nanofiber
COHP	= Crystal orbital Hamilton population
Cu-BHT	= Copper-benzenehexathial
DA	= Dual atom
DFT	= Density functional theory
DOS	= Density of states
E_{ads}	= Net adsorption energy
E_b	= Binding energy
E_{def}	= Deformation energy
E_{int}	= Intrinsic interaction energy
EMIM	= 1-ethyl-3-methylimidazolium
GGA	= Generalized gradient approximation
HF	= Hydrofluoric acid
ICOHP	= Integrated Crystal Orbital Hamilton Population
LDA	= Local density approximation
LIB	= Li-ion battery
MIM	= 1-butyl-3-methylimidazolium
NEB	= Nudged elastic band
NPs	= Nanoparticles
PAW	= Projector-augmented wave
PBE	= Perdew-Burke-Ernzerhof
PDOS	= Projected density of states
QM	= Quantum mechanical

มหาวิทยาลัยเทคโนโลยีสุรนารี

LIST OF ABBREVIATIONS (Continued)

S_8	= Polysulfide
SA	= Single atom
SAC	= Single-atom catalyst
SCF	= Self-consistent field
SOAP	= Smooth Overlap of Atomic Positions
SRR	= Sulfur reduction reaction
SWCNT	= Single-walled carbon nanotube
TM	= Transition metal
VASP	= Vienna Ab initio Simulation Package
vdW	= van der Waals
V_O	= Oxygen vacancy
XC	= Exchange-correlation
η^{SRR}	= Overpotential for sulfur reduction reaction s

มหาวิทยาลัยเทคโนโลยีสุรนารี

CHAPTER I

INTRODUCTION

Renewable energy, which comes from natural sources that can be replenished, such as solar, wind, hydro, geothermal, and biomass, is seen as a viable alternative for achieving development of sustainable society. Rechargeable battery technology has become a key research area in recent decades, as it enables the storage and utilization of sustainable energy sources. Presently, Li-ion batteries are used in various applications from portable electronics to electric vehicles. Nevertheless, Li-ion batteries have limitations in terms of the theoretical specific capacities and energy density (387 $Wh \cdot kg^{-1}$, 155 $mA \cdot h \cdot g^{-1}$) (Chen et al., 2021; Van der Ven et al., 2020).

Battery technologies include solid-state batteries, which offer enhanced safety and energy density, and sodium-ion batteries, noted for their abundance and cost-effectiveness. Among these, metal-sulfur batteries, such as lithium-sulfur (Li-S), sodium-sulfur (Na-S), and aluminum-sulfur (Al-S), stand out for their exceptionally high theoretical capacities and potential for low-cost manufacturing, given the global abundance of sulfur (Klimpel et al., 2022; Liu et al., 2021).

In particular, Al-S batteries have attracted attention because of the high abundance of Al in the earth's crust as well as aluminum's high theoretical gravimetric (2980 $mAh \cdot g^{-1}$) and volumetric (8046 $mAh \cdot cm^{-3}$) capacities. Furthermore, sulfur (1675 $mAh \cdot g^{-1}$) as the cathode material offers environmentally friendly and inexpensive (Akgenc et al., 2021; Klimpel et al., 2022; Smajic et al., 2020).

An Al-S battery typically consists of an aluminum metal anode, a sulfur-based cathode, and an ionic liquid electrolyte, such as a mixture of aluminum chloride

($AlCl_3$) and 1-ethyl-3-methylimidazolium chloride (EMIM) (Appiah et al., 2022; Gao et al., 2016; Xia et al., 2015). This electrolyte is crucial for enabling the electrochemical reaction while managing the interaction of Al^{3+} ions with host materials (Yang et al., 2018).

Despite this promising potential, the practical application of high-performance Al-S batteries is hindered by several critical challenges that impede performance and cyclability (Bhauriyal et al., 2020; Klimpel et al., 2022; Tu et al., 2021; F. Wang et al., 2020). Three major issues must be addressed: (1) The "shuttle effect," where soluble intermediate aluminum-polysulfides (Al_2S_n, such as Al_2S_{18}, Al_2S_{12}, Al_2S_6, and Al_2S_3) diffuse from the cathode to the anode. This continuous loss of active material results in poor coulombic efficiency and rapid capacity fading. (2) Sluggish reaction: The multi-step Sulfur Reduction Reaction (SRR) involves complex electrochemical conversions with high energy barriers. These barriers restrict the battery's rate capability, leading to low power density. (3) Difficult conversion of Al_2S_3, as the complete reduction to final, insulating discharge products and their re-oxidation are often incomplete. These insulating products can passivate the electrode surface, blocking active sites and leading to poor reversibility.

Designing suitable hosts for sulfur to address these issues has been the focus of many experimental studies. Early cathodes based on porous carbons like Ketjen black demonstrated high initial specific capacities (over 1400 $mA{\cdot}h{\cdot}g^{-1}$) but suffered by the rapid dissolution of discharged products, highlighting the need for functional hosts, not just physical confinement (Cohn et al., 2015). Performance improved with the introduction of 2D materials; for instance, a 2D-BN nanosheet composite retained over 300 $mAh{\cdot}g^{-1}$ after 250 cycles (Zhang et al., 2019). More recently, functionalized MXenes (e.g., $S@Ti_3C_2O_2$) and single-atom catalysts (e.g., Fe-SAs-NCF) have shown improved stability and polysulfide retention, demonstrating the potential of engineering materials with specific catalytic and anchoring properties (Luo et al., 2023; Zheng et al., 2022).

Alongside experimental work, computational studies based on Density Functional Theory (DFT) have been employed to screen suitable anchoring materials and calculate SRR energy barriers. However, current computational efforts are limited.

Most studies rely on strategies from the more established Li-S batteries field, often overlooking the properties of aluminum species, such as their larger ionic radii and complex solvation behavior. While specific studies have identified promising hosts, such as Cu-benzenehexathial (Cu-BHT) MOFs (Bhauriyal & Pathak, 2020) and single-atom supported $Ti_3C_2O_2$ MXene (Z. Wang et al., 2022). The field remains underexplored. There is a critical need for systematic investigations into transition metal catalysts and host materials tailored specifically for the unique chemistry of Al-S batteries

To address these challenges, our strategy focuses on O-functionalized vanadium carbide MXene (V_2CO_2). First-principles calculations in Li-S systems indicated that V_2CO_2 binds polysulfides very strongly (Zhu et al., 2023). While such strong binding can be an obstacle in Li-S systems by impeding the decomposition and further reaction of smaller polysulfides, we hypothesize this same characteristic is exceptionally promising for Al-S batteries. The high orders of Al_2S_n species are expected to likely require stronger adsorption strength for effective immobilization. However, because strong anchoring can restrict SRR. Therefore, we further propose a 3d-transition metal decorated design: the V_2CO_2 substrate will provide the powerful anchoring required to trap Al_2S_n species, while 3d-transition metal anchored to its surface will function as distinct catalytic centers to accelerate the sluggish sulfur reduction reaction. This design aims to create a host that actively manages the electrochemical conversion pathway, rather than just passively containing sulfur.

This study utilizes first-principles study to evaluate 3d-TMs decorated V_2CO_2 MXenes as cathode hosts for Al-S batteries. We examined the adsorption of S_8 and various A_2S_n species then constructed free energy diagram for the sulfur reduction reaction, and the decomposition of Al_2S_3. Specifically, we investigated the material's ability to suppress the shuttle effect through anchoring while simultaneously catalyzing the conversion of Al_2S_3. This systematic evaluation provides guidelines for the rational design of high-performance cathode materials tailored to the Al-S system.

1.1 Research objectives

The first-principles calculations are carried out to systematically investigate 3d-transition metals decorated on V_2CO_2 cathodes as anchoring materials for Al-S batteries. This study examines the structural and electronic properties of various single atom (SA) and dual atom (DA) configurations to evaluate their stability and effectiveness. Special emphasis is placed on understanding these following objectives:

(1) To evaluate the material's efficiency in suppressing the shuttle effect. This will be achieved by systematically calculating the adsorption strength of key Al_2S_n on the V_2CO_2, the SA and DA systems, thereby quantifying the anchoring strength of the host material.

(2) To investigate the catalytic enhancement of the Sulfur Reduction Reaction (SRR) kinetics. This involves constructing the Gibbs free energy profiles for the multi-step sulfur reduction pathway on the surfaces. This analysis will identify the rate-determining steps and quantify the energy barriers, providing a direct measure of the material's ability to overcome the sluggish kinetics inherent to the SRR.

(3) To assess the material's ability to promote the complete conversion of polysulfides and enhance reversibility. This objective focuses on analyzing the energy barriers for the decomposition of the final, insulating discharge product (Al_2S_3), a critical step for re-oxidation during charging. This will elucidate the material's potential to mitigate electrode passivation and the difficult conversion of low-order polysulfides.

1.2 Scope and limitation of the study

The scope of this study is focused on a systematic first principles investigation of single 3d-transition metal atoms decorated on V_2CO_2 MXenes as potential cathode host materials for Al-S batteries, employing spin-polarized Density Functional Theory (DFT) (Kohn & Sham, 1965) as implemented in the Vienna ab initio Simulation Package (VASP 6.3). The methodology uses the projector augmented wave (PAW) method for electron-ion interactions and the generalized gradient approximation (GGA) with the Perdew-Burke-Ernzerhof (PBE) functional (Blöchl, 1994; Kresse & Joubert, 1999; Perdew et al., 1996). Weak van der Waals interactions, critical for the adsorption of S_8 and Al_2S_n species, are accounted for using the Grimme DFT-D3 correction (Grimme et al., 2010,

2011). A plane-wave cutoff energy of 500 eV is used, with structural optimizations converged until the total energy difference is within 10^{-6} eV and all residual forces are below 0.02 eV/Å. The Brillouin zone is sampled using a 3x3x1 Monkhorst-Pack k-point mesh for structural relaxations and a denser 5x5x1 grid for static energy calculations, with a 20 Å vacuum applied in the z-direction (Monkhorst & Pack, 1976). The investigation includes screening 3d-transition metal (Sc-Zn except V), considering their valence electrons (V 3d4s, C 2s2p, O 2s2p, Al 3s3p, S 3s3p). The study first determines the most stable SA@V_2CO_2 structures, then systematically investigates the adsorption behaviors of Al_2S_n species and SRR. Then, selected the candidate 3d-TM atoms for DA@V_2CO_2. Finally, the energy barriers for Al_2S_3 decomposition on the most promising candidates are simulated using the climbing-image nudged elastic band (CI-NEB) method (Smidstrup et al., 2014).

This theoretical study has several inherent limitations: the GGA-PBE functional is an approximation; the calculations are performed in an idealized vacuum, neglecting the explicit, complex role of the $AlCl_3$-EMIM ionic liquid electrolyte, solvation effects, and the electrochemical double layer; the 0 K ground-state calculations do not capture full dynamic and thermal effects; and the supercell models represent an idealized, low concentration of single atoms and adsorbates. The scope is therefore focused on elucidating intrinsic material properties and catalytic mechanisms, providing a foundational screening for experimental design rather than a quantitative prediction of full-cell device performance.

1.3 References

Akgenc, B., Sarikurt, S., Yagmurcukardes, M., & Ersan, F. (2021). Aluminum and lithium sulfur batteries: a review of recent progress and future directions. *J Phys Condens Matter*, *33*(25).

Appiah, W. A., Li, H., Lampkin, J., & García-Lastra, J. M. (2022). Towards understanding aluminum sulfur batteries with imidazolium-based electrolytes: A phenomenological model. *Journal of Power Sources*, *529*.

Bhauriyal, P., Das, S., & Pathak, B. (2020). Theoretical Insights into the Charge and Discharge Processes in Aluminum–Sulfur Batteries. *The Journal of Physical Chemistry C*, *124*(21), 11317–11324.

Bhauriyal, P., & Pathak, B. (2020). Superior anchoring effect of a Cu-benzenehexathial MOF as an aluminium–sulfur battery cathode host. *Materials Advances*, *1*(9), 3572–3581.

Blöchl, P. E. (1994). Projector augmented-wave method. *Physical Review B*, *50*(24), 17953–17979.

Chen, Y., Kang, Y., Zhao, Y., Wang, L., Liu, J., Li, Y., Liang, Z., He, X., Li, X., Tavajohi, N., & Li, B. (2021). A review of lithium-ion battery safety concerns: The issues, strategies, and testing standards. *Journal of Energy Chemistry*, *59*, 83–99.

Cohn, G., Ma, L., & Archer, L. A. (2015). A novel non-aqueous aluminum sulfur battery. *Journal of Power Sources*, *283*, 416–422.

Gao, T., Li, X., Wang, X., Hu, J., Han, F., Fan, X., Suo, L., Pearse, A. J., Lee, S. B., Rubloff, G. W., Gaskell, K. J., Noked, M., & Wang, C. (2016). A Rechargeable Al/S Battery with an Ionic-Liquid Electrolyte. *Angew Chem Int Ed Engl*, *55*(34), 9898–9901.

Grimme, S., Antony, J., Ehrlich, S., & Krieg, H. (2010). A consistent and accurate ab initio parametrization of density functional dispersion correction (DFT-D) for the 94 elements H-Pu. *The Journal of Chemical Physics*, *132*(15), 154104.

Grimme, S., Ehrlich, S., & Goerigk, L. (2011). Effect of the damping function in dispersion corrected density functional theory. *Journal of Computational Chemistry*, *32*(7), 1456–1465. https://doi.org/https://doi.org/10.1002/jcc.21759

Klimpel, M., Kovalenko, M. V, & Kravchyk, K. V. (2022). Advances and challenges of aluminum-sulfur batteries. *Commun Chem*, *5*(1), 77.

Kohn, W., & Sham, L. J. (1965). Self-Consistent Equations Including Exchange and Correlation Effects. *Physical Review*, *140*(4A), A1133–A1138.

Kresse, G., & Joubert, D. (1999). From ultrasoft pseudopotentials to the projector augmented-wave method. *Physical Review B*, *59*(3), 1758–1775.

Liu, X., Li, Y., Xu, X., Zhou, L., & Mai, L. (2021). Rechargeable metal (Li, Na, Mg, Al)-sulfur batteries: Materials and advances. *Journal of Energy Chemistry*, *61*, 104–134.

Luo, Y., Wu, M., Zhang, D., Liu, J., He, Y., Zhang, W., Liu, S., Dong, Y., Xiang, C., Yang, L., Liu, H., Shu, H., Wang, X., & Chen, M. (2023). Boosted Polysulfide Conversion by Co, Mn Bimetallic-Modulated Nitrogen–Carbon Material for Advanced Lithium–Sulfur Batteries. *ACS Sustainable Chemistry & Engineering*, *11*(3), 1087–1099.

Monkhorst, H. J., & Pack, J. D. (1976). Special points for Brillouin-zone integrations. *Physical Review B*, *13*(12), 5188–5192.

Perdew, J. P., Burke, K., & Ernzerhof, M. (1996). Generalized Gradient Approximation Made Simple. *Physical Review Letters*, *77*(18), 3865–3868.

Smajic, J., Wee, S., Simoes, F. R. F., Hedhili, M. N., Wehbe, N., Abou-Hamad, E., & Costa, P. M. F. J. (2020). Capacity Retention Analysis in Aluminum-Sulfur Batteries. *ACS Applied Energy Materials*, *3*(7), 6805–6814.

Smidstrup, S., Pedersen, A., Stokbro, K., & Jónsson, H. (2014). Improved initial guess for minimum energy path calculations. *The Journal of Chemical Physics*, *140*(21), 214106.

Tu, J., Song, W. L., Lei, H., Yu, Z., Chen, L. L., Wang, M., & Jiao, S. (2021). Nonaqueous Rechargeable Aluminum Batteries: Progresses, Challenges, and Perspectives. *Chem Rev*, *121*(8), 4903–4961.

Van der Ven, A., Deng, Z., Banerjee, S., & Ong, S. P. (2020). Rechargeable Alkali-Ion Battery Materials: Theory and Computation. *Chem Rev*, *120*(14), 6977–7019.

Wang, F., Li, J., Zhao, J., Yang, Y., Su, C., Zhong, Y. L., Yang, Q.-H., & Lu, J. (2020). Single-Atom Electrocatalysts for Lithium Sulfur Batteries: Progress, Opportunities, and Challenges. *ACS Materials Letters*, *2*(11), 1450–1463.

Wang, Z., Zheng, X., Chen, A., Han, Y., Wei, L., & Li, J. (2022). Unraveling the Anchoring Effect of MXene-Supported Single Atoms as Cathodes for Aluminum–Sulfur Batteries. *ACS Materials Letters*, *4*(8), 1436–1445.

Xia, S., Zhang, X.-M., Huang, K., Chen, Y.-L., & Wu, Y.-T. (2015). Ionic liquid electrolytes for aluminium secondary battery: Influence of organic solvents. *Journal of Electroanalytical Chemistry*, *757*, 167–175.

Yang, H., Yin, L., Liang, J., Sun, Z., Wang, Y., Li, H., He, K., Ma, L., Peng, Z., Qiu, S., Sun, C., Cheng, H. M., & Li, F. (2018). An Aluminum-Sulfur Battery with a Fast Kinetic Response. *Angew Chem Int Ed Engl*, *57*(7), 1898–1902.

Zhang, K., Lee, T. H., Cha, J. H., Varma, R. S., Choi, J. W., Jang, H. W., & Shokouhimehr, M. (2019). Two-dimensional boron nitride as a sulfur fixer for high performance rechargeable aluminum-sulfur batteries. *Sci Rep*, *9*(1), 13573.

Zheng, X., Wang, Z., Li, J., & Wei, L. (2022). Binder-free S@$Ti_3C_2T_x$ sandwich structure film as a high-capacity cathode for a stable aluminum-sulfur battery. *Science China Materials*, *65*(6), 1463–1475.

Zhu, X., Ge, M., Sun, T., Yuan, X., & Li, Y. (2023). Rationalizing Functionalized MXenes as Effective Anchor Materials for Lithium-Sulfur Batteries via First-Principles Calculations. *J Phys Chem Lett*, *14*(8), 2215–2221.

มหาวิทยาลัยเทคโนโลยีสุรนารี

CHAPTER II

LITERATURE REVIEW

2.1 Aluminum-sulfur batteries

The success of lithium-ion batteries leads to the development of high-performance batteries with cost-effective and safety energy storage. Among many types of batteries, metal–sulfur batteries (Na, K, Mg, or Al) have been recently focused as promising commercial batteries which provide higher capacity than traditional ion batteries. (Klimpel et al., 2022) The high theoretical volumetric capacity of the Al anode (8046 $mAh \cdot L^{-1}$) and theoretical energy density equal to 3177 $Wh \cdot L^{-1}$ comparing to Na-S batteries (3079 $Wh \cdot L^{-1}$), Mg-S batteries (3115 $Wh \cdot L^{-1}$), and Li-S batteries (3290 $Wh \cdot L^{-1}$) as shown in Figure 2.1a and Figure 2.1b. Aluminum is the most abundant metal in the Earth's crust crust and the least expensive compared to other metal–sulfur batteries in Figure 2.1c.

For historical development of Al-S batteries, Marassi et al invented the very first Al-S batteries in the 1980s which studied sulfur in NaCl-AlCl molten electrolyte (Marassi et al., 1985; Tanemoto et al., 1982). After that, Licht and Peramunage invented Al-S batteries using an aqueous alkaline electrolyte. Due to the great potential of Li-ion batteries and Li-S batteries, the development of Al-S batteries remained untouched until 2015 shown in Figure 2.2 (Licht & Peramunage, 1993). The ionic liquid as the electrolyte for Al-S batteries represented a very high efficiency which can create rechargeable Al-S batteries (Cohn et al., 2015; X. Yu & Manthiram, 2017). After that the number of publications on Al–S batteries have increased in experimental and computational studies.

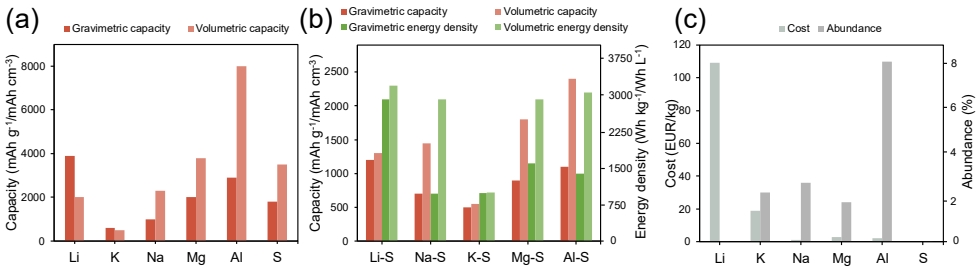


Figure 2.1 Comparison of metal-sulfur batteries and their components. (a) capacities of different metal including Li, K, Na, Mg, Al, and S in terms of gravimetric and volumetric. (b) Theoretical capacities and energy densities of each metal-sulfur batteries. (c) Comparison of abundance and cost of metal and S (Klimpel, Kovalenko et al. 2022).

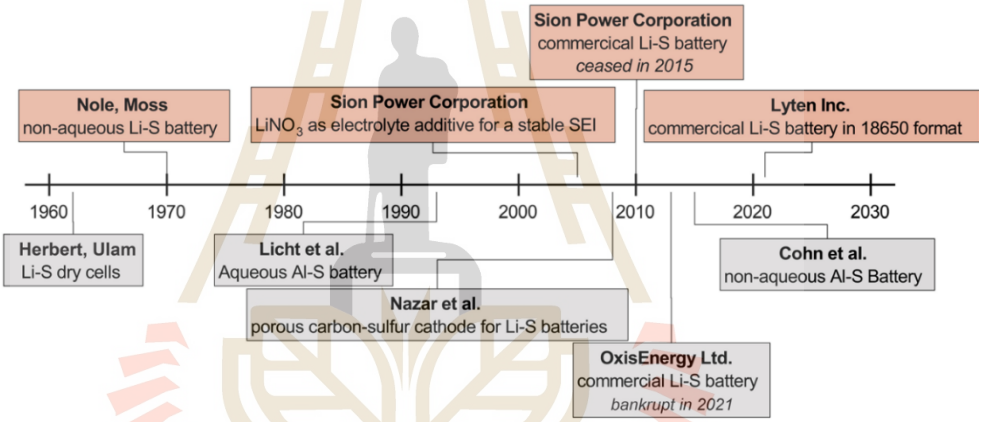


Figure 2.2 Development of Li–S and Al–S batteries and expectation (Klimpel et al., 2022).

Electrolyte of Al-S batteries normally contain chloroaluminate melts, which are the mixtures of aluminum chloride and other chlorides containing an organic cation, such as, 1-butyl-3-methylimidazolium chloride (MIM) and 1-ethyl-3-methylimidazolium chloride (EMIM). These electrolytes are called room temperature ionic liquid.

The mechanism of Al-S batteries using chloroaluminate ionic liquid electrolyte can be summarized as given equations (1) and (2). (Appiah et al., 2022; Bhauriyal et al., 2020)

$$8Al + 14AlCl_4^- \rightarrow 8Al_2Cl_7^- + 6e^- \quad (2.1)$$

$$8Al_2Cl_7^- + 6e^- + 3S \rightarrow Al_2S_3 + 14AlCl_4^- \quad (2.2)$$

During the discharge process, at the anode-electrolyte interface, Al reacts with $AlCl_4^-$ to produce $Al_2Cl_7^-$ species. Then $Al_2Cl_7^-$ species transport from the anode through the bulk electrolyte to the cathode, shown in Figure 2.3. At the cathode, solid sulfur changes into dissolved polysulfide (S_8). Then the ligand exchange reactions in which polysulfide replaces chloride ions of $Al_2Cl_7^-$ species result in the formation of aluminum polysulfide species (Al_2S_n). (Appiah et al., 2022; Bhowmik et al., 2022) This process is called sulfur reduction reaction. The key intermediates of Al_2S_n or S_8 initially start from S_8, Al_2S_{18}, Al_2S_{12}, Al_2S_6 to Al_2S_3 shown in Figure 2.4.

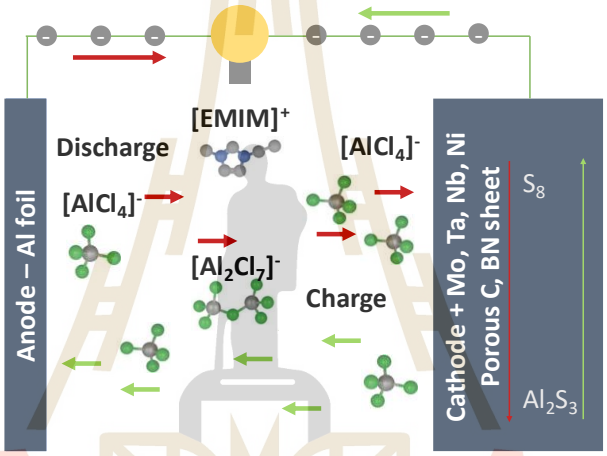


Figure 2.3 The charge and discharge mechanism of Al-S batteries.

During sulfur reduction reaction, the high orders of Al_2S_n species including Al_2S_{18}, Al_2S_{12}, Al_2S_6 prefer to dissolve into the bulk electrolyte. They could diffuse back and react with Al at the anode which is one of the main challenges in developing metal-sulfur batteries called shuttle effect. Furthermore, Al_2S_n species are difficult to change into lower order of Al_2S_n. These lead to the development of promising cathode material for Al-S batteries.

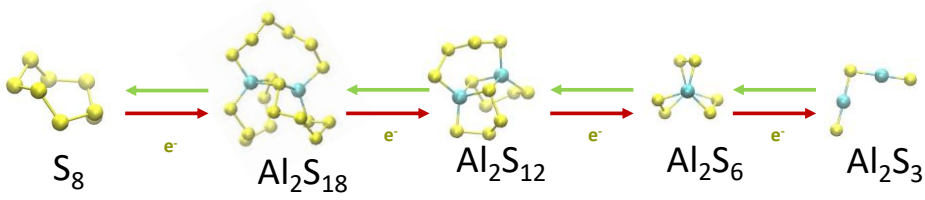


Figure 2.4 The sulfur reduction process and key intermediates.

2.2 Cathode materials for Al-S batteries

The information on the cathode materials is summarized in Table 2.1. In the initial stages of research, carbon was commonly used as cathode materials because of tunable properties, low cost, and abundance. The first cathode for rechargeable Al-S batteries made from Ketjen black carbon/S (Cohn et al., 2015). It was used as the sulfur host for the cathode because of the high surface area. The result showed a remarkably high specific capacity of more than 1400 $mA{\cdot}h{\cdot}g^{-1}$ at 30 $mA{\cdot}g^{-1}$ which is more than 80% of the theoretical capacity. However, the inability to oxidize and the dissolution of the discharged products are the obstacle in capacity decay and low cycle life of the rechargeable batteries. Other carbon materials, such as activated carbon cloth/S (Gao et al., 2016), CNF/S (X. Yu & Manthiram, 2017), SWCNT/S (Smajic et al., 2020), and Graphene/CoS_2/S (Zheng et al., 2020), are also used as cathodes. However, their performance is not remarkable, and they exhibit low discharge cycles shown in Table 2.1.

The exponential improvement of cathode materials began since 2D materials were applied in experimental studies as cathodes. For example, 2D-BN nanosheet/S/C demonstrated a high specific capacity more than 300 $mA{\cdot}h{\cdot}g^{-1}$ after 250 discharge cycle (K. Zhang et al., 2019). For other 2D materials also including SATM@NC, S@$Ti_3C_2T_x$, S @ NO-C, S @ Fe-N-C, and S@Fe-NO-C also exhibited impressive performance comparable to 2D-BN nanosheet/S/C.

For the computational studies, the DFT study proposed a 2D copper-based MOF (Cu-BHT) monolayer as a potential cathode material in Al–S batteries. It revealed the reason behind better performance of Cu-BHT than that of graphene since Cu-BHT show a better performance of suppress the high orders of Al_2S_n species (Bhauriyal & Pathak, 2020). These findings suggest that DFT can provide insightful information and details at the atomistic level. Furthermore, DFT study can cooperate with experimental study. The combination of the experimental and computational techniques used to identify the single-atom catalysts for boosted Al-S conversion reaction. Computational models play an important role in the selection of candidate materials for the synthesis. Their catalytic properties were confirmed experimentally. Among them, SACo@NC/S exhibited rate performance with a specific capacity of 485.8 $mAh{\cdot}g^{-1}$and long cycling

stability with a reversible specific capacity of 517.2 mAh·g^{-1} at 100 mA·g $^{-1}$ after 200 cycles (Ju et al., 2022).

Table 2.1 Studied sulfur cathode materials for Al–S batteries.

Materials	Synthesis or Modeling References	Initial discharge capacity ($mA{\cdot}h{\cdot}g^{-1}$)	Discharge cycle ($mA{\cdot}h{\cdot}g^{-1}$) at n cycles
Ketjen black carbon/S (2015)	Solution-processed slurry based method (Cohn et al., 2015)	1200 @ 120 $mA{\cdot}g^{-1}$	<50 after 4 cycles
S (2015)	Commercial S-powder (Xia et al., 2015)	113.64 @ 15 $mA{\cdot}g^{-1}$	104.69 after cycles
Mo_6S_8 (2015)	Chemical intercalation process (Geng et al., 2015)	148 @ 12 $mA{\cdot}g^{-1}$	70 after 50 cycles
Activated carbon cloth/S (2016)	Melt diffusion method (Gao et al., 2016)	1320 @ 50 $mA{\cdot}g^{-1}$	1000 at 20 cycles
NiS (2016)	Hydrothermal method (Z. Yu et al., 2016)	104.7 @ 200 $mA{\cdot}g^{-1}$	100 after 100 cycles

มหาวิทยาลัยเทคโนโลยีสุรนารี

Table 2.1 (Continued) Studied sulfur cathode materials for Al–S batteries.

Materials	Synthesis or Modeling References	Initial discharge capacity ($mA{\cdot}h{\cdot}g^{-1}$)	Discharge cycle ($mA{\cdot}h{\cdot}g^{-1}$) at n cycles
Ni_3S_2/graphene micro flakes (2016)	Mixing (S. Wang et al., 2016)	350 @ 100 mA g^{-1}	60 after 100 cycles
CNF/S as cathode and SWCNT coated separator (2017)	Vacuum filtration and vacuum drying (X. Yu & Manthiram, 2017)	>1200 @ 0.05 C	>450 after 10 cycles
S@CMK-3 (2018)	Melt diffusion method (H. Yang et al., 2018)	1390 @ 251 $mA{\cdot}g^{-1}$	>400 after 30 cycles
SPAN (2018)	Thermal polymerization (C. Wang et al., 2018)	343 @ 0.025 $mA{\cdot}g^{-1}$	201 after 20 cycles
2D-BN nanosheet/S/C (2019)	Ball milling mixing (K. Zhang et al., 2019)	532 @ 100 $mA{\cdot}g^{-1}$	300 after 250 cycles

มหาวิทยาลัยเทคโนโลยีสุรนารี

Table 2.1 (Continued) Studied sulfur cathode materials for Al–S batteries.

Materials	Synthesis or Modeling References	Initial discharge capacity ($mA{\cdot}h{\cdot}g^{-1}$)	Discharge cycle ($mA{\cdot}h{\cdot}g^{-1}$) at n cycles
Co_3S_4 (2019)	Solvothermal process (H. Li et al., 2019)	287.9 @ 50 $mA{\cdot}g^{-1}$	90 after 150 cycles
Carbonised-ZIF/S (2020)	Solvothermal synthesis (Hu et al., 2020)	1410 @ 200 $mA{\cdot}g^{-1}$	420 after 30 cycles
SWCNT/S (2020)	Non-destructive sublimation–deposition method (Smajic et al., 2020)	>900 @ 100 $mA{\cdot}g^{-1}$	1024 @ 2 cycles
Graphene/CoS_2/S as cathode and rGO coated separator (2020)	Melt diffusion method and hydrothermal method (Zheng et al., 2020)	680 @ 50 $mA{\cdot}g^{-1}$	1145 after 37 cycles
Cu-BHT MOF (2020)	VASP, DFT-D3 (Bhauriyal & Pathak, 2020)	Theoretical study	Theoretical study

Table 2.1 (Continued) Studied sulfur cathode materials for Al–S batteries.

Materials	Synthesis or Modeling References	Initial discharge capacity ($mA{\cdot}h{\cdot}g^{-1}$)	Discharge cycle ($mA{\cdot}h{\cdot}g^{-1}$) at n cycles
S@ZIF-67 and S@Z-67-700 (2021)	Solvothermal synthesis (Xiao et al., 2021)	1675 @ 100 $mA{\cdot}g^{-1}$ Theoretical study	180 after 50 cycles Theoretical study
SATM@NC (2022)	Mixing (Ju et al., 2022)	1097.4 @ 100 $mA{\cdot}g^{-1}$	517.2 after 200 cycles
S@$Ti_3C_2T_x$ (2022)	Conventional slurry-coating (Zheng et al., 2022)	489 @ 300 $mA{\cdot}g^{-1}$	415 after 280 cycles
($Ti_3C_2O_2$)@SA (2022)	VASP, DFT-D3 (Z. Wang et al., 2022)	Theoretical study	Theoretical study
S@NO-C, S @ Fe-N-C, S@Fe-NO-C (2023)	Solvothermal process (Luo et al., 2023)	352.1 at 300 $mA{\cdot}g^{-1}$	550.1 after 400 cycles Theoretical study

มหาวิทยาลัยเทคโนโลยีสุรนารี

2.3 MXene for as electrode material for batteries

MXene is a type of 2D material that consists of thin layers of transition metal carbides, nitrides, or carbonitrides. MXene is in $M_{n+1}X_nT_x$ form, which includes transition metals (M elements), e.g., Sc, Y, Ti, Zr, Hf, V, Nb, Ta, Cr, Mo, W, Mn, carbon, and nitrogen (X elements) along with the functional surface termination groups (T_x elements).

They can be synthesized by the selective etching of the "A" element in the MAX phase. Figure 2.5a shows elements that commonly occur in the formation of MXenes. Normally, These Strong acids such as HF, LiCl, HCl are used to etch the MAX phase resulting in the delamination of MXenes (Mahmud et al., 2022). Then, the intercalation of MXenes occurs as shown in Figure 2.5b. To achieve selective layer. Top-down processes are used to etch and exfoliate using strong acids. For example, the production of Ti_3C_2 can achieve from Ti_3AlC_2 with a top-down method shown in Figure 2.5c (Naguib et al., 2011).

The fascinating properties of MXenes are high conductivity, mechanically robust, hydrophilicity, reactivity, and corrosion resistance. These characteristics make MXenes suitable for various applications such as biosensors, antibacterial agents, catalysis, and energy storage. The table below shows the MXenes and their synthesis conditions in Table 2.

The application for energy storage has become more interesting because their metallic or narrow bandgap characteristics are highly advantageous for batteries. They are usually used as electrodes for batteries. Several studies have shown an impressive performance shown in Table 3. For examples, Ti_3C_2 nanosheet as the anode material provide an impressive initial capacity of 1112 $mA{\cdot}h{\cdot}g^{-1}$ over 2000 cycles for Na-ion batteries (R. Zhao et al., 2019). $V_2O_x@V_2CT_x$ as the cathode material provide initial capacity of 304 over 200 cycles for Zn-ion batteries (Venkatkarthick et al., 2020). For Al-S batteries, there is a study that use $Ti_3C_2T_x$ as the cathode The results show an impressive performance which provide initial capacity of 489 $mA{\cdot}h{\cdot}g^{-1}$ at 300 $mA{\cdot}g^{-1}$ and retained a value of 415 $mA{\cdot}h{\cdot}g^{-1}$ after 280 stable cycles. However, they are usually applied for metal-ion batteries. There is a long way to improve the performance of MXenes for other batteries.

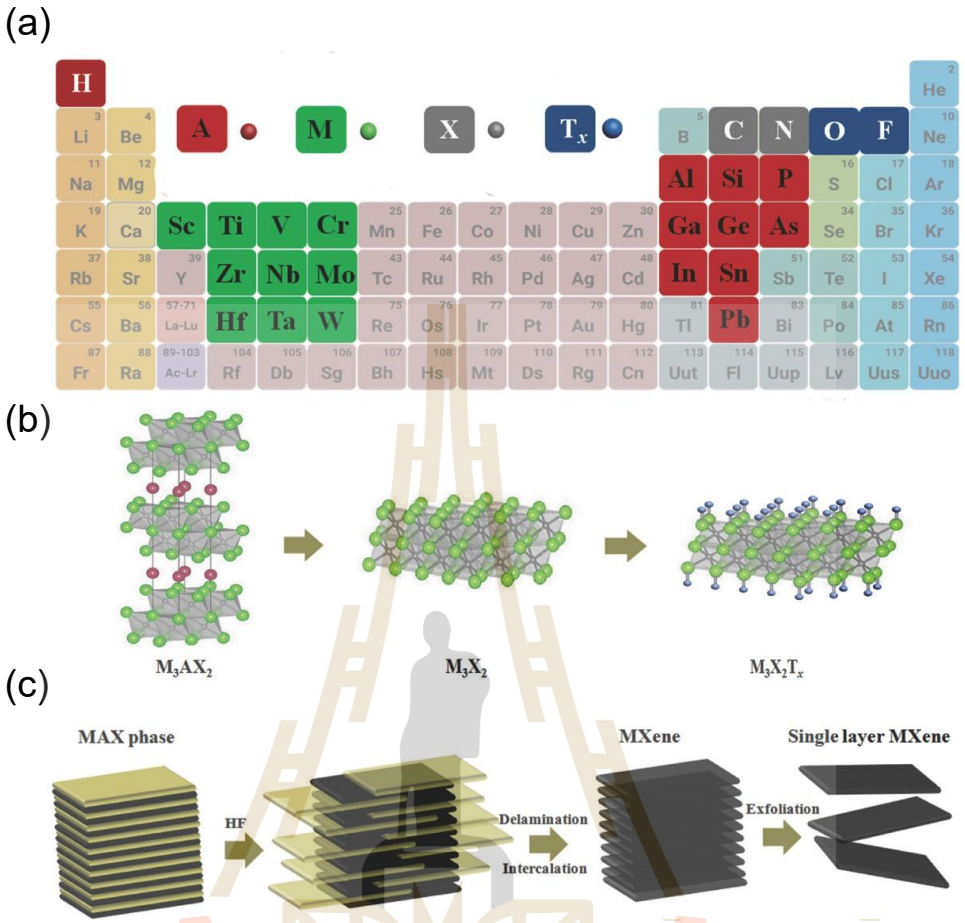


Figure 2.5 (a) Synthesizable elements used in MAX processes. b) The illustration of MXene synthesis process. (c) The step of etching Ti_3AlC_2 using HF etchant (Mahmud, Hasan et al., 2022)

มหาวิทยาลัยเทคโนโลยีสุรนารี

Table 2.2 Synthesis conditions for different MXene and their potential application.

MXene	Etchant (time, temperature)	Purpose/application	References
Nb_2C	50 wt % HF (90 h, RT)	anode material for LIB	(Naguib et al., 2013)
V_2C	50 wt % HF (90 h, RT)	anode material for LIB	(Naguib et al., 2013)
Ti_3C_2	40 wt % HF (48 h, 60 °C) + Ti3C2 calcinated high temp., 200–1200 °C	vacuum calcination for better electrochemical and thermal properties for LIB	(Lipatov et al., 2016)
Zr_3C_2	1 M NaHF2 (12 h, RT)	comparison between structural stability of $Zr_3C_2T_z$ and $Ti_3C_2T_z$ MXenes	(Zhou et al., 2016)
$(Nb,Ti)_4C_3$	50 wt % HF (90 h, 50 °C)	$Nb_4C_3T_x$ multilayer MXene for energy storage applications	(J. Yang et al., 2016)
V_2C	3.35 M NaF in 12 M HCl (48 h, 90 °C)	preparation with NaF at high temperature as anode for LIB	(Liu et al., 2017)
Ti_2C	13.5 M LiF in 6 M (15 h, 40 °C)	hybrid Li-ion battery (LIB)	(Kajiyama et al., 2017)
Nb_2C	50 wt % HF (48 h, 25 °C)	chemical sensor	(Lin et al., 2017)

มหาวิทยาลัยเทคโนโลยีสุรนารี

Table 2.2 (Continued) Synthesis conditions for different MXene and their potential application.

MXene	Etchant (time, temperature)	Purpose/application	References
Ti_3C_2	2 M HCl (24 h, 40 °C)	PH sensor	(X. Chen et al., 2018)
Ti_3C_2	40 wt % HF (24 h, RT)	Sn^{4+} ion decorated nanocomposites for LIB	(Kong et al., 2018)

มหาวิทยาลัยเทคโนโลยีสุรนารี

Table 2.3 Studied MXenes as Electrode Material for Batteries.

Structure	Battery type	electrode	Initial capacity (mAh g^{-1})	Current density (mA g^{-1})	Number of cycles	ref
$2DTi_2CT_x$ nanosheets	Li-ion	anode	1015	100	50	(Ahmed et al., 2016)
$V_2O_x@V_2CT_x$	Zn-ion	cathode	304	2	200	(Venkatkarthick et al., 2020)
SnO_2-Ti_3C_2	Li-ion	anode	1030.1	100	360	(F. Wang et al., 2017)
V_2CT_x	Al-ion	cathode	335	10	20	(VahidMohammadi et al., 2017)
PDDA-BP/Ti_3C_2 nanosheet	Na-ion	anode	1112	0.1	2000	(R. Zhao et al., 2019)
MoS_2/MXene	K-ion	anode	453.5	50	50	(J. Li et al., 2020)

มหาวิทยาลัยเทคโนโลยีสุรนารี

2.4 Single atom as catalyst on MXenes

A single-atom catalyst (SAC) is a type of catalyst that consists of isolated atoms of a metal or a non-metal on a supported substrate or an alloy. The catalysts are tunable to maximize atomic efficiency, the activity, and selectivity of catalytic reactions. The studies of SACs usually focus on metal-based catalysts, especially the late transition metals, such as Pt, Pd, Fe, Co, Ni, and Cu for their high catalytic activity and selectivity since d orbitals play an important role for their performance.

SACs work by providing active sites for chemical reactions to occur on the surface of a substrate or an alloy. The isolated atoms act as the centers of electron transfer, adsorption, and activation of the reactants and products. The substrate or the alloy supports the single atoms and stabilizes their electronic structure and geometry. The performance of single-atom catalysts depends on the type, size, and coordination of the single atoms, as well as the interaction with the substrate or the alloy (X.-F. Yang et al., 2013).

The preparation of SACs on supported materials still poses challenges due to the tendency of aggregation of single metal atoms. Two major techniques have been developed for synthesizing SACs. The first is mass-selected soft-landing techniques. These methods focus on precise control during the deposition of single metal atoms onto the support material. By carefully selecting and placing individual atoms, aggregation is minimized. The second is improved wet chemistry methods. These approaches enhance wet chemical processes to achieve better control over the placement of single metal atoms. The aim is to prevent aggregation and maintain the unique properties of SACs (N. Cheng et al., 2019).

For MXenes, SACs can be synthesized by different methods depending on the positions on MXenes including. These methods include adsorption on the surface, anchoring at the M vacancies, and anchoring at the T Vacancies.

2.4.1 Adsorption on the surface

In experimental studies, SAs on the surface of MXene are normally synthesized by electrostatic adsorption and in situ reduction in two steps (Y.-H. Chen et al., 2021). Firstly, metal cations are absorbed on the negatively charged functional groups of MXene to form ionic bonds driven by electrostatic attraction. Secondly, the metal

cations are reduced and fixed on the MXene to form covalent bonds with functional group by adding reducing agents or annealing at high temperatures. The successful of this method shows in Figure 2.6a. The presence of $NaBH_4$ avoided the excessive oxidation of MXene and leading Co^{2+} ions bond to O on MXene under the drive of electrostatic attraction.

The other efficient strategy is annealing in hydrogen atmosphere which can induce the morphologic transformation of SAs species on MXenes (Dai et al., 2022). For example, Ir species in hydrogen atmosphere can change from nanoparticles to single atoms on Mo-based MXene with the increase of annealing temperature shown in Figure 2.6b. Furthermore, there are the method that quaternary MAX phase which includes four different atoms. The sublimation of $AlCl_3$, Zhao et al. selectively etched Al from the quaternary MAX phase $Ti_3(Al_{1-x}Cu_x)C_2$, which contained a mixed A layer, and obtained Cu single atoms on the surface of MXene shown in Figure 2.6c (Q. Zhao et al., 2021).

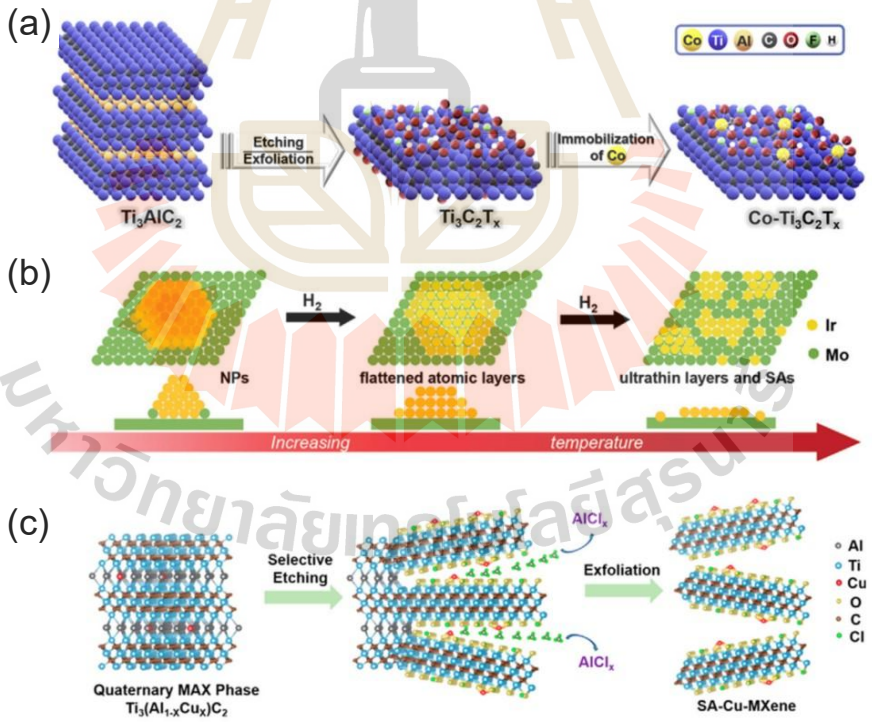


Figure 2.6 Illustrations of MXene synthesis. (a) Schematic of Co–$Ti_3C_2T_x$ single-atom catalysts (SA) (Y.-H. Chen et al., 2021). (b) Synthesis of Ir from nanoparticles to flattened layer and on Mo_2 TiC_2T_x (Dai et al., 2022). (c) The production of SA–Cu–MXene with selective etching quaternary MAX.

In computational studies, the adsorption of single atoms (SAs) mainly occurs at four possible sites: top site (T), two different hollow sites fcc and hcp, and bridge sites (B), where the sites of hcp and fcc are the preferred adsorption sites shown in Figure 2.7a and 2.7b.

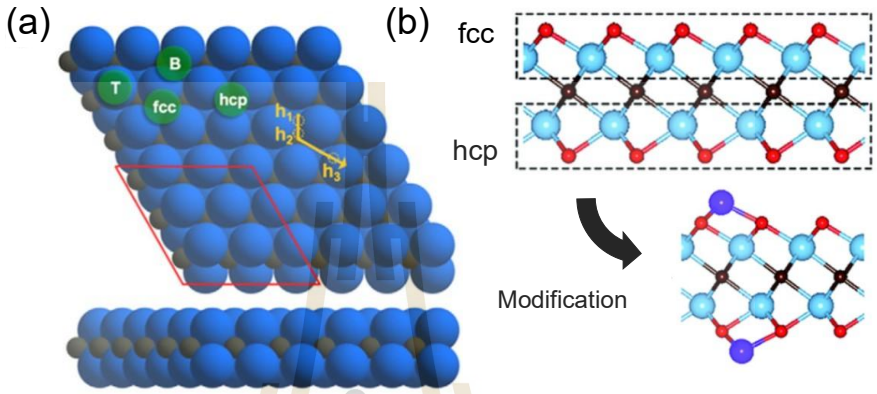


Figure 2.7 (a) All possible binding sites of single-metal atoms on M_2C. (b) An atomistic model of transition metal (TM) on M_2C.

2.4.2 Anchoring at the metal vacancies

In the synthesis process, forming metal vacancies (M vacancies) is inevitable because the surfaces normally have unsaturated coordination and certain reducibility called "self-reduction method". Zhao et al. demonstrated Pt onto the Ti vacancy of Ti-based MXene with 0.2 wt% of Pt shown in Figure 2.8a (D. Zhao et al., 2019). The Pt atom was anchored at the Ti site rather than the lattice gap. The clear Pt spots located at the lattice plane walls of the Ti columns shown in Figure 2.8b and 2.8c. The one factor that involves to the M vacancy of MXene is the concentration of etching agent and etching time. Another study from Park et al., V_2CT_x with 49% HF for 5 days can provide V vacancies that can use to anchor-isolated Pt atoms by self-reduction (Park et al., 2022). There is a study that used CO_2 atmosphere as an addition process after adsorption step. Zhao et al. demonstrated CO_2 promoted the formation of Ti vacancy and conducive Se to Ti vacancy shown in Figure 2.8d.

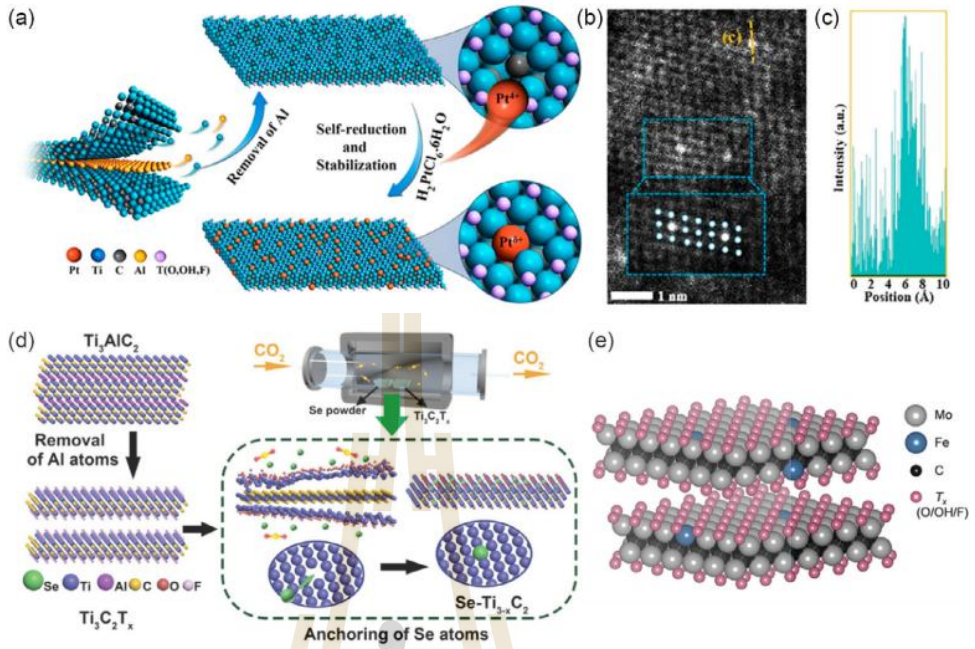


Figure 2.8 (a) Self–reduction–stabilization process for the preparation of $Pt_1/Ti_{3-x}C_2T_y$ (D. Zhao et al., 2019). (b) Magnified HAADF image of $Pt_1/Ti_{3-x}C_2Ty$. (c) Corresponding intensity maps. (d) Synthesis process of the SASe–Ti_3C_2. (e) Schematic representation of the Mo_2CT_x:Fe structure.

For computational studies, M vacancies are natural sites on MXene and can be used to anchor individual atoms. Li et al. demonstrated calculated formation energy of Zr, Hf, Ta W, Re, and Os filling on the bimetallic MXene $Mo_2TiC_2O_2$ with Mo defects, which were -1.89, -2.24, -1.64, -0.10, 1.29, and -1.96 eV, respectively (L. Li et al., 2019). The study indicates that the experimental preparation for the structures with negative formation energy is possible.

2.4.3 Anchoring at the T Vacancies

TM atoms can prefer to be anchored to T vacancies or substituted for the T atoms to form SACs. There are various methods depending on materials and the conditions. For example, Bao et al. reduced $Ti_3C_2T_x$ with $NaBH_4$, then added Cu ions to obtain Cu SA/$Ti_3C_2T_x$ by vacuum freeze-drying shown in Figure 2.9a (Bao et al., 2021). Zhao et al. added $CoCl_2$ solution in the form of ice cube to V2CTx solution and maintained the condition of 0 ℃ to ensure the slow release of Co^{2+} to avoid the formation of clusters (X. Zhao et al., 2023). The mixture was then exposed to ultraviolet light for 1 h to reduce and fix the Co onto the MXene shown in Figure 2.9b.

In computational studies, the functional groups O, F, and Cl are easy to form defects or be replaced in the reaction. The studies usually focused on oxygen vacancies because of the high stability of O terminated. The study of oxygen vacancies in $Mo_3C_2O_2$, Pd anchored onto these vacancies exhibited high stability and good CO oxidation activity (C. Cheng et al., 2018). Furthermore, the binding energy of Fe, Co, Ni, Cu, Zn, Ru, Rh, Ag, Ir, Pt, and Au atoms on the oxygen vacancies of Mo_2CO_2 was calculated by Cheng et al (C. Cheng et al., 2018). Four initial sites for anchoring TMs were calculated, including B, H1, H2, and oxygen vacancy shown in Figure 2.9c. The study revealed that TMs (except Fe) would always move to more stable oxygen vacancy during optimizations.

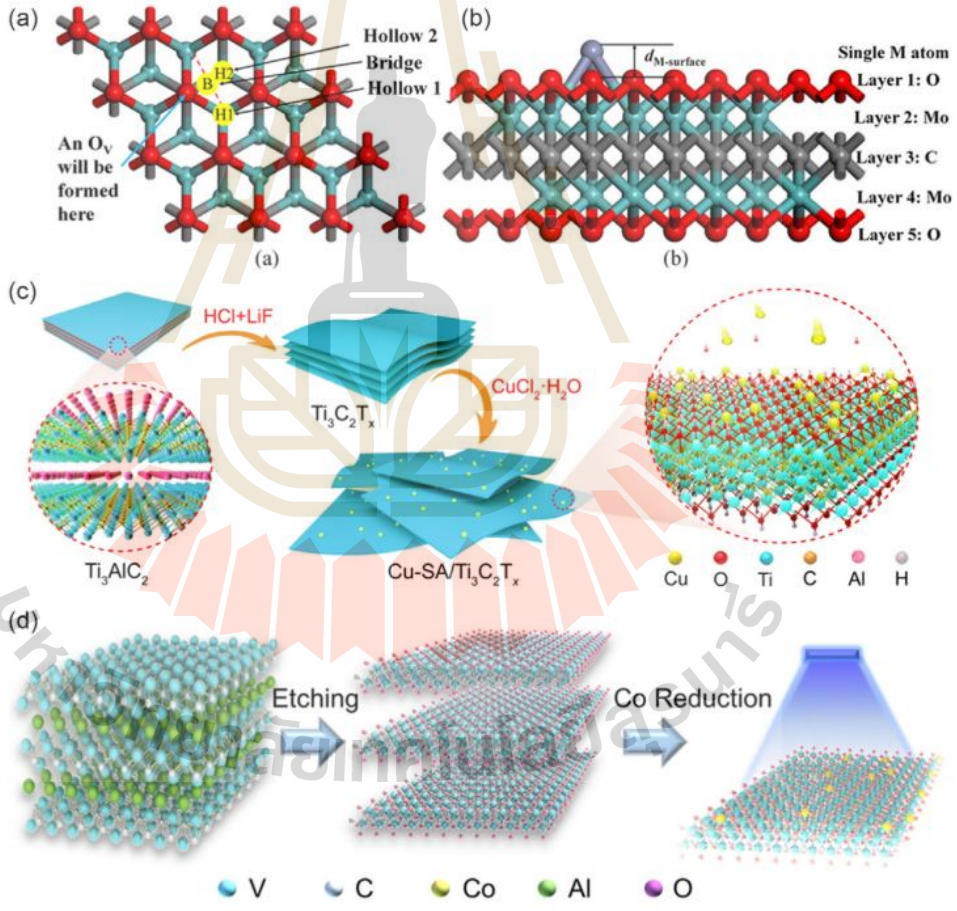


Figure 2.9 (a) Top view of the pristine Mo_2CO_2 sheet. (b) Side view of the optimized $M/Mo_2CO_{2\text{-sigma}}$ structure. (c) The synthesis of Cu–SA/$Ti_3C_2T_x$. (d) The synthesis of Co@V_2CO_2 (Bai & Guan, 2023).

For applications in energy storage, several studies demonstrate that MXene modification improves better performance in the batteries. In Li-ion batteries, Co/V_2C doubled capacity of the electrode material from 686.7 to 1117.3 mA·h·g^{-1} at 0.1 A·g^{-} (C. Wang et al., 2018). Furthermore, Sn/V_2C electrode achieved 1284.6 mA·h·g^{-1} at 0.1 A·g^{-1} for 1600 cycles (C. Wang et al., 2019) In Li-S batteries, several studies demonstrated that SAs on MXenes can inhibit the dendrite of Li. Gu et al. demonstrated that Li could form an alloying phase with Zn rather than dendrite of Li on Zn/$Ti_3C_2Cl_x$ (Gu et al., 2020). Furthermore, Zn-MXenes can improve reversible capacity and reduce the rate-limiting reaction barrier from 0.91 to 0.17 eV (D. Zhang et al., 2020).

However, there has been only one computational study on SAs-MXene for Al-S batteries. The study focused on Al-S batteries by Wang et al (Z. Wang et al., 2022). The study demonstrated that they use adsorption energy and the free energy diagram to explore and evaluate the performance of SAs on MXene. The study offered valuable insights and recommended candidate material for experimentalists shown in Figure 2.10.

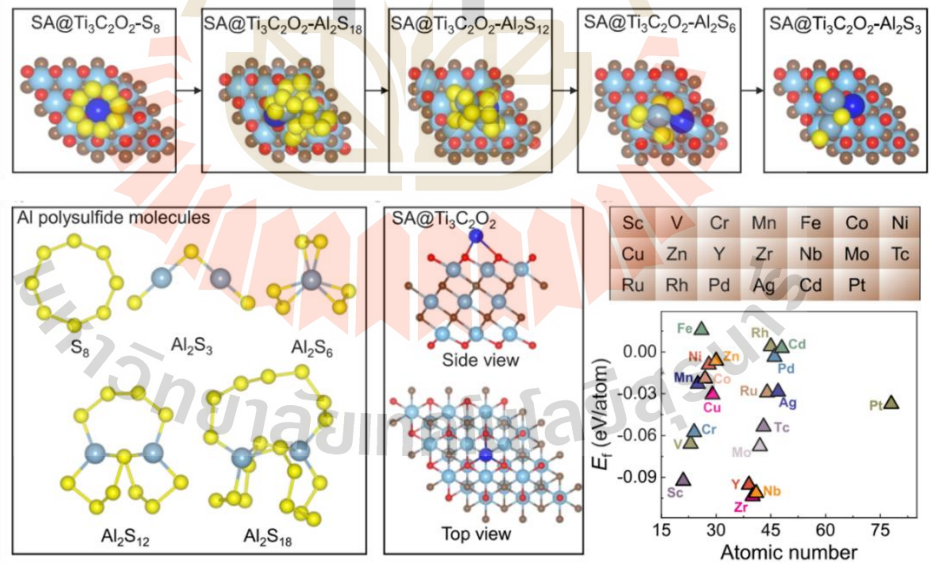


Figure 2.10 Key intermediates and reduction steps of S_8 and Al_2S_n on SA@$Ti_3C_2O_2$ with. Structural details and SA@$Ti_3C_2O_2$ (Z. Wang et al., 2022).

2.5 The studies of suppression of shuttle effect for metal-sulfur batteries

The shuttle effect is one of the main challenges in developing metal-sulfur batteries, leading to rapid capacity decay and low cycle life. The mechanism of this phenomenon occurs during the discharge process within the electrolyte. At the cathode, solid sulfur changes into dissolved polysulfide (S_8). The reduction process results in the formation of metal polysulfide species such as Li_2S_n or Na_2S_n. The key intermediates initially start from solid S_8 to large cluster of polysulfides such as Li_2S_8 and Li_2S_6 which are soluble in the electrolyte. However, these high-order species prefer to dissolve into the bulk electrolyte rather than remaining at the cathode. Driven by the concentration gradient, they could diffuse back and react with the metal anode.

This problem reduces the active material and corrodes the anode. Furthermore, the dissolved polysulfides are difficult to change into lower order insoluble sulfides. These issues result in the loss of active sulfur and poor electrochemical performance.

For computational studies, Density Functional Theory (DFT) provides insightful information and details at the atomistic level. To analyze the problem of the shuttle effect, the studies usually focus on the binding energy or adsorption energy of the polysulfide species on the cathode materials. This calculation reveals the reason behind the better performance of materials, such as the superior anchoring effect which prevents the dissolution of polysulfides. For example, the study of Li-S batteries by Wang C et. al. demonstrated that the adsorption strength of Li polysulfides on 2D-$Ti_3C_2O_2$ is stronger than that of with electrolytes including DME and DOL shown in Figure 2.11a. In the case of Al-S batteries, there is a work by Bhauriyal P. et. al that show the comparison between adsorption energy of Al_2S_n (x =6, 12, and 18) molecules with graphene, the Cu-BHT monolayer and $EMIM^+AlCl_4$ electrolyte shown in Figure 2.11b. While other computational studies normally compare graphene or their pristine model to visualize the better anchoring effect (Ju et al., 2022; Z. Wang et al., 2022; Zheng et al., 2022).

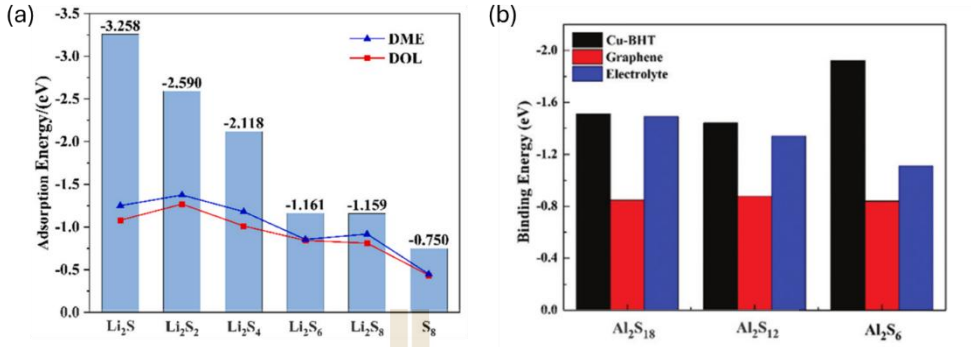


Figure 2.11 (a) The adsorption energy of Li polysulfides on 2D-$Ti_3C_2O_2$ cathode material for Li-S batteries (Dong et al., 2025). (b) Comparative binding energy of Al_2S_n (x =6, 12, and 18) molecules with graphene, the Cu-BHT monolayer and $EMIM^+AlCl_4$ electrolyte (Bhauriyal et al., 2020).

In there case of Al-S batteries, most of computational studies did not

2.6 The studies of sulfur reduction reaction and conversion of small polysulfides for metal-sulfur batteries

In studies of the sulfur reduction reaction (SRR), the conversion of small polysulfides is considered the rate-determining step in metal-sulfur batteries. The mechanism involves the transition from soluble large cluster species to insoluble solid products (such as Li_2S or Na_2S). However, the conversion of small polysulfides (such as Li_2S_2) to the final product is rather sluggish due to the high activation energy barrier and the insulating nature of the solid discharge products. This phenomenon leads to the incomplete utilization of active sulfur (often limiting capacity to 50% of the theoretical value) and the premature termination of the discharge process.

To analyze this problem, computational studies usually focus on the Gibbs free energy profile of the reduction pathway. These calculations reveal the Gibbs free energy landscape of each reaction step. For example, Zhang et al. (D. Zhang et al., 2020) demonstrated that the initial reduction of S_8 is relatively favorable with a low energy barrier, whereas the subsequent conversion of polysulfides into insoluble products represents the kinetic bottleneck with the highest energy barrier, as shown in **Figure 2.12**a. Furthermore, DFT calculations can identify the catalytic effect of host materials. The study demonstrated that the introduction of electrocatalysts could

significantly lower the dissociation energy of Li_2S_2, thereby accelerating the solid-solid conversion kinetics and improving sulfur utilization.

This method of investigating the SRR does not take the potential into account and is a common approach. However, there are a few computational studies that account for potential by using the oxygen reduction reaction as a reference (Feng et al., 2022; L. Wang et al., 2022). For example, the study by Yang et. al. examined the equilibrium, limiting potential and overpotential from SRR. The results show that there is no overpotential in electronic step of Ga doped $SmMn_2O_5$ (001) from SRR providing maximum theoretical limiting potential while there is the challenge in Li_2S desorption shown in Figure 2.12b and c. This suggests that the Ga-doped material is a promising candidate compared to other transition metals, as shown in Figure 2.12c.

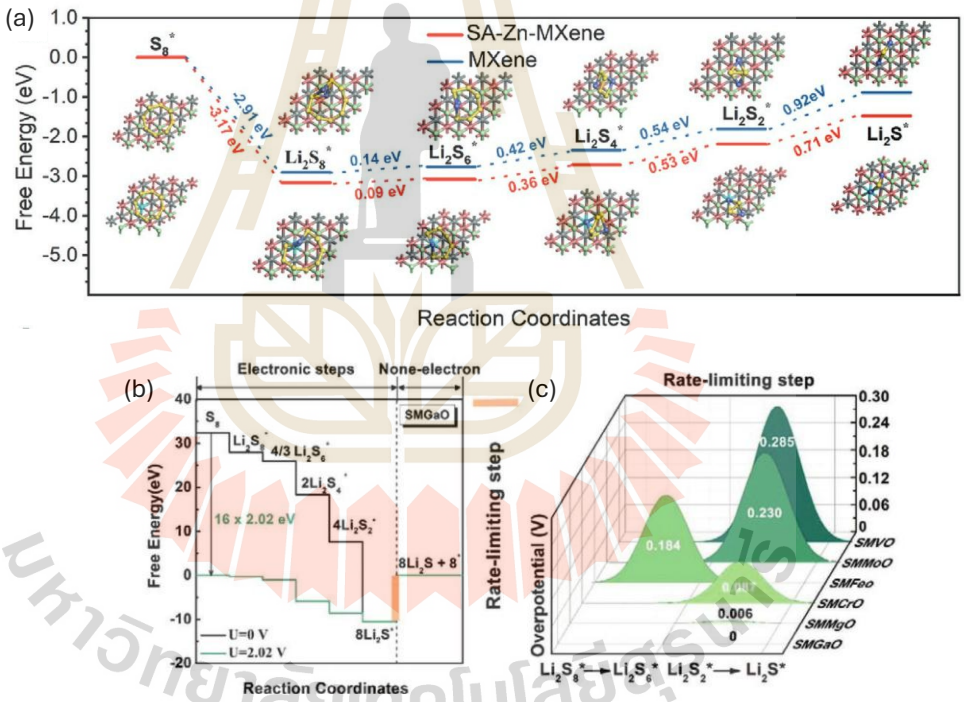


Figure 2.12 (a) The Gibbs free energy profiles of lithium polysulfides on SA-Zn-MXene and its pristine (D. Zhang et al., 2020). (b) Free energy diagram of SRR for Ga-doped $SmMn_2O_5$ (001) slab at U = 0 V and equilibrium potential (U = 2.02V). (c) SRR overpotential and rate-limiting step of SmMnMO (M = V, Mo, Fe, Cr, Mg, Ga) system.

In the case of Al-S batteries, most computational studies regarding the SRR have not taken the potential into account (Bhauriyal & Pathak, 2020; Ju et al., 2022; Z. Wang et al., 2022). This is due to the complexity of the SRR mechanism and the limited

number of studies on Al-S batteries. Regarding the decomposition of small polysulfides (Al_2S_3), We observe that they attempt to dissociate the Al atom, similar to the approach taken by the community for breaking the Li atom from Li_2S, as shown in Figure 2.13a and b. The results indicate that this reaction is thermodynamically unfavorable with high energy barriers in both Li-S and Al-S batteries (Figure 2.13c and d).

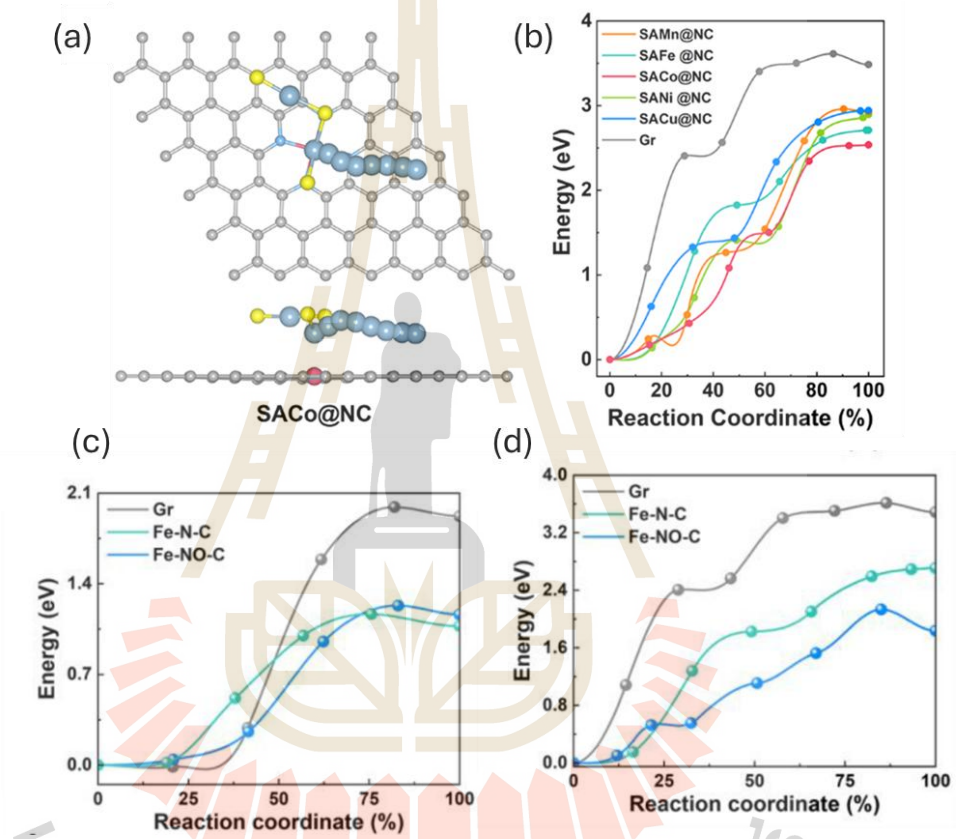


Figure 2.13 (a) The simulated decomposition pathway of Al_2S_3 on SACo@NC. (b) The calculated energy curves for the decomposition of Al_2S_3 on Gr and SATM@NC (Ju et al., 2022). (c) Li_2S and (d) Al_2S_3 molecules on Gr, Fe-N-C and Fe-NO-C (Ju et al., 2023).

2.7 References

Ahmed, B., Anjum, D. H., Hedhili, M. N., Gogotsi, Y., & Alshareef, H. N. (2016). H_2O_2 assisted room temperature oxidation of Ti_2C MXene for Li-ion battery anodes. *Nanoscale*, *8*(14), 7580–7587. https://doi.org/10.1039/C6NR00002A

Appiah, W. A., Li, H., Lampkin, J., & García-Lastra, J. M. (2022). Towards understanding aluminum sulfur batteries with imidazolium-based electrolytes: A phenomenological model. *Journal of Power Sources*, *529*.

Bai, X., & Guan, J. (2023). Applications of MXene-Based Single-Atom Catalysts. *Small Structures*, *4*(7), 2200354.

Bao, H., Qiu, Y., Peng, X., Wang, J. A., Mi, Y., Zhao, S., Liu, X., Liu, Y., Cao, R., Zhuo, L., Ren, J., Sun, J., Luo, J., & Sun, X. (2021). Isolated copper single sites for high-performance electroreduction of carbon monoxide to multicarbon products. *Nat Commun*, *12*(1), 238.

Bhauriyal, P., Das, S., & Pathak, B. (2020). Theoretical Insights into the Charge and Discharge Processes in Aluminum–Sulfur Batteries. *The Journal of Physical Chemistry C*, *124*(21), 11317–11324.

Bhauriyal, P., & Pathak, B. (2020). Superior anchoring effect of a Cu-benzenehexathial MOF as an aluminium–sulfur battery cathode host. *Materials Advances*, *1*(9), 3572–3581.

Bhowmik, A., Carrasco-Busturia, D., Jankowski, P., Raccichini, R., Garcia-Araez, N., & García-Lastra, J. M. (2022). Influence of Ionic Coordination on the Cathode Reaction Mechanisms of Al/S Batteries. *The Journal of Physical Chemistry C*, *126*(1), 40–47.

Chen, X., Sun, X., Xu, W., Pan, G., Zhou, D., Zhu, J., Wang, H., Bai, X., Dong, B., & Song, H. (2018). Ratiometric photoluminescence sensing based on Ti_3C_2 MXene quantum dots as an intracellular pH sensor. *Nanoscale*, *10*(3), 1111–1118.

Chen, Y.-H., Qi, M.-Y., Li, Y.-H., Tang, Z.-R., Wang, T., Gong, J., & Xu, Y.-J. (2021). Activating two-dimensional $Ti_3C_2T_x$-MXene with single-atom cobalt for efficient CO_2 photoreduction. *Cell Reports Physical Science*, *2*(3), 100371.

Cheng, C., Zhang, X., Wang, M., Wang, S., & Yang, Z. (2018). Single Pd atomic catalyst on Mo2CO2 monolayer (MXene): unusual activity for CO oxidation by trimolecular Eley–Rideal mechanism. *Physical Chemistry Chemical Physics*, *20*(5), 3504–3513.

Cheng, N., Zhang, L., Doyle-Davis, K., & Sun, X. (2019). Single-Atom Catalysts: From Design to Application. In *Electrochemical Energy Reviews* (Vol. 2, Issue 4, pp. 539–573). Springer Science and Business Media B.V.

Cohn, G., Ma, L., & Archer, L. A. (2015). A novel non-aqueous aluminum sulfur battery. *Journal of Power Sources*, *283*, 416–422.

Dai, L., Shen, Y., Chen, J. Z., Zhou, L., Wu, X., Li, Z., Wang, J., Huang, W., Miller, J. T., Wang, Q., Cao, A., & Wu, Y. (2022). MXene-Supported, Atomic-Layered Iridium Catalysts Created by Nanoparticle Re-Dispersion for Efficient Alkaline Hydrogen Evolution. *Small*, *18*(14), 2105226.

Dong, Y. P., Zhao, F. N., Xue, H. T., & Tang, F. L. (2025). First-principles study on electrochemical properties of 2D-$Ti_3C_2O_2$ cathode material for Li-S batteries. *Materials Today Communications*, *46*.

Feng, S., Fu, Z. H., Chen, X., Li, B. Q., Peng, H. J., Yao, N., Shen, X., Yu, L., Gao, Y. C., Zhang, R., & Zhang, Q. (2022). An Electrocatalytic Model of the Sulfur Reduction Reaction in Lithium–Sulfur Batteries. *Angewandte Chemie - International Edition*, *61*(52).

Gao, T., Li, X., Wang, X., Hu, J., Han, F., Fan, X., Suo, L., Pearse, A. J., Lee, S. B., Rubloff, G. W., Gaskell, K. J., Noked, M., & Wang, C. (2016). A Rechargeable Al/S Battery with an Ionic-Liquid Electrolyte. *Angew Chem Int Ed Engl*, *55*(34), 9898–9901.

Geng, L., Lv, G., Xing, X., & Guo, J. (2015). Reversible Electrochemical Intercalation of Aluminum in Mo_6S_8. *Chemistry of Materials*, *27*(14), 4926–4929.

Gu, J., Zhu, Q., Shi, Y., Chen, H., Zhang, D., Du, Z., & Yang, S. (2020). Single Zinc Atoms Immobilized on MXene ($Ti_3C_2Cl_x$) Layers toward Dendrite-Free Lithium Metal Anodes. *ACS Nano*, *14*(1), 891–898.

Hu, Z., Guo, Y., Jin, H., Ji, H., & Wan, L. J. (2020). A rechargeable aqueous aluminum-sulfur battery through acid activation in water-in-salt electrolyte. *Chem Commun (Camb)*, *56*(13), 2023–2026.

Ju, S., Ye, J., Zhang, H., Wang, W., Xia, G., Cui, W., Yang, Y., Pan, H., & Yu, X. (2023). Recognizing the contrasting role of N, O dual-coordinated single-atom iron catalyst in Li–S and Al–S batteries. *Energy Storage Materials*, *56*, 1–12.

Ju, S., Yuan, C., Zheng, J., Yao, L., Zhang, T., Xia, G., & Yu, X. (2022). Identifying single-atom catalysts for boosted Al–S conversion reactions. *Energy Storage Materials*, *52*, 524–533.

Kajiyama, S., Szabova, L., Iinuma, H., Sugahara, A., Gotoh, K., Sodeyama, K., Tateyama, Y., Okubo, M., & Yamada, A. (2017). Enhanced Li-Ion Accessibility in MXene Titanium Carbide by Steric Chloride Termination. *Advanced Energy Materials*, *7*(9), 1601873.

Klimpel, M., Kovalenko, M. V, & Kravchyk, K. V. (2022). Advances and challenges of aluminum-sulfur batteries. *Commun Chem*, *5*(1), 77.

Kong, F., He, X., Liu, Q., Qi, X., Zheng, Y., Wang, R., & Bai, Y. (2018). Improving the electrochemical properties of MXene Ti_3C_2 multilayer for Li-ion batteries by vacuum calcination. *Electrochimica Acta*, *265*, 140–150.

Li, H., Yang, H., Sun, Z., Shi, Y., Cheng, H.-M., & Li, F. (2019). A highly reversible Co_3S_4 microsphere cathode material for aluminum-ion batteries. *Nano Energy*, *56*, 100–108.

Li, J., Rui, B., Wei, W., Nie, P., Chang, L., Le, Z., Liu, M., Wang, H., Wang, L., & Zhang, X. (2020). Nanosheets assembled layered MoS_2/MXene as high performance anode materials for potassium ion batteries. *Journal of Power Sources*, *449*, 227481.

Li, L., Wang, X., Guo, H., Yao, G., Yu, H., Tian, Z., Li, B., & Chen, L. (2019). Theoretical Screening of Single Transition Metal Atoms Embedded in MXene Defects as Superior Electrocatalyst of Nitrogen Reduction Reaction. *Small Methods*, *3*(11), 1900337.

Licht, S., & Peramunage, D. (1993). Novel Aqueous Aluminum/Sulfur Batteries. *Journal of The Electrochemical Society*, *140*(1), L4. https://doi.org/10.1149/1.2056120

Lin, H., Gao, S., Dai, C., Chen, Y., & Shi, J. (2017). A Two-Dimensional Biodegradable Niobium Carbide (MXene) for Photothermal Tumor Eradication in NIR-I and NIR-II Biowindows. *Journal of the American Chemical Society*, *139*(45), 16235–16247.

Lipatov, A., Alhabeb, M., Lukatskaya, M. R., Boson, A., Gogotsi, Y., & Sinitskii, A. (2016). Effect of Synthesis on Quality, Electronic Properties and Environmental Stability of Individual Monolayer Ti3C2 MXene Flakes. *Advanced Electronic Materials*, *2*(12), 1600255.

Liu, F., Zhou, J., Wang, S., Wang, B., Shen, C., Wang, L., Hu, Q., Huang, Q., & Zhou, A. (2017). Preparation of High-Purity V_2C MXene and Electrochemical Properties as Li-Ion Batteries. *Journal of The Electrochemical Society*, *164*(4), A709.

Luo, Y., Wu, M., Zhang, D., Liu, J., He, Y., Zhang, W., Liu, S., Dong, Y., Xiang, C., Yang, L., Liu, H., Shu, H., Wang, X., & Chen, M. (2023). Boosted Polysulfide Conversion by Co, Mn Bimetallic-Modulated Nitrogen–Carbon Material for Advanced Lithium–Sulfur Batteries. *ACS Sustainable Chemistry & Engineering*, *11*(3), 1087–1099.

Mahmud, S. T., Hasan, M. M., Bain, S., Rahman, S. T., Rhaman, M., Hossain, M. M., & Ordu, M. (2022). Multilayer MXene Heterostructures and Nanohybrids for Multifunctional Applications: A Review. *ACS Materials Letters*, *4*(6), 1174–1206.

Marassi, R., Laher, T. M., Trimble, D. S., & Mamantov, G. (1985). Electrochemical and Spectroscopic Studies of Sulfur in Aluminum Chloride-N(n-Butyl)Pyridinium Chloride. *Journal of The Electrochemical Society*, *132*(7), 1639.

Naguib, M., Halim, J., Lu, J., Cook, K. M., Hultman, L., Gogotsi, Y., & Barsoum, M. W. (2013). New Two-Dimensional Niobium and Vanadium Carbides as Promising Materials for Li-Ion Batteries. *Journal of the American Chemical Society*, *135*(43), 15966–15969.

Naguib, M., Kurtoglu, M., Presser, V., Lu, J., Niu, J., Heon, M., Hultman, L., Gogotsi, Y., & Barsoum, M. W. (2011). Two-Dimensional Nanocrystals Produced by Exfoliation of Ti_3AlC_2. *Advanced Materials*, *23*(37), 4248–4253.

Park, S., Lee, Y.-L., Yoon, Y., Park, S. Y., Yim, S., Song, W., Myung, S., Lee, K.-S., Chang, H., Lee, S. S., & An, K.-S. (2022). Reducing the high hydrogen binding strength of vanadium carbide MXene with atomic Pt confinement for high activity toward HER. *Applied Catalysis B: Environmental*, *304*, 120989.

Smajic, J., Wee, S., Simoes, F. R. F., Hedhili, M. N., Wehbe, N., Abou-Hamad, E., & Costa, P. M. F. J. (2020). Capacity Retention Analysis in Aluminum-Sulfur Batteries. *ACS Applied Energy Materials*, *3*(7), 6805–6814.

Tanemoto, K., Marassi, R., Mamantov, C. B., Ogata, Y., Matsunaga, M., Wiaux, J. P., & Mamantov, G. (1982). Oxidation of Sulfur in Chloroaluminate Melts of Intermediate pCl. *Journal of The Electrochemical Society*, *129*(10), 2237.

VahidMohammadi, A., Hadjikhani, A., Shahbazmohamadi, S., & Beidaghi, M. (2017). Two-Dimensional Vanadium Carbide (MXene) as a High-Capacity Cathode Material for Rechargeable Aluminum Batteries. *ACS Nano*, *11*(11), 11135–11144.

Venkatkarthick, R., Rodthongkum, N., Zhang, X., Wang, S., Pattananuwat, P., Zhao, Y., Liu, R., & Qin, J. (2020). Vanadium-Based Oxide on Two-Dimensional Vanadium Carbide MXene (V_2O_x@V_2CT_x) as Cathode for Rechargeable Aqueous Zinc-Ion Batteries. *ACS Applied Energy Materials*, *3*(5), 4677–4689.

Wang, C., Chen, S., Xie, H., Wei, S., Wu, C., & Song, L. (2019). Atomic Sn^{4+} Decorated into Vanadium Carbide MXene Interlayers for Superior Lithium Storage. *Advanced Energy Materials*, *9*(4), 1802977.

Wang, C., Xie, H., Chen, S., Ge, B., Liu, D., Wu, C., Xu, W., Chu, W., Babu, G., Ajayan, P. M., & Song, L. (2018). Atomic Cobalt Covalently Engineered Interlayers for Superior Lithium-Ion Storage. *Advanced Materials*, *30*(32), 1802525.

Wang, F., Wang, Z., Zhu, J., Yang, H., Chen, X., Wang, L., & Yang, C. (2017). Facile synthesis SnO2 nanoparticle-modified Ti_3C_2 MXene nanocomposites for enhanced lithium storage application. *Journal of Materials Science*, *52*(7), 3556–3565.

Wang, L., Hu, Z., Wan, X., Hua, W., Li, H., Yang, Q. H., & Wang, W. (2022). Li2S4 Anchoring Governs the Catalytic Sulfur Reduction on Defective $SmMn_2O_5$ in Lithium–Sulfur Battery. *Advanced Energy Materials*, *12*(20).

Wang, S., Yu, Z., Tu, J., Wang, J., Tian, D., Liu, Y., & Jiao, S. (2016). A Novel Aluminum-Ion Battery: Al/$AlCl_3$-[EMIm]Cl/Ni_3S_2@Graphene. *Advanced Energy Materials*, *6*(13).

Wang, Z., Zheng, X., Chen, A., Han, Y., Wei, L., & Li, J. (2022). Unraveling the Anchoring Effect of MXene-Supported Single Atoms as Cathodes for Aluminum–Sulfur Batteries. *ACS Materials Letters*, *4*(8), 1436–1445.

Xia, S., Zhang, X.-M., Huang, K., Chen, Y.-L., & Wu, Y.-T. (2015). Ionic liquid electrolytes for aluminium secondary battery: Influence of organic solvents. *Journal of Electroanalytical Chemistry*, *757*, 167–175.

Xiao, X., Tu, J., Huang, Z., & Jiao, S. (2021). A cobalt-based metal-organic framework and its derived material as sulfur hosts for aluminum-sulfur batteries with the chemical anchoring effect. *Phys Chem Chem Phys*, *23*(17), 10326–10334.

Yang, H., Yin, L., Liang, J., Sun, Z., Wang, Y., Li, H., He, K., Ma, L., Peng, Z., Qiu, S., Sun, C., Cheng, H. M., & Li, F. (2018). An Aluminum-Sulfur Battery with a Fast Kinetic Response. *Angew Chem Int Ed Engl*, *57*(7), 1898–1902.

Yang, J., Naguib, M., Ghidiu, M., Pan, L.-M., Gu, J., Nanda, J., Halim, J., Gogotsi, Y., & Barsoum, M. W. (2016). Two-Dimensional Nb-Based M_4C_3 Solid Solutions (MXenes). *Journal of the American Ceramic Society*, *99*(2), 660–666.

Yang, X.-F., Wang, A., Qiao, B., Li, J., Liu, J., & Zhang, T. (2013). Single-Atom Catalysts: A New Frontier in Heterogeneous Catalysis. *Accounts of Chemical Research*, *46*(8), 1740–1748.

Yu, X., & Manthiram, A. (2017). Electrochemical Energy Storage with a Reversible Nonaqueous Room‐Temperature Aluminum–Sulfur Chemistry. *Advanced Energy Materials*, *7*(18).

Yu, Z., Kang, Z., Hu, Z., Lu, J., Zhou, Z., & Jiao, S. (2016). Hexagonal NiS nanobelts as advanced cathode materials for rechargeable Al-ion batteries. *Chem Commun (Camb)*, *52*(68), 10427–10430.

Zhang, D., Wang, S., Hu, R., Gu, J., Cui, Y., Li, B., Chen, W., Liu, C., Shang, J., & Yang, S. (2020). Catalytic Conversion of Polysulfides on Single Atom Zinc Implanted MXene toward High-Rate Lithium–Sulfur Batteries. *Advanced Functional Materials*, *30*(30), 2002471.

Zhang, K., Lee, T. H., Cha, J. H., Varma, R. S., Choi, J. W., Jang, H. W., & Shokouhimehr, M. (2019). Two-dimensional boron nitride as a sulfur fixer for high performance rechargeable aluminum-sulfur batteries. *Sci Rep*, *9*(1), 13573.

Zhao, D., Chen, Z., Yang, W., Liu, S., Zhang, X., Yu, Y., Cheong, W. C., Zheng, L., Ren, F., Ying, G., Cao, X., Wang, D., Peng, Q., Wang, G., & Chen, C. (2019). MXene ($Ti_{(3)}C_{(2)}$) Vacancy-Confined Single-Atom Catalyst for Efficient Functionalization of CO(2). *J Am Chem Soc*, *141*(9), 4086–4093.

Zhao, Q., Zhang, C., Hu, R., Du, Z., Gu, J., Cui, Y., Chen, X., Xu, W., Cheng, Z., Li, S., Li, B., Liu, Y., Chen, W., Liu, C., Shang, J., Song, L., & Yang, S. (2021). Selective Etching Quaternary MAX Phase toward Single Atom Copper Immobilized MXene ($Ti_3C_2Cl_x$) for Efficient CO2 Electroreduction to Methanol. *ACS Nano*, *15*(3), 4927–4936.

Zhao, R., Qian, Z., Liu, Z., Zhao, D., Hui, X., Jiang, G., Wang, C., & Yin, L. (2019). Molecular-level heterostructures assembled from layered black phosphorene and Ti_3C_2 MXene as superior anodes for high-performance sodium ion batteries. *Nano Energy*, *65*, 104037.

Zhao, X., Zheng, X., Lu, Q., Li, Y., Xiao, F., Tang, B., Wang, S., Yu, D. Y. W., & Rogach, A. L. (2023). Electrocatalytic enhancement mechanism of cobalt single atoms anchored on different MXene substrates in oxygen and hydrogen evolution reactions. *EcoMat*, *5*(2).

Zheng, X., Tang, R., Zhang, Y., Ma, L., Wang, X., Dong, Y., Kong, G., & Wei, L. (2020). Design of a composite cathode and a graphene coated separator for a stable room-temperature aluminum–sulfur battery. *Sustainable Energy & Fuels*, *4*(4), 1630–1641.

Zheng, X., Wang, Z., Li, J., & Wei, L. (2022). Binder-free S@$Ti_3C_2T_x$ sandwich structure film as a high-capacity cathode for a stable aluminum-sulfur battery. *Science China Materials*, *65*(6), 1463–1475.

Zhou, J., Zha, X., Chen, F. Y., Ye, Q., Eklund, P., Du, S., & Huang, Q. (2016). A Two-Dimensional Zirconium Carbide by Selective Etching of Al_3C_3 from Nanolaminated $Zr_3Al_3C_5$. *Angewandte Chemie International Edition*, *55*(16), 5008–5013.

มหาวิทยาลัยเทคโนโลยีสุรนารี

CHAPTER III

COMPUTATIONAL DETAILS

In this thesis, we used density functional theory to describe the quantum behavior of atoms, molecules, and 2D materials. To study single atom (SA) and dual atom (DA) decoration on V_2CO_2, various computational methods were employed, providing understanding for suggestions of the most suitable surface as a cathode material for Al-S batteries. This chapter provides an overview of the theoretical and computational methods used in this thesis. It begins with an introduction to the fundamentals of the Schrödinger equation for multi-particle systems (Section 3.1), followed by a detailed explanation of the core principles of DFT (Section 3.2).

Subsequently, the methodology for structural optimization, a crucial step in providing stable structures, is described in Section 3.3. To address the errors inherent in DFT calculations, techniques for error correction are discussed in Section 3.4. For studying the reaction kinetics of Al_2S_3 decomposition, the climbing image-nudged elastic band (CI-NEB) method is introduced in Section 3.5.

To further understand the sulfur reduction reaction (SRR) process with the bare and modified V_2CO_2 surfaces, Gibbs free energy (G) calculations were employed, as detailed in Section 3.6. The Smooth Overlap of Atomic Positions (SOAP) is used to gain deeper insight into the correlation between structural changes, adsorption, and deformation energy in Section 3.7. The crystal orbital Hamilton population (COHP) method, used to evaluate bond strength, is described in Section 3.8. All these methodologies were summarized in Section 3.9.

3.1 Schrödinger equation for many particles

Understanding the quantum behavior of systems with multiple particles is fundamentally grounded in the Schrödinger equation. Formulated by Erwin Schrödinger in the 1920s, this equation provides a mathematical framework for describing the wavefunctions of complex systems. The general form of the Schrödinger equation can be written

$$\hat{H}\Psi(\vec{R}_i, \vec{r_j}) = E\Psi(\vec{R}_i, \vec{r_j}) \tag{3.1}$$

The equation is an eigenvalue equation where $\hat{H}$ is the Hamiltonian operator, Ψ is the wavefunction dependent on the coordinates of nuclei ($\vec{R}_i$) and electrons ($\vec{r_j}$), and E is the energy eigenvalue of the system. The Hamiltonian operator consists of kinetic energy and potential energy terms for nuclei and electrons. Thus, the Hamiltonian can be written as

$$\begin{aligned}\hat{H} &= T_N + T_e + V_{NN} + V_{Ne} + V_{ee} \\ &= -\sum_{i=1}^{N} \frac{\hbar^2}{2M_i}\nabla_{R_i}^2 - \sum_{j=1}^{n} \frac{\hbar^2}{2m_j}\nabla_{r_j}^2 + \frac{1}{2}\sum_{i=1}^{N}\sum_{i'=1}^{N} \frac{1}{4\pi\epsilon_0}\frac{Z_i Z_{i'} e^2}{|R_i - R_{i'}|} \\ &\quad - \sum_{i=1}^{N}\sum_{j=1}^{n} \frac{1}{4\pi\epsilon_0}\frac{Z_i e^2}{|R_i - r_j|} + \frac{1}{2}\sum_{j=1}^{n}\sum_{j'=1}^{n} \frac{1}{4\pi\epsilon_0}\frac{e^2}{|r_j - r_{j'}|}\end{aligned} \tag{3.2}$$

Where T_N and T_e are kinetic energy operators of nucleus and electron, respectively. V_{NN}, V_{Ne} and V_{ee} are potential operators of nucleus-nucleus interaction, nucleus-electron interaction, and electron-electron interaction, respectively. The kinetic operators can be explained as shown in equation (3.2), including $\hbar = h/2\pi$. M_i is the mass of nucleus and m_j is mass of an electron. The potential operators consist of Z_i, R_i, and r_j which are atomic number of nuclei and position of nucleus and electrons, respectively. Solving the full Schrödinger equation with many particles is computationally challenging due to the complexity of the system. To simplify the

problem, the Born-Oppenheimer approximation (Born & Oppenheimer, 1927) is often applied. This approximation assumes that the motion of atomic nuclei and electrons occurs on vastly different time scales. Therefore, the motions of nuclei and electrons can be treated as decoupled, allowing the nuclei to be considered fixed while solving the electronic Schrödinger equation. Consequently, the Hamiltonian operator can be reduced as equation (3.3) based on the time-independent Schrödinger

$$\begin{pmatrix} -\sum_{j=1}^{n} \frac{\hbar^2}{2m_j}\nabla_{r_j}^2 & -\sum_{i=1}^{N}\sum_{j=1}^{n} \frac{1}{4\pi\epsilon_0}\frac{Z_i e^2}{|R_i - r_j|} \\ & +\frac{1}{2}\sum_{j=1}^{n}\sum_{j'=1}^{n} \frac{1}{4\pi\epsilon_0}\frac{e^2}{|r_j - r_{j'}|} \end{pmatrix} \Psi(\vec{r}_j) = E\Psi(\vec{r}_j) \qquad (3.3)$$

The Born-Oppenheimer approximation can determine electronic energy level and wavefunctions, which form the basis of calculating a wide range of molecular properties. These include bond lengths, bond angles, vibrational frequencies, and other characteristics critical to understanding molecular systems.

3.2 Density functional theory

Density functional theory (DFT) is a quantum mechanical (QM) method widely used in chemistry and physics to calculate the electronic density of atoms, as shown in equation (3.4). This theory simplifies the approximation of Schrödinger equation instead of tracking individual particles within the system., offering a more computationally efficient alternative to the Hartree-Fock method. The electron density, expressed in terms of the wavefunction, represents a fundamental connection between the DFT method and the quantum mechanical description of electronic systems:

$$\rho(\vec{r}) = \sum_i \Psi_i^*(\vec{r})\Psi_i(\vec{r}) = \sum_i |\Psi(\vec{r})|^2 \qquad (3.4)$$

where $\rho(\vec{r})$ represents the electron density at a given position $\vec{r}$, where interaction between electrons is not explicitly considered.

3.2.1 The Hohenberg-Kohn theorems

The Hohenberg-Kohn theorems (Hohenberg & Kohn, 1964a) developed by Pierre Hohenberg and Walter Kohn in 1964, are foundational principles in quantum mechanics and form the theoretical basis of DFT. The theorems consist of two key statements, often referred to as the first and second Hohenberg-Kohn theorems.

In case of first theorem, the external potential $V(r)$ uniquely determines the ground-state electron density $\rho(r)$, and vice versa. In other words, knowing the external potential allows you to determine the electron density, and knowing the electron density allows you to reconstruct the external potential. This theorem forms the basis for expressing the total energy of a quantum system as a function of electron density, $E[\rho]$, and the external potential, $V(r)$. The main goal of DFT is to suggest the electron density which minimized the total energy. This energy is ground-state electron density and energy. $\rho_0(r)$,

For the second theorem, it emphasizes the uniqueness of the ground-state electron density and the total energy of a quantum system. It describes a one-to-one correspondence between the ground-state electron density, $\rho_0(r)$, and the external potential, $V_0(r)$, which results in the same minimum value of the ground-state energy. In other words, a single ground-state electron density and its corresponding external potential uniquely minimize the total energy of the system. This relationship is mathematically represented as:

$$E[\rho_0(r)] = \frac{\partial E[\rho(r)]}{\partial \rho}|_{\rho=\rho_o(r)} = min_{\rho\to\rho_0} E[\rho(r)] \quad (3.5)$$

These theorems form the basis of DFT, which focuses on suggesting the electron density that minimizes the total energy functional of a quantum system. Although the Hohenberg-Kohn theorems do not provide a direct method for calculating the ground-state electron density, they offer a theoretical framework that ensures the accuracy and reliability of DFT in predicting the properties of many-electron systems.

3.2.2 The Kohn-Sham equation

The second Hohenberg-Kohn theorem provides the foundation for determining the ground-state energy of a quantum system by minimizing the total energy functional with respect to the electron density. In the framework of DFT, the total energy of a many-electron system is expressed as a functional of the electron density. This approach allows for the accurate prediction of ground-state properties without explicitly solving the many-body Schrödinger equation.

In the Kohn-Sham equation, a central component of DFT, the kinetic energy of electrons in a many-particle system is separated into two terms: (1) the kinetic energy of non-interacting electrons and (2) the contribution from electron-electron correlations, often referred to as the correlation effect on kinetic energy. This decomposition leads to the formulation of kinetic energy for electrons in a many-particle system as:

$$T[\rho(r)] = T_{non}[\rho(r)] + T_{cor}[\rho(r)] \tag{3.6}$$

For a system consisting of nuclei N and electrons N_e, the kinetic energy of non-interacting electrons can be represented as:

$$T_{non}[\rho(r)] = \sum_{i}^{N_e} \langle \psi_i(r) | \frac{-\nabla^2}{2} | \psi_i(r) \rangle \tag{3.7}$$

This term describes kinetic energy as if the electrons were moving independently, disregarding electron-electron interactions. However, in real systems, interactions between electrons significantly impact the total energy, necessitating the inclusion of potential energy terms. The potential energy contributions from electron-electron interactions and electron-nucleus interactions are given by:

$$V_{ee} = \langle \psi_e(r) | \frac{1}{2} \sum_{i}^{N_e} \sum_{j}^{N_e} \frac{1}{|r_i - r_j|} | \psi_e(r) \rangle = \frac{1}{2} \int \int \frac{\rho(r)\rho(r')}{|r - r'|} dr dr' \tag{3.8}$$

$$V_{Ne} = \langle \psi_e(r) | \sum_{i}^{N} \sum_{j}^{N_e} \frac{-Z_i}{|R_i - r_j|} | \psi_e(r) \rangle = -\sum_{i=1}^{N} \int \frac{Z_I \rho(r)}{|R_I - r|} dr \tag{3.9}$$

These terms encapsulate the electrostatic forces within the system. V_{ee} accounts for the repulsive interactions between electrons, while V_{Ne} describes the attractive forces between electrons and nuclei. Together, these terms are crucial for determining the system's total energy.

In the Hartree-Fock approximation, the exchange energy naturally arises from the antisymmetric nature of electron wavefunctions, a consequence of the Pauli exclusion principle. However, this approximation neglects the correlation energy, which represents the additional energy associated with the dynamic interactions between electrons. To overcome this limitation, DFT combines both the exchange and correlation energy into a single term known as the exchange-correlation energy, denoted as:

$$E_{xc}[\rho(r)] = E_x[\rho(r)] + E_c[\rho(r)] \tag{3.10}$$

This unified term allows DFT to incorporate both effects seamlessly, improving accuracy over the Hartree-Fock method. The total energy of a many-particle system in DFT is expressed as:

$$\begin{aligned} E[\rho(r)] = T_{non}[\rho(r)] + \frac{1}{2}\int\int \frac{\rho(r)\rho(r')}{|r-r'|}drdr' \\ - \sum_{i=1}^{N} \frac{Z_i\rho(r)}{|R_i - r|}dr + E_{xc}[\rho(r)] \end{aligned} \tag{3.11}$$

According to the second Hohenberg-Kohn theorem, the ground-state energy of a quantum system corresponds to the minimum value of this energy functional. The condition for achieving this minimum is given by:

$$\left[-\frac{\nabla_i^2}{2} + V_{eff}[\rho(r)]\right]\psi_i^{KS}(r) = E_i\psi_i^{KS}(r) \tag{3.12}$$

The effective potential in the Kohn-Sham equation, which governs the behavior of the electrons, can be written as:

$$\begin{aligned} V_{eff}[\rho(r)] &= V_H[\rho(r)] + V_{ext}[\rho(r)] + Vxc[\rho(r)] \\ &= \frac{1}{2}\int \frac{\rho(r')}{|r-r'|}dr' - \sum_{i=1}^{N}\frac{Z_i}{|R_i - r|} + V_{xc}[\rho(r)] \end{aligned} \tag{3.13}$$

This effective potential includes contributions from the external potential, the Hartree potential (arising from electron-electron interactions), and the exchange-correlation potential, which incorporates quantum mechanical corrections. By solving the Kohn-Sham equations iteratively, the ground-state electron density and corresponding energy of the system can be determined. This methodology makes DFT a powerful tool for studying the electronic structure of complex systems, bridging the gap between computational efficiency and physical accuracy.

3.2.3 Exchange-correlation functional

For DFT calculations, the exchange-correlation potential (XC) accounts for all quantum mechanical interactions and effects that are not included in other potentials in density functional theory (DFT). The XC operator is a critical yet challenging component of DFT because its exact form remains unknown. Although XC energy typically constitutes less than 10% of the total energy, it plays a vital role in determining the properties of materials in DFT calculations.

In the present day, various approximations of the XC functional have been proposed, including the local density approximation (LDA) and the generalized gradient approximation (GGA). The local XC energy per electron can be expressed as:

$$\varepsilon_{XC}[\rho(\vec{r})] = \frac{1}{2}\int \frac{\rho_{XC}(\vec{r},\vec{r}')}{|\vec{r}-\vec{r}'|} d\vec{r}' \tag{3.14}$$

Then

$$E_{XC}[\rho(\vec{r})] = \int \rho(\vec{r})\, \varepsilon_{XC}(\vec{r},\rho) d\vec{r} \tag{3.15}$$

For the LDA, the XC functional is exactly for a homogeneous electron gas. The XC energy for the LDA can be written as:

$$E_{XC}^{LDA}[\rho(\vec{r})] = \int \rho(\vec{r})\, \varepsilon_{XC}^{LDA}[\rho(\vec{r})] d\vec{r} \tag{3.16}$$

Nevertheless, the LDA has imitations in accurately describing systems with varying electron densities (inhomogeneous), making it less suitable for real systems with complex electronic structures. To overcome these limitations, GGA incorporates

the density gradient, allowing it to account for inhomogeneous behavior more effectively. The general formula for the XC energy in GGA is given by:

$$E_{XC}^{GGA}[\rho(\vec{r})] = \int \rho(\vec{r})\, \varepsilon_{XC}^{GGA}[\rho(\vec{r}), \nabla\rho(\vec{r})] d\vec{r} \tag{3.17}$$

GGA functionals are widely used due to their accuracy for a range of properties, inculding ground-state energies, molecular geometries, and covalent bonding. The are also well-suited for weakly bonded systems (Santra et al., 2007). Currently, several forms of GGA functionals have been developed, including PW91 (Perdew & Wang, 1992), PBE (Perdew et al., 1996). In our work, the PBE functional is mainly used due to its balance of accuracy and computational efficiency. The PBE functional can be written as:

$$\varepsilon_{XC}^{PBE}[\rho(\vec{r}), \nabla\rho(\vec{r})] = -\frac{3}{4}\left(\frac{3}{\pi}\right)^{\frac{1}{3}} n^{\frac{1}{3}}(\vec{r}) F(x) \tag{3.18}$$

where

$$F(x) = 1 + a - \frac{a}{1+bx^2}, \qquad x = \frac{|\nabla\rho(\vec{r})|}{n^{\frac{4}{3}}(\vec{r})} \tag{3.19}$$

Where a and b are constants. Substituting equation (3.19) into equation (3.20), the corresponding XC potential for PBE is:

$$V_{XC}^{PBE}[\rho(\vec{r})] = \frac{\delta E_{XC}^{PBE}[\rho(\vec{r})]}{\delta\rho(\vec{r})} \tag{3.20}$$

The PBE functional's ability to incorporate density gradients while maintaining computational simplicity makes it a popular choice for a wide range of applications in materials science and quantum chemistry.

3.2.4 Pseudopotentials

Pseudopotentials are an essential tool for simplifying complex calculations in computational chemistry. They replace the true potential of atomic nuclei with an effective potential designed to replicate the behavior of valence (outermost) electrons, while either simplifying or neglecting the contributions of tightly bound inner-core electrons. In most cases, bond formation and electronic properties are determined by valence electrons, while core electrons are treated as part of the nuclei under the frozen-core approximation. This method simplifies the description of pseudo-

wavefunctions and facilitates the practical use of plane-wave basis sets. Additionally, this simplification significantly reduces the computational cost of electronic structure calculations while maintaining accuracy for many properties of interest.

As shown in Figure 3.1, the pseudo and exact potential align when the interparticle distance exceeds the specified cutoff radius (r_c). Similarly, the pseudo (ψ_{peudo}) and exact (ψ_{exact}) wavefunctions also converge beyond this radius. Within the region below r_c , however, the exact wavefunction exhibits pronounced oscillations. These oscillations make solving the Schrödinger equation challenging, as achieving a smooth and numerically stable wavefunction in this region requires significant computational effort, as shown by the red solid line in the figure.

To overcome this issue, a smoother pseudo-wavefunction is employed, which significantly reduces computational cost while maintaining accuracy. For the pseudo wavefunction and potential to be effective, they must satisfy the following criteria: (1) Consistency: The pseudo wavefunction and potential should match the exact counterparts beyond the cutoff radius. (2) Smoothness: Within the r_c region, the pseudo wavefunction should minimize oscillations to simplify numerical calculations. (3) Transferability: The pseudopotential should accurately describe the behavior of valence electrons across various chemical environments. These requirements ensure that pseudopotentials serve as an efficient and accurate approach to simplifying electronic structure calculations (Kresse & Joubert, 1999).

มหาวิทยาลัยเทคโนโลยีสุรนารี

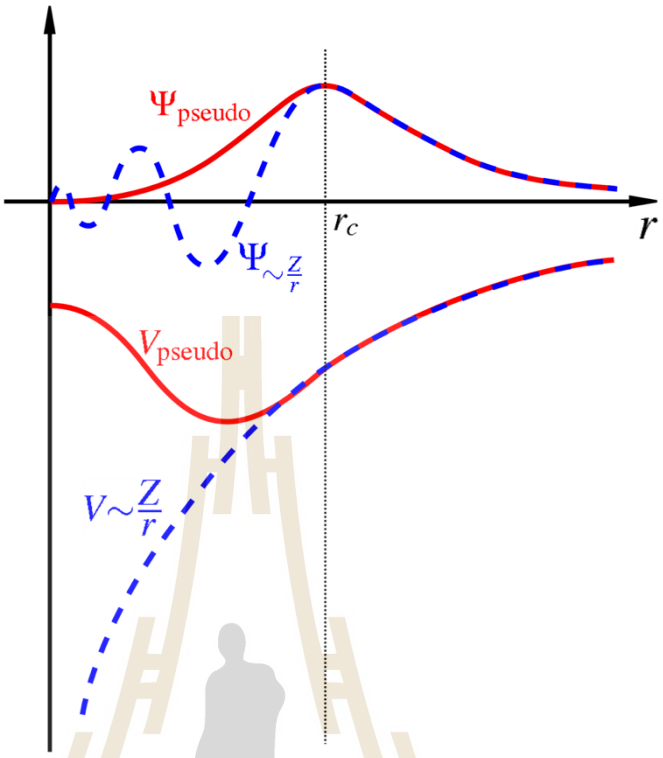


Figure 3.1 Comparison of wavefunctions in a nuclear Coulomb potential (blue) and a pseudopotential (red) (Grajcarova, 2013).

3.2.5 Self-consistent field approach

In practical DFT calculations, the ground-state energy of a many-body system is determined using a self-consistent field (SCF) method. This approach focuses on finding the lowest-energy configuration of atoms by solving the Kohn-Sham equation. Figure 3.2 presents the flowchart of this process, ensuring that the electron density and effective potential reach a stable and consistent solution.

มหาวิทยาลัยเทคโนโลยีสุรนารี

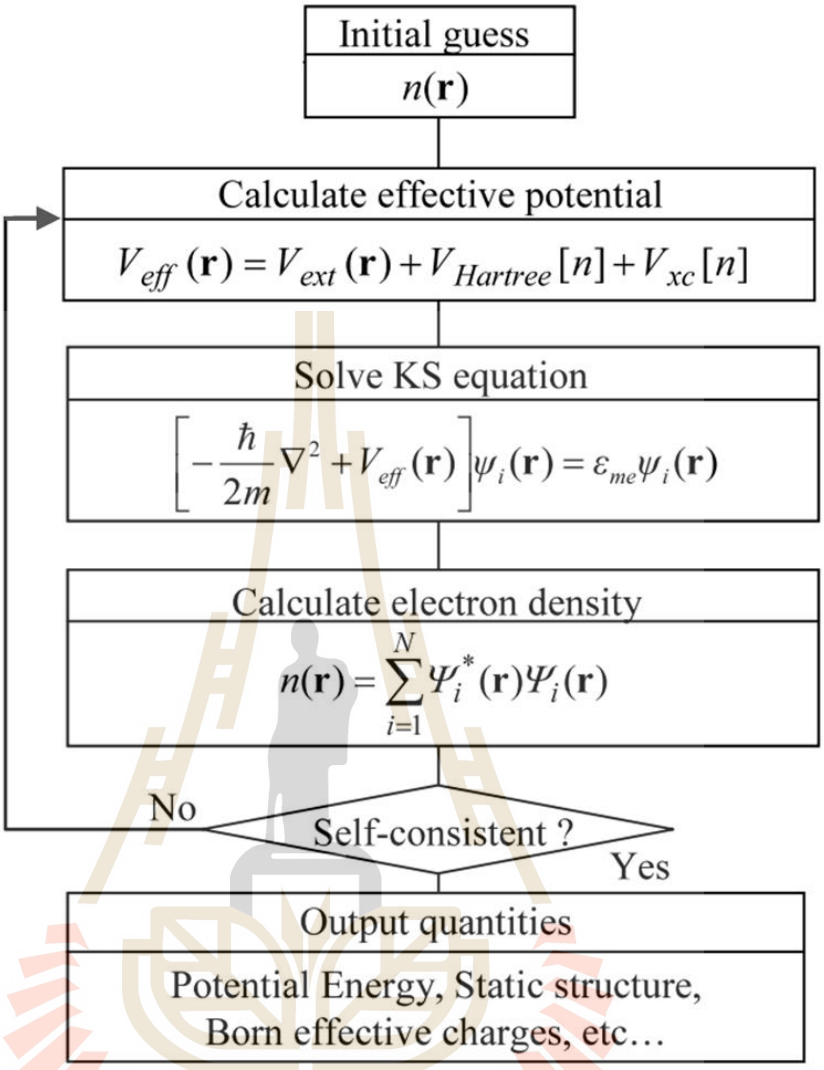


Figure 3.2 Flowchart showing the process of solving the Kohn-Sham equation (Nakamachi et al., 2013).

The SCF calculation follows a systematic process to determine the ground-state energy in density functional theory (DFT) calculations. The steps involved are as follows:

1. Initial electron density guess: make an initial assumption for the electron density
2. Effective potential calculation: compute the effective potential using the initial electron density
3. Solving the Kohn-Sham equation: Solve the Kohn-Sham equation to suggest the eigenvalues (total energy) and eigenvectors (wavefunctions)

4. New electron density calculation: Generate a new electron density based on the calculated eigenvectors (wavefunctions).
5. New energy calculation: Calculate the total electronic energy using the updated electron density in the Kohn-Sham equation
6. Energy convergence check: if the difference between the new and previous electronic energy is smaller than the predefined convergence criterion, the calculation terminates, and the resulting values are accepted. However, If the difference exceeds, update the electron density with the new values and repeat the process from step 2. This process is repeated until the calculated energy and electron density reach convergence, ensuring a consistent solution for the electron density and effective potential. In this thesis, the convergence criterion is set to 10^{-6} eV.

3.3 Geometry optimization

Geometry optimization is a critical step in DFT calculations, particularly for studying molecules and materials. The goal is to find the most energetically favorable arrangement of atoms by minimizing the system's total energy while adjusting atomic positions and, if applicable, unit cell dimensions. An overview of the geometry optimization process is provided below (see Figure 3.3). First step, it is initial geometry which starts with the initial atomic coordinate of the system. Next, the DFT calculation determines the system's total energy using the self-consistent field (SCF) method and further calculates the atomic forces using the Hellmann-Feynman theorem. In case of convergence check after calculations, If the calculated atomic forces are below the predefined tolerance limit, the optimization is complete, and the resulting geometry is accepted. However, If the atomic forces exceed the tolerance limit, the atomic positions are adjusted based on the calculated forces and gradients. The optimization process then returns to step 2, iterating until convergence is achieved. Optimization algorithms, such as the conjugate gradient method, are typically used to guide the adjustments (Dai et al., 2017).

Geometry optimization is a foundational process in DFT that allows for accurate predictions of molecular and material properties. This method offers critical insights

into the behavior, stability, and structural characteristics of chemical systems by calculating the optimal atomic positions and total energy.

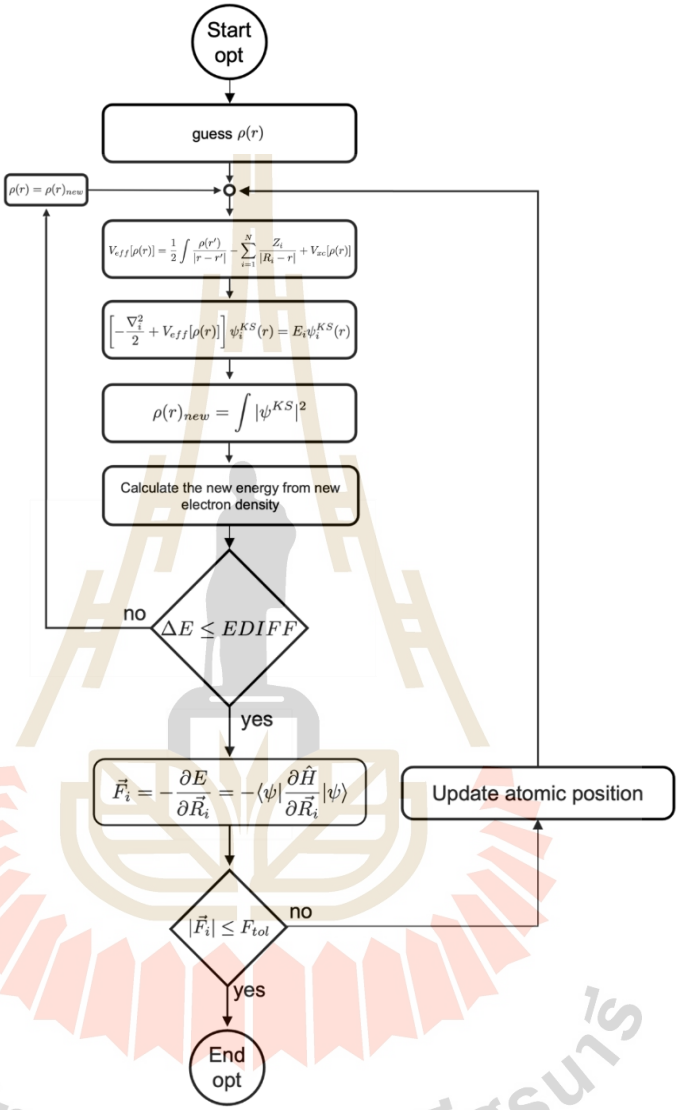


Figure 3.3 Schematic representation of the optimization process in DFT calculations.

3.4 vdW correction

One of the well-known limitations of DFT is its inability to accurately capture van der Waals (vdW) interactions. These interactions are weak, long-range forces between molecules or atoms that result from temporary fluctuations in electron density. Standard DFT functionals, including LDA and GGA, are designed to capture local exchange-correlation effects but frequently underestimate vdW interactions.

To overcome this limitation, various correction methods have been developed to incorporate vdW interactions into DFT calculations. One widely used approach in the DFT-D3 method developed by Grimme (Grimme et al., 2010). DFT-D3 is an empirical correction method, to account for long-range van der Waals (vdW) interactions. Standard DFT functionals often fail to capture these non-covalent forces, which are critical for describing many systems (e.g., molecular crystals, protein folding, adsorption). As defined in the paper, the total energy is the sum of the standard DFT energy and the dispersion correction:

$$E_{\text{DFT-D3}} = E_{\text{KS-DFT}} + E_{\text{disp}} \tag{3.21}$$

The dispersion term, E_{disp}, consists of a two-body term E_2) and an optional three-body term (E_3, which is often omitted). The primary E_2 term, which truncates the full series at $n = 8$, is:

$$E_{\text{disp}} \approx E^{(2)} = -\sum_{i=1}^{N_{\text{at}}} \sum_{j=i+1}^{N_{\text{at}}} \sum_{\mathbf{L}} \left(s_6 f_{d,6}(r_{ij,\mathbf{L}}) \frac{C_{6ij}}{r_{ij,\mathbf{L}}^6} + s_8 f_{d,8}(r_{ij,\mathbf{L}}) \frac{C_{8ij}}{r_{ij,\mathbf{L}}^8} \right) \tag{3.22}$$

Where:

- $\sum_{i=1}^{N_{\text{at}}} \sum_{j=i+1}^{N_{\text{at}}} \cdots$ This is a sum over all unique atom pairs in the system, which contains N_{at} atoms. (This notation, summing j from $i+1$, is a computationally efficient way to sum each pair only once).
- $\sum_L$ This is the summation over lattice vectors, L . This component is only used for periodic systems (like crystals or surfaces). It ensures that atom i interacts not only with atom j in the primary unit cell but also with all of its periodic images in adjacent cells. For an isolated molecule, this summation is absent.
- s_6 and s_8 (Global Scaling Factors) These are the key empirical parameters of the D3 method. Each density functional (like PBE, B3LYP, etc.) has its own pair of s_6 and s_8 values, which are determined by fitting to a benchmark set of high-accuracy reference energies. These parameters "tune" the correction to seamlessly merge

with the short-range correlation already provided by the specific DFT functional. As the paper states, s_8 is often the main adjustable parameter.

- C_{6ij} and C_{8ij} (Dispersion Coefficients) These are the $n=6$ (dipole-dipole) and $n = 8$ (dipole-quadrupole) dispersion coefficients for the atom pair (i, j). A key innovation of D3 is that these coefficients are not static. They are calculated "on the fly" based on the coordination number (CN) of each atom in its specific molecular environment. This makes D3 far more accurate than previous methods, as the coefficients adapt to the atom's local chemistry.
  - $r_{ij,L}$ (Interatomic Distance) This is the distance between atom i and atom j (or its periodic image, L).
  - $f_{d,n}(r_{ij,L})$ (The Damping Function) This function is critical for preventing "double counting" and unphysical behavior. It smoothly turns off the dispersion correction ($f \rightarrow 0$) at short interatomic distances, where atoms are covalently bonded. It ramps up to ($f \rightarrow 1$) at larger distances, turning the correction "on" only where it's needed (i.e., in the non-covalent, long-range region).

3.5 Climbing image-nudged elastic band method

The climbing image-nudged elastic band (CI-NEB) (Henkelman et al., 2000) is an advanced computational technique widely used in DFT calculations to suggest transition states and map reaction pathways with precision. By enhancing the traditional Nudged Elastic Band (NEB) method, CI-NBE introduces a “climbing” image that converges toward the transition state, allowing for precise determination of the highest energy points along a reaction coordinate. Next, paraphrase will summarize knowledge of these methods.

In the case of NEB, it can calculate the reaction pathway by constructing a series of intermediate configurations (called images) that connect the initial and final states. Each image is characterized by specific atomic coordinates, forming an elastic band represented as [R_0, R_1, R_2, ..., R_N], where R_0 and R_N remain fixed as the initial and final state. The force acting on each image (F_i) is a combination of spring force and true force. Spring force is used to ensure images remain evenly spaced along the reaction

path. True force is used to account for the system's potential energy, acting perpendicular to the reaction path. The total force for an image i is expressed as:

$$\vec{F}_i^{NEB} = \vec{F}_i^{s||} - \nabla E(\vec{R}_i)^{\perp} \tag{3.23}$$

The true force is given by:

$$\nabla E(\vec{R}_i)^{\perp} = \nabla E(\vec{R}_i) - \nabla E(\vec{R}_i) \cdot \hat{\tau}_i \tag{3.24}$$

Where ∇E is the gradient of energy with respect to atomic coordinates, and $\hat{\tau}_i$ is the normalized local tangent at image i. Spring force is defined as:

$$\vec{F}_i^{s||} = k(|\vec{R}_{i+1} - \vec{R}_i| - |\vec{R}_i - \vec{R}_{i-1}|)\hat{\tau}_i \tag{3.25}$$

Where k is spring constant. Optimization algorithms move the images according to NEB force until the forces converge below a set threshold. In our study, we set the convergence criterion for NEB calculations which is 0.05 eV/Å

The CI-NBE method improves upon NEB by refining the transition state suggestion. After several iterations with the standard NEB, the image with the highest energy (i_{max}) is identified. This image is then allowed to "climb" toward the saddle point by modifying its force calculation:

$$\vec{F}_{i_{max}} = -\nabla E(\vec{R}_{i_{max}}) + 2\nabla E(\vec{R}_{i_{max}}) \cdot \hat{\tau}_{i_{max}} \tag{3.26}$$

This modification ensures that the climbing image is unaffected by spring forces and moves directly to the saddle point, representing the transition state. Consequently, the CI-NEB method is widely used in computational chemistry to study reaction mechanisms and calculate energy barriers for chemical reactions. It delivers three key benefits by determining the transition state with accuracy, mapping minimum energy pathways precisely, and providing insights into the reaction dynamics of complex systems.

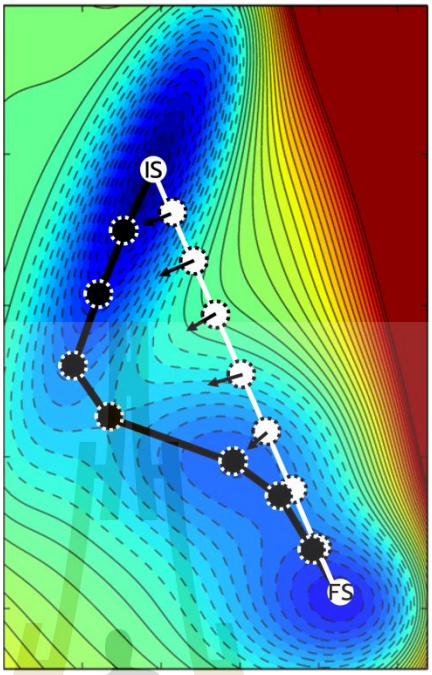


Figure 3.4 Schematic of the potential energy surface (PES) and NEB calculation, showing the initial reaction pathway (white line) and the optimized reaction pathway (black line).

Overall, the CI-NEB method combines the principles of the NEB method with the climbing image adjustment, providing an efficient and reliable approach for identifying transition states and understanding reaction mechanisms. By ensuring accurate placement of the transition state along the reaction coordinate, CI-NEB is a critical tool for investigating complex chemical reactions and energy landscapes.

3.6 Gibbs free energy (G) calculation

The Gibbs free energy (G) can be expressed as the sum of the system's enthalpy (H) and entropy (S), as shown below:

$$G = E_{elec} + E_{ZPE} - TS \tag{3.27}$$

Here, E_{elec} represents electronic energy, and E_{elec} is the zero-point energy correction applied to the electronic energy to account for quantum mechanical effects at absolute zero. The zero-point energy is calculated as:

$$ZPE = \sum_i \frac{hv_i}{2} \tag{3.28}$$

where, h is the Planck's constant and v_i are the computed vibrational frequencies of the system. This correction is essential in ensuring accurate thermodynamic predictions, especially for molecular systems at low temperatures. For entropy (S), it is given by the equation:

$$S = k_B lnQ \tag{3.29}$$

The partition function (Q) can be expressed as the product of translational, rotational, and vibrational components:

$$Q = f_{trans}\, f_{vib} f_{rot} \tag{3.30}$$

In equation (3.30), The calculation of entropy relies on the partition function, which for ideal gas molecule can be divided into translational, rotational, and vibrational contributions. Each component corresponds to a specific type of motion or degree of freedom within the system. For a free-gas molecule, the translational partition function in three dimensions is given by:

$$f_{trans} = V\left(\frac{2\pi M k_b T}{h^2}\right)^{3/2} \tag{3.31}$$

where V is the volume of the gas, M is the molecular mass, k_B is the Boltzmann constant. Often, V can be substituted using the ideal gas equation of state $PV = k_B T$. For a single dimension, the translational partition function simplifies to:

$$f_{trans} = \frac{L\sqrt{2\pi m k_b T}}{h} \tag{3.32}$$

Where L is the characteristic length along one dimension. In case of the rotational partition function for a diatomic molecule can be expressed as:

$$f_{rot} = \frac{8\pi^2 I k_b T}{h^2} \tag{3.33}$$

Where I is the moment of inertia about an axis perpendicular to the molecular axis and passing through the center of mass.

In the harmonic approximation, the vibrational partition function is given as:

$$f_{vib} = \frac{1}{1 - e^{-h\omega/k_b T}} \tag{3.34}$$

Each vibrational mode contributes independently to the partition function, and the harmonic approximation assumes that the vibrations are small perturbations around equilibrium.

3.7 Smooth Overlap of Atomic Positions (SOAP)

The Smooth Overlap of Atomic Positions (SOAP) descriptor has been extensively studied and applied in computational materials science and chemistry (Bartók et al., 2013). It was introduced as a method to represent atomic neighborhood environments, ensuring differentiability and invariance to fundamental symmetries, making it particularly suitable for analyzing structural similarities in materials. SOAP has been widely used for fitting potential energy surfaces, optimizing machine learning interatomic potentials, and improving predictive modeling in various applications, including drug design and materials characterization. Additionally, SOAP descriptors have been employed for mapping atomic coordinates to electron densities, demonstrating their effectiveness in predicting charge distributions in different systems. These studies underscore the versatility and efficacy of SOAP in characterizing atomic environments and predicting material properties.

SOAP achieves its structural representation by constructing a continuous atomic density function, where atomic positions are expressed as Gaussian functions centered at each atom. Mathematically, this is given by:

$$\rho_i(r) = \sum_j exp\left(-\frac{|r - r_j|^2}{2\sigma^2}\right) f_{cut}(|r - r_j|) \tag{3.35}$$

where $\rho_i(\mathrm{r})$represents the atomic density around atom i, σ is the Gaussian broadening parameter, and $f_{cut}(\mathrm{r})$ is a cutoff function ensuring that only atoms within a distance r_{cut} contribute to the density. The cutoff function smoothly decays atomic contributions at large distances:

$$f_{cut}(r) = \left(1 - \frac{r}{r_{cut}}\right)^n \tag{3.36}$$

where r_{cut} is the cutoff radius, defining the spatial range of atomic interactions.

To make the density function computationally manageable, it is expanded using radial basis functions $g_n(r)$ and spherical harmonics $Y_{lm}(\theta, \phi)$, resulting in:

$$\rho_i(r) = \sum_{nlm} c_{nlm} g_n(r)\, Y_{lm}(\theta, \phi) \tag{3.37}$$

where $g_n(r)$ captures radial features, controlled by the maximum number of radial basis functions (n_{max}), and ($Y_{lm}(\theta, \phi)$) describes angular features, determined by the maximum angular momentum (l_{max}). The expansion coefficients, computed as:

$$c_{nlm} = \int \rho_i\,(r) g_n(\mathrm{r})\, Y_{lm}(\theta, \phi) dr \tag{3.38}$$

numerically encode the atomic environment into a descriptor vector.

To ensure rotational invariance, SOAP descriptors are constructed using the power spectrum:

$$p_{nn'l} = \sum_m c_{nlm} c^*_{n'lm} \tag{3.39}$$

This power spectrum forms a unique fingerprint of the atomic neighborhood, allowing for robust structural comparisons independent of orientation.

To gain deeper insight into the correlation between structural changes, adsorption behavior, and deformation energy, SOAP analysis was employed to quantify structural similarity before and after adsorption. The SOAP similarity score (Similarity) is calculated using the following equation

$$\text{Similarity} = \left(\frac{\mathrm{X_{initial}} \cdot \mathrm{X_{final}}}{\|\mathrm{X_{initial}}\| \cdot \|\mathrm{X_{final}}\|}\right)^{\zeta} \times 10 \tag{3.40}$$

Where, $X_{initial}$ represents the SOAP descriptor vector for the initial (reference) structure, and X_{final} is the SOAP descriptor vector for the final (adsorbed) structure. The terms $\|\mathrm{X_{initial}}\|$ and $\|\mathrm{X_{final}}\|$ denote the magnitudes of these vectors, ensuring the similarity

is normalized. (set to 4 in this study) amplifies the similarity value. This equation computes the cosine similarity between the SOAP vectors and scales the result from 0 to 10, with a score close to 10 indicating minimal structural change and high stability.

The SOAP descriptor provides an effective and numerically stable means of quantifying local atomic environments, making it a widely used tool in computational materials science. By incorporating SOAP into adsorption studies, it becomes possible to systematically compare structural distortions and gain insight into the stability and interaction strength of adsorbed species.

3.8 Crystal orbital Hamilton population (COHP)

The crystal orbital hamilton population (COHP) is a theoretical method used in computational chemistry and materials science to suggest chemical bonding in periodic systems (Steinberg & Dronskowski, 2018). It is particularly effective in quantifying the bonding, nonbonding, and antibonding interactions between atomic orbitals in solids. The fundamental concept of COHP focused on partitioning the electronic structure of a system into contributions from specific atomic pairs or orbitals. It combines concepts from quantum mechanics and electronic structure theory, particularly the Hamiltonian formalism, to analyze the interaction between two atomic orbitals.

COHP is often evaluated relative to the Fermi level, which suggests the energy up to which the electronic states are occupied. The bonding interactions below the Fermi level are most significant in determining the stability of the system.

It can be calculated based on electronic Hamiltonian $(\hat{H})$ describes the total energy of the quantum system, including kinetic and potential energies. In COHP, it is used to evaluate the interaction between two atomic orbitals:

$$H_{ij} = \int \psi_i^*(\mathbf{r}) \hat{H} \psi_j(\mathbf{r}) d^3r \tag{3.41}$$

The term of Hamilton population quantifies the contribution of each orbital pair to the total electronic energy:

$$HP_{ij}(E) = -H_{ij}(E) \cdot n_{ij}(E) \tag{3.42}$$

After that, COHP is derived by integrating over all energy states:

$$-COHP(E) = -\sum_{i,j} H_{ij}(E) \cdot n_{ij}(E) \tag{3.43}$$

The negative value of COHP represents bonding contributions, whereas positive values show antibonding contributions. To obtain a single scalar value representing the total bonding interaction between two atoms, COHP can be integrated over all relevant energy levels:

$$ICOHP = \int_{E_{\min}}^{E_F} -COHP(E)dE \tag{3.44}$$

ICOHP value can suggest the bonding strength. Negative ICOHP suggests strong bonding interactions, while positive value suggest dominant antibonding interactions. Although COHP and ICOHP can explain the strength bond of pair atoms, it still has limitations which we should be concerned about. First, it is basis set dependence. Results can vary with the choice of basis sets, requiring careful validation. Computational cost increases with system size, especially for large supercells or complex systems. Lately, the choice of integration limits in ICOHP calculations can influence the results, particularly in systems with partially filled bands.

3.9 Summary of computational details

In this thesis, all calculations were employed using spin-polarized Density Functional Theory (DFT) (Hohenberg & Kohn, 1964b) as implemented in the Vienna Ab-initio Simulation Package (VASP 6.3) (Kresse & Furthmüller, 1996b, 1996a). The frozen-core projector-augmented wave (PAW) method was used to describe the electron-ion interactions (Blöchl, 1994). For the V_2CO_2 structure, valence electrons included V 3d4s, C 2s2p, and O 2s2p treated within a plane-wave basis. For S_8 and Al_2S_n species, Al 3s3p and S 3s3p valence electrons were considered. Screening of single-atom (SA) transition metals included 3*d*-transition metals, considering their 3d4s valence electrons, respectively. The exchange-correlation interactions were approximated using the Generalized Gradient Approximation (GGA) with the Perdew-Burke-Ernzerhof (PBE) functional (Kresse & Joubert, 1999; Perdew et al., 1996). Weak van der Waals

interactions between the adsorbates (S_8 and Al_2S_n) and the decorated 3d-TMs on V_2CO_2 were included using the DFT-D3 (Grimme et al., 2010, 2011). Structural optimizations were carried out with a kinetic energy cutoff of 500 eV. Monkhorst-Pack k-point sampling was employed (Monkhorst & Pack, 1976), using a 3 × 3 × 1 grid for structural optimization and a 5 × 5 × 1 grid for electronic density of states (DOS) calculations. Optimization was considered complete when the energy difference between iterations reached 10^{-6} eV and residual forces were below 0.02 eV/Å. Charge distribution analysis was conducted using the Bader charge decomposition scheme. The energy barriers and reaction pathways for the decomposition of Al_2S_3 was calculated using the Climbing Image Nudged Elastic Band (CI-NEB) method (Henkelman et al., 2000)

มหาวิทยาลัยเทคโนโลยีสุรนารี

3.10 References

Bartók, A. P., Kondor, R., & Csányi, G. (2013). *On representing chemical environments*.

Blöchl, P. E. (1994). Projector augmented-wave method. *Physical Review B*, *50*(24), 17953–17979.

Born, M., & Oppenheimer, R. (1927). Zur Quantentheorie der Molekeln. *Annalen Der Physik*, *389*(20), 457–484.

Dai, X., Liu, Z., Zhang, L., & Zhou, A. (2017). A Conjugate Gradient Method for Electronic Structure Calculations. *SIAM Journal on Scientific Computing*, *39*(6), A2702–A2740.

Grajcarova, L. (2013). *Simulations of structural phase transitions in crystals using ab-initio metadynamics*.

Grimme, S., Antony, J., Ehrlich, S., & Krieg, H. (2010). A consistent and accurate ab initio parametrization of density functional dispersion correction (DFT-D) for the 94 elements H-Pu. *The Journal of Chemical Physics*, *132*(15), 154104.

Grimme, S., Ehrlich, S., & Goerigk, L. (2011). Effect of the damping function in dispersion corrected density functional theory. *Journal of Computational Chemistry*, *32*(7), 1456–1465.

Henkelman, G., Uberuaga, B. P., & Jónsson, H. (2000). A climbing image nudged elastic band method for finding saddle points and minimum energy paths. *The Journal of Chemical Physics*, *113*(22), 9901–9904.

Hohenberg, P., & Kohn, W. (1964a). Inhomogeneous Electron Gas. *Physical Review*, *136*(3B), B864–B871.

Hohenberg, P., & Kohn, W. (1964b). Inhomogeneous Electron Gas. *Physical Review*, *136*(3B), B864–B871.

Kresse, G., & Furthmüller, J. (1996a). Efficiency of ab-initio total energy calculations for metals and semiconductors using a plane-wave basis set. *Computational Materials Science*, *6*(1), 15–50.

Kresse, G., & Furthmüller, J. (1996b). Efficient iterative schemes for ab initio total-energy calculations using a plane-wave basis set. *Physical Review B*, *54*(16), 11169–11186.

Kresse, G., & Joubert, D. (1999). From ultrasoft pseudopotentials to the projector augmented-wave method. *Physical Review B*, *59*(3), 1758–1775.

Monkhorst, H. J., & Pack, J. D. (1976). Special points for Brillouin-zone integrations. *Physical Review B*, *13*(12), 5188–5192.

Nakamachi, E., Uetsuji, Y., Kuramae, H., Tsuchiya, K., & Hwang, H. (2013). Process Crystallographic Simulation for Biocompatible Piezoelectric Material Design and Generation. *Archives of Computational Methods in Engineering*, *20*.

Perdew, J. P., Burke, K., & Ernzerhof, M. (1996). Generalized Gradient Approximation Made Simple. *Physical Review Letters*, *77*(18), 3865–3868.

Perdew, J. P., & Wang, Y. (1992). Accurate and simple analytic representation of the electron-gas correlation energy. *Physical Review B*, *45*(23), 13244–13249.

Santra, B., Michaelides, A., & Scheffler, M. (2007). On the accuracy of density-functional theory exchange-correlation functionals for H bonds in small water clusters: Benchmarks approaching the complete basis set limit. *The Journal of Chemical Physics*, *127*(18), 184104.

Steinberg, S., & Dronskowski, R. (2018). The crystal orbital hamilton population (COHP) method as a tool to visualize and analyze chemical bonding in intermetallic compounds. In *Crystals* 8(5). MDPI AG.

มหาวิทยาลัยเทคโนโลยีสุรนารี

CHAPTER IV

INVESTIGATION OF CATHODE PERFORMANCE IN ALUMINUM-SULFUR BATTERIES: DFT, AND COMPUTATIONAL STUDY

In the previous chapter, we established the theoretical and computational framework for this study. We began with an overview of the theoretical and computational methods, focusing on the Schrödinger equation and its approximate solutions through the variational principle. Key developments in computational materials science were highlighted, followed by an overview of density functional theory (DFT), the foundation of our calculations. Methods for structural optimization and error correction in DFT were also discussed, along with the climbing image-nudged elastic band (CI-NEB) method for the decomposition of Al_2S_3. Finally, computational details implemented using the Vienna Ab initio Simulation Package (VASP) were summarized.

In this chapter, we investigated the structural and electronic properties of 3d-transition metals decorated V_2CO_2 cathode materials. We assess the stability of Al_2S_n species on SA@V_2CO_2 and DA@V_2CO_2 using advanced structural analysis techniques, including Bader charge and Smooth Overlap of Atomic Positions) analyses. The chapter further explores the sulfur reduction reaction to evaluate cathode performance and examines the decomposition of Al_2S_3 to understand the reversibility and efficiency of aluminum-sulfur batteries. These investigations provide critical insights into the design of high-performance cathode materials.

4.1 The structural and electronic properties for V_2CO_2 MXene

According to previous study, the redox process of Al–S batteries with the electrolyte of 1-ethyl-3-methylimidazolium chloride ($[EMIM]^+Cl^-$) as electrolyte can be summarized as given equations (4.1) and (4.2) The charge-discharge process of Al–S

batteries involved the formation of S_8 and Al_2S_n species as equations (4.3) and (4.4). The sulfur reduction reactions initially start from S_8, Al_2S_{18}, Al_2S_{12}, Al_2S_6 to Al_2S_3.

$$8Al + 14AlCl_4^- \rightarrow 8Al_2Cl_7^- + 6e^- \quad (4.1)$$

$$8Al_2Cl_7^- + 6e^- + 3S \rightarrow Al_2S_3 + 14AlCl_4^- \quad (4.2)$$

$$\frac{1}{8}S_8 + \frac{1}{3}e^- \rightarrow \frac{1}{6}S_6^{2-} \quad (4.3)$$

$$\frac{1}{6}S_6^{2-} + \left(\frac{2}{x} - \frac{1}{3}\right)e^- \leftrightarrow \frac{1}{x}S_x^{2-} \ (1 \leq x \leq 6) \quad (4.4)$$

The optimized structures of S_8 and Al_2S_n species show the most stable structures among all the possible structures in Figure 4.1a. The morphology of S_8 is a crownlike orthorhombic structure. Al_2S_3 presents a planar bent. For the structure of Al_2S_6, Al_2S_{12}, and Al_2S_{18}, they form 3D cluster shapes without overhanging bonds which results were consistent with other computational studies (Bhauriyal & Pathak, 2020; Z. Wang et al., 2022; Zheng et al., 2022). The side views of the surfaces are presented in Figure 4.1b, where V_2CO_2 with a terminal group of O atoms has the V–O bond with length of 1.95 Å, and V–C bond with length of 2.05 Å. In this study, 3d-TMs excluding V were decorated on the bare V_2CO_2 due to their unique catalytic properties, specifically their ability to improve polysulfide conversions by facilitating electron transfer and promoting adsorption. Additionally, the choice of 3d-TMs (like Cr, Mn, and Fe) is driven by their distinct properties, such as better catalytic activity, structural stability, and flexibility in designing materials with tunable electronic characteristics, which improves their performance in energy storage applications such as Li-S, and Al-S batteries (Andritsos et al., 2021; Chen et al., 2021; Gu et al., 2020; Ju et al., 2022; Yang et al., 2013).

For the binding site of SA, there are four possible binding sites including $bridge_{VO}$, Hollow O_{TopV}, Hollow O_{TopC}, and O_{Top} shown in Figure 4.1b. We find that O_{top} is unstable site for all decorated SAs. As well as $bridge_{VO}$ site, the decorated SAs change into Hollow O_{TopV} site for all surfaces. These suggest that there are two

preferential sites where Sc, Ti, Cr, Mn, and Cu prefer to bind on Hollow O_{TopC} site, and Fe, Co, Ni, and Zn as decorated SAs prefer to bind on Hollow O_{TopV} site shown in Figure 4.1c. Similarly, the DA binding site including Cr and Mn follows the same strategy in both the no-oxygen vacancy and oxygen vacancy systems (V_O). A detailed analysis of all tested configurations for both SA and DA systems is provided in Figure A1. To assess the viability of these materials, we determined their relative stability. For the SA and d-DA-no systems, where dopants are decorated on the surface, we calculated the binding energy (E_b) to quantify the strength of the anchor using the formula:

$$E_b = E_{decorated} - E_{surface} - nE_{metal} \quad (4.5)$$

where $E_{decorated}$ and $E_{V_2CO_2}$ are the total energy of the decorated V_2CO_2 for SA and DA systems and V_2CO_2 or with an oxygen vacancy for d-DA-V_O@V_2CO_2, respectively. n is the number of decorated atoms, and E_{metal} is the energy of the single atom metal.

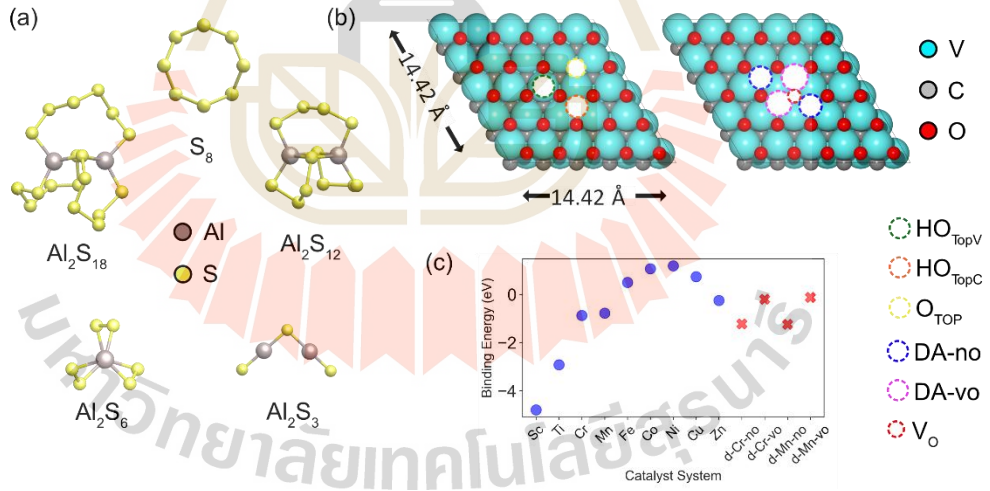


Figure 4.1 Optimized structures of V_2CO_2 and adsorption configurations: (a) Top views of the optimized 3×3×1 V_2CO_2. (b) Possible binding sites for SA@V_2CO_2. (c) DA@V_2CO_2 configurations: *d*-DA (left) without oxygen vacancy and *d*-DA-vo (right) with surface oxygen vacancy. (c) Binding energy of SA and DA on V_2CO_2 surfaces for various transition metal.

We find that the 3d-TM, Zn and DAs have negative E_b values, indicating the possibility of successful fabrication, providing a reference for experimental preparation. To further examine their stability under operating conditions, we performed ab initio molecular dynamics (AIMD) simulations, a method used in similar a computational study (Singsen et al., 2022). The simulations, performed at e.g., 300 K for 10 ps, revealed that the structures remain intact with no significant degradation, thus suggesting their excellent thermal stability (see Figure A2 for details).

To understand how SAs and DAs affect the material's electronic properties, we analyzed the projected density of states (PDOS) for each system (see Figure A3 for all systems). Figure 4.2 presents the DOS for representative cases: bare, Co@V_2CO_2, d-Cr@V_2CO_2, and d-Cr-V_O@V_2CO_2. We find that the bare exhibits metallic character. The states near the Fermi level are dominated by V 3d orbitals, with non-negligible contributions from C 2p and O 2p orbitals, consistent with previous computational studies (Gao et al., 2022; Zou et al., 2024). Both SA and DA@V_2CO_2 preserves this essential metallic nature. The SA systems, represented by Co@V_2CO_2, introduces additional states near the Fermi level originating from the Co atom, though these are less dominant than the V 3d states. Similarly, the DA systems maintain conductivity, where the interaction between the dual 3d-TMs and the substrate further modulates the states around the Fermi level.

The impact of these tuned structural and electronic properties on the material's performance as a cathode host will be systematically investigated in the following sections.

มหาวิทยาลัยเทคโนโลยีสุรนารี

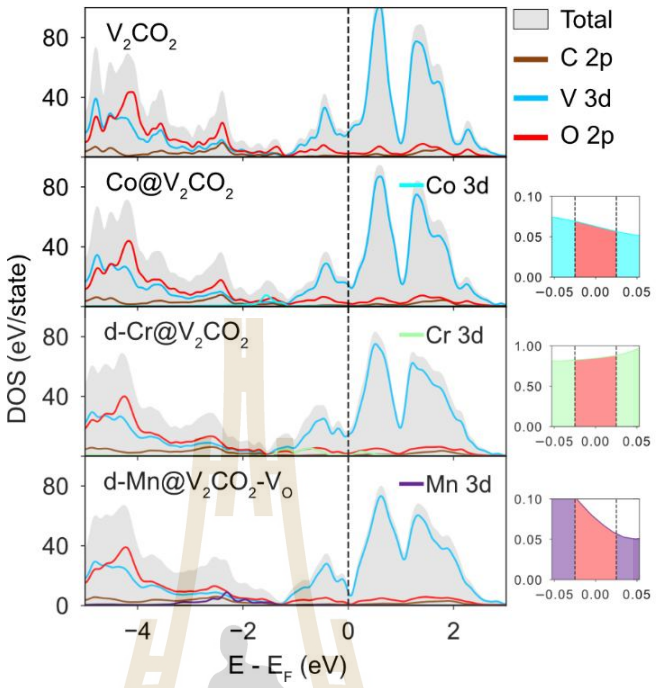


Figure 4.2 Projected Density of States (PDOS) for the bare V_2CO_2 surface, SA (Co), and DA (d-Cr and d-Mn-V_O). Fermi level (E_F) is adjusted to 0 eV. Light blue, V; brown, C; red, O; sky blue, Co; neon, d-Cr; violet, d-Mn-V_O.

4.2 Adsorption energy of sulfur species (S_8, Al_2S_n)

A critical challenge hindering the practical application of Al-S batteries is the dissolution of Al_2S_n species into the electrolyte. This phenomenon, known as the shuttle effect, is primarily caused by the high solubility of large, higher order Al_2S_n species such as S_8, Al_2S_{18}, and Al_2S_{12}. To mitigate this issue, the V_2CO_2, SA@V_2CO_2 and DA@V_2CO_2 must be capable of strongly anchoring these S_8 and Al_2S_n species to confine them within the cathode region. Firstly, we investigated for the most stable adsorbed configurations and adsorption sites. The optimized structures of S_8 and Al_2S_n species are detailed in Figure A4-A8**.** To understand the anchoring performance, we deconstructed the adsorption process into its fundamental energetic components: the net adsorption energy (E_{ads}), the intrinsic interaction energy (E_{int}),

and the energetic penalty from structural deformation (E_{def}). The adsorption energy, E_{ads}, can be calculated using the following equation:

$$E_{ads} = E_{total} - E_{surface} - E_{S_8\ or\ Al_2S_n} \quad (4.6)$$

where E_{total}, $E_{surface}$, and $E_{S_8\ or\ Al_2S_n}$ are the total energy of the fully relaxed adsorbed system, the isolated catalyst-decorated surface, and the isolated sulfur species in a vacuum, respectively. A more negative E_{ads} value indicates a stronger, more favorable adsorption strength.

This adsorption energy is a balance between the intrinsic interaction and the deformation penalty, as defined by the relationship $E_{ads} = E_{int} + E_{def}$ These components are calculated as:

$$E_{int} = E_{total} - E_{surface\ (distorted)} - E_{S_8\ or\ Al_2S_n\ (disorted)} \quad (4.7)$$

$$E_{def} = \left(E_{surface\ (distorted)} - E_{surface}\right) + \left(E_{S_8\ or\ Al_2S_n\ (disorted)} - E_{S_8\ or\ Al_2S_n}\right) \quad (4.8)$$

Here, E_{int} is quantifies the interaction between the species and the surface in their final (E_{total}) by subtracting the single-point energy of the surface ($E_{surface\ (distorted)}$) and the S_8 or Al_2S_n species ($E_{S_8\ or\ Al_2S_n\ (disorted)}$) in their final, distorted geometries. This isolates the interaction, separate from the energy cost of deformation. The deformation energy, E_{def}, is the sum of the energy required to distort the surface from its relaxed state ($E_{surface}$) to its final adsorbed geometry ($E_{S_8\ or\ Al_2S_n\ (disorted)}$) and to distort the polysulfide from its relaxed state ($E_{S_8\ or\ Al_2S_n}$) to its final adsorbed geometry ($E_{S_8\ or\ Al_2S_n\ (disorted)}$).

On the bare V_2CO_2, Al-O bonds form easily during Al_2S_n species adsorption. Species like Al_2S_3, Al_2S_6, and Al_2S_{12} strongly adsorb due to the formation of Al-O bonds. In contrast, S_8 and Al_2S_{18} show weak adsorption. S_8 lacks Al atoms, preventing Al-O bond formation, while Al_2S_{18} is a large cluster where S atoms obstruct bonding shown in Figure 4.3a.

For the SA@V_2CO_2, S atoms from S_8 and Al_2S_n species form bonds with the TMs. Depending on the adsorption site, Al_2S_n species adopt different configurations on the surface. For example, Fe@V_2CO_2, where Fe binds to the Hollow O_{TopV} site, the

Fe atom forms multiple bonds with S atoms in higher-order Al_2S_n species. Al_2S_3 prefers Al–O bonds, while S atoms favor Fe–S bonds in Figure 4.3b. Cu@V_2CO_2 behaves similarly, but the Al_2S_n configuration varies depending on the TM atom in Figure 4.3c.

On DA@V_2CO_2, S atoms of S_8, and high orders of Al_2S_n interact form bonds with both TMs. For high orders of Al_2S_n, several S atoms can bond with dual atoms resulting the different configurations comparing to SA@V_2CO_2 While Low orders of Al_2S_n species also bond with both TMs, but their size and fewer S atoms cause structural distortion shown in Figure 4.3d and Figure 4.3e. Furthermore, the adsorption of Al_2S_n species on DA@V_2CO_2 for example, with and without oxygen vacancies (dCr@V_2CO_2 and dCr-V_O@V_2CO_2) represent the different configurations suggested the effect of vacancies on the adsorption. These might be discussed in the further section.

The calculated interaction energy for S_8 and large soluble Al_2S_n species are presented in Figure 4.4a. The solid bars represent the final, net adsorption energy (E_{ads}), while the hatched bars stacked on top represent the positive deformation energy penalty (E_{def}). Therefore, the total height of each stacked bar (solid plus hatched) represents the total intrinsic interaction energy (E_{int}). On the bare V_2CO_2 surface, the adsorption of these species is weak, with E_{ads} values of -0.96 eV for S_8, -1.02 eV for Al_2S_{18}, and -2.15 eV for Al_2S_{12}. According to previous computational study, we find that the E_{ads} of Al_2S_{18}, Al_2S_{12} with the ionic liquid electrolyte are -1.49, and -1.34 eV, respectively. This refers to the weak adsorption strength that might be insufficient to overcome the strong adsorption strength of the high orders of Al_2S_n species with ionic liquid in the electrolyte, indicating that the bare might be an ineffective anchor and would suffer from a severe shuttle effect. Critically, the hatched bars (E_{def}) for the bare surface are almost the same portion as adsorption energy, meaning the total interaction energy (E_{int}) is nearly identical to the final adsorption energy. This lack of deformation is characteristic of weak physisorption. Critically, the hatched bars (E_{defs}) for the bare surface are a significant portion of the E_{ads}, indicating that a deformation penalty is paid even for this weak interaction.

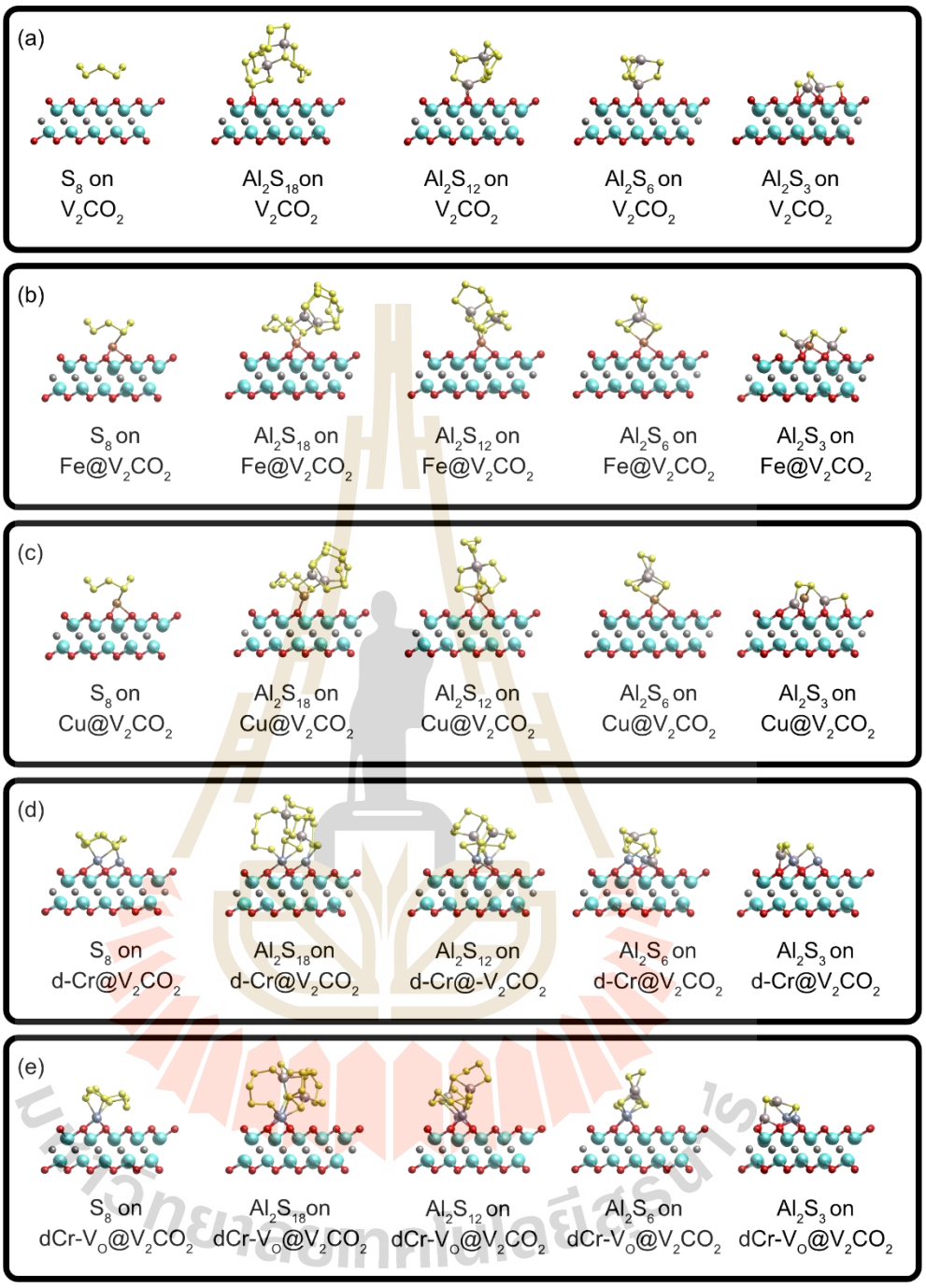


Figure 4.3 (a) Adsorption of S_8, and Al_2S_n species on the bare V_2CO_2 surface, showcasing side views of each configuration. (b) and (c) Adsorption of the same species on $Fe@V_2CO_2$, and $Cu@V_2CO_2$ with the SA positioned at the hollow O_{topV} site and the hollow O_{topC} site respectively (d) and (e) Adsorption of the species on V_2CO_2 surfaces modified with DA configurations, both with and without oxygen vacancies ($dCr@V_2CO_2$ and $dCr\text{-}V_O@V_2CO_2$).

The introduction of SAs significantly enhances the adsorption strength since the interaction between the high orders of Al_2S_n and SA@V_2CO_2 become stronger. For example, the E_{ads} of Al_2S_{12} is strengthened to -3.30 eV on Ti@V_2CO_2 and -3.53 eV on Cr@V_2CO_2, values which are stronger than that of the bare. Furthermore, E_{def} of SA@V_2CO_2 is less than that of the bare indicating the interaction between TMs and S atoms of Al_2S_n species did not break the structure of high orders Al_2S_n species. This trend holds across the various TMs, indicating that SAs are a viable strategy for effectively capturing or suppressing the high orders of Al_2S_n species. Furthermore, the early 3d-TMs including Sc, Ti, Cr, Mn show the negligible difference of the adsorption energy. While the late 3d-TMs like Co, Ni, Cu, and Zn show excessive adsorption strength especially Ni.

The anchoring effect is further amplified in DAs. These surfaces exhibit the strongest interaction (total bar height) compared to the other systems. This strong interaction comes with a significant penalty, as DAs also show the largest E_{def}. Despite this high energetic penalty, the resulting strongest adsorption strength, consistently surpassing both the bare and SA systems. For instance, the adsorption of Al_2S_{12} on the d-Cr-vo@V_2CO_2 system reaches -5.94 eV. These results clearly establish a performance hierarchy (Bare < SA < DA) and demonstrate that DA systems are a highly effective strategy for capturing the high orders of Al_2S_n species responsible for the shuttle effect.

To further understand this energetic trade-off, we analyzed the correlations between these energy components and the resulting structural changes, as shown in Figure 4.4b. The left panel, which plots E_{int} versus E_{def}, reveals a clear trade-off: stronger interactions (more negative E_{int}) force the system to pay a higher energetic penalty (more positive E_{def}). For instance, the adsorption of S_8 on the bare surface involves weak interaction and deformation. In contrast, the adsorption of Al_2S_n species on the decorated surfaces results in highly strong interaction and correspondingly large deformation. In Figure 4.4c, we examined this structural change using the similarity, where a score close to 10 indicates high structural integrity, while lower scores signify greater deformation. The right panel of Figure 3c plots this energetic penalty (E_{def}) against the similarity, a measure of structural distortion.

Interestingly, the plot does not show a simple linear correlation. Instead, it reveals a complex relationship, indicating that the energetic cost of deformation is not directly proportional to the magnitude of the structural distortion. This suggests that the cost of deforming a polysulfide is highly dependent on the specific nature of the interaction and not just the final degree of structural change.

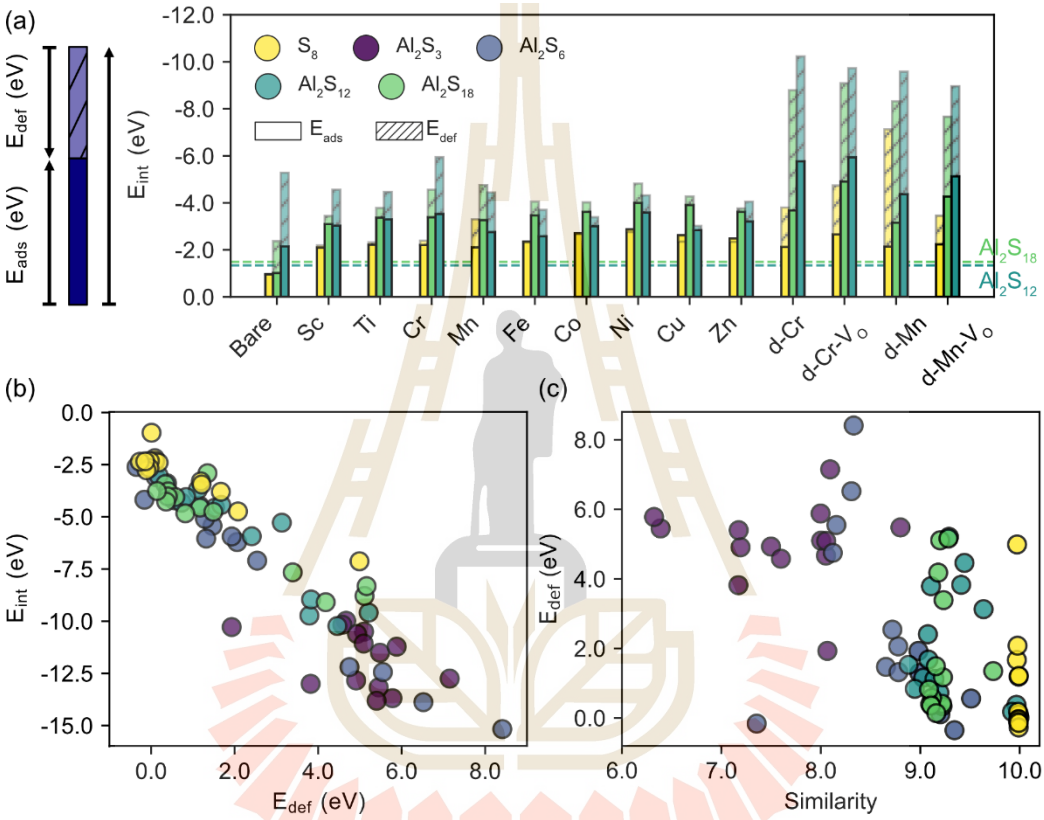


Figure 4.4 Analysis of polysulfide adsorption on bare and SA and DA systems. (a) Interaction energy (E_{int}) of large, soluble sulfur species (S_8, Al_2S_{18}, and Al_2S_{12}) on bare, SA, and DA@V_2CO_2. (b) Correlation between the interaction energy (E_{int}) and the corresponding adsorption energy (E_{ads}) and deformation energy (E_{def}) for all sulfur species across all surfaces. The species are color-coded as follows: S_8 (dark purple), Al_2S_{18} (medium blue), Al_2S_{12} (light green), Al_2S_6 (yellow-green), and Al_2S_3 (yellow).

Next, we investigated the electronic properties of the strong interaction. To quantify the charge difference upon adsorption, we performed a Bader charge

analysis. In this study, we calculated the charge transfer as the difference in the summed Bader charge of the three S atoms nearest the adsorption site between the adsorbed and isolated states. A positive value indicates that the S_8 or Al_2S_n species have lost electrons to the surface, while a negative value signifies that it has gained (or accepted) donated electrons from the surface.

The relationship between this charge transfer and the interaction energy (E_{int}) is plotted in Figure 4.5. An interesting behavior is observed for the bare surface. For higher-order species like Al_2S_{18} and Al_2S_{12}, there appears to be a significant charge transfer from the polysulfide to the surface (1.18 e and 0.92 e, respectively). However, this does not translate into strong interaction energy. This might suggest that the charge redistribution does not lead to the formation of a stable chemical bond, which is likely because the O-terminated V_2CO_2 surface is chemically unfavorable for forming strong bonds with the S atoms in the Al_2S_n species.

For the SA and DA systems, a clear correlation between the magnitude of charge transfer and interaction strength emerges. As seen in Figure 4.5, the higher-order species Al_2S_{18} and Al_2S_{12} (top panels) generally show a smaller magnitude of charge difference compared to the lower-order species Al_2S_6 and Al_2S_3 (bottom panels). For Al_2S_{18} and Al_2S_{12}, stronger interaction generally correlates with a greater loss of electrons to the surface. This trend is even more pronounced for the smallest species, Al^2S_3, which shows a large loss of electrons (up to ~2.4 e) on the decorated surfaces. This suggests a bonding mechanism where the catalyst atom withdraws electron density from these polysulfides. A notable exception is seen for the DA-V_O systems, which exhibit the strongest interaction for these species while showing a significant gain of electrons, indicating a different and highly effective anchoring mechanism enhanced by the V_O.

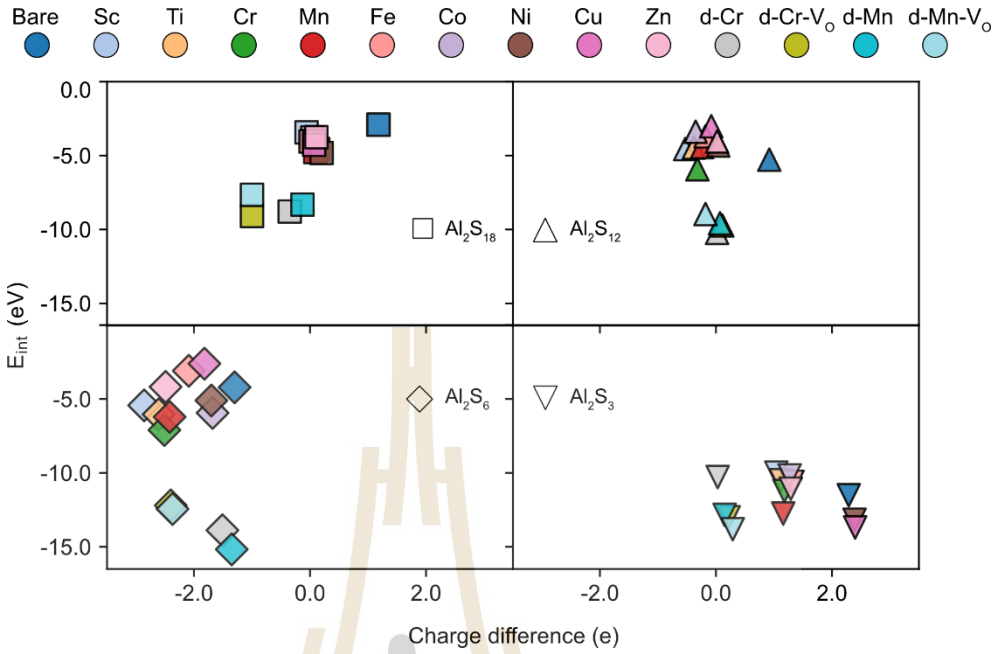


Figure 4.5 The relationship between charge transfer and interaction energy for Al_2S_n species. The plot shows the relationship between the calculated charge difference on the Al_2S_n species and the corresponding interaction energy (E_{int}) on the bare, SA, and DA@V_2CO_2. Each system is represented by a unique color, and each Al_2S_n species is represented by a unique marker shape, as defined in the legend.

In contrast, Al_2S_6 exhibits unique and opposite behavior. For this species, stronger interaction energy is directly correlated with a greater gain of electrons from the surface. This remarkable trend, with charge difference values reaching -2.86 e on Sc@V_2CO_2 and -2.37 e on d-Mn-V_O@V_2CO_2, suggests a mechanism dominated by electron donation from the surface to the Al_2S_6. This donation likely creates a powerful electrostatic and covalent interaction responsible for the strong binding. Overall, these results indicate that charge transfer, regardless of its direction, is a key electronic origin of the strong adsorption necessary for effective anchoring on the decorated surfaces.

This adsorption and the electronic properties appear to have a direct and measurable impact on the structure of the adsorbed S_8 and Al_2S_n species. The correlation between the similarity score and adsorption energy, presented in Figure 4.6a reveals a distinct trend: the stronger the adsorption energy, the more the S_8 and

Al_2S_n species' structure is deformed, resulting in a lower similarity score. For example, on the bare surface, the S_8 molecule has a similarity score of 9.99, indicating it is almost completely undeformed, which is consistent with weak physisorption. However, upon adsorption on the SA@V_2CO_2, the similarity scores for the Al_2S_n species decrease significantly. Furthermore, we can clearly see the separation of each S_8, Al_2S_6, Al_2S_3 species depending on the correlation of E_{ads} and similarity value. While Al_2S_{18} and Al_2S_{12} seem difficult to separate from each other since both are the large cluster. These indicate a direct structural consequence of strong anchoring.

Finally, to create a unified picture of the adsorption of S_8 and Al_2S_n species, we directly correlated the electronic cause with the structural effect. As shown in Figure 4.6b, there is a relationship between the bader charge transfer and the similarity score. For instance, the Al_2S_3 species on Ni and Cu catalysts, which exhibit the largest charge loss (2.39 e and 2.40 e), also show the most significant deformation with the lowest similarity scores (6.38 and 6.32, respectively). Conversely, the Al_2S_6 species on Sc and Ti, which show the largest charge gain (-2.86 e and -2.61 e), also display considerable deformation with similarity scores of 8.65 and 8.78. This suggests that a large magnitude of charge transfer, regardless of direction, leads to the formation of strong chemical bonds that physically rearrange the structure of the adsorbed Al_2S_n species.

มหาวิทยาลัยเทคโนโลยีสุรนารี

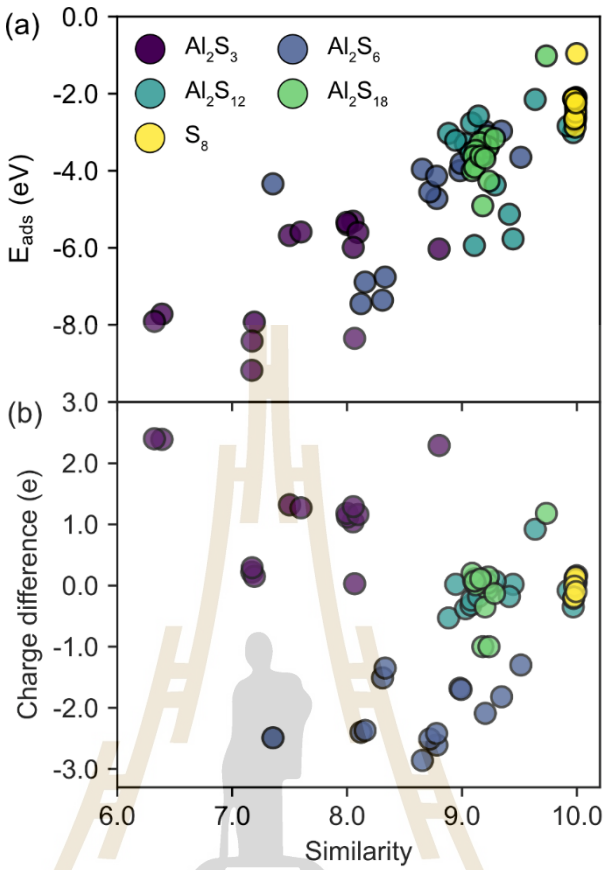


Figure 4.6 Correlation between the similarity value and the corresponding adsorption energy (E_{ads}) and charge difference for S_8 and Al_2S_n species across all surfaces. The species are color-coded as follows: S_8 (dark purple), Al_2S_{18} (medium blue), Al_2S_{12} (light green), Al_2S_6 (yellow-green), and Al_2S_3 (yellow).

In summary, this analysis suggests a logical narrative for the enhanced anchoring performance of the 3d-TM decorated V_2CO_2 surfaces. The bare suffers from a severe shuttle effect due to the weak adsorption strength. The 3d-TMs decorated systems with SA and DA catalysts show to be highly effective anchors for large, soluble polysulfides (Figure 4.4a). This superior performance seems to be driven by a strong intrinsic interaction (Figure 4.4b), which has a clear electronic origin in the form of significant charge transfer between the catalyst and the polysulfide (Figure 4.5). This adsorption strength comes with an energetic cost in the form of structural distortion, as indicated by the deformation energy analysis and directly causes a quantifiable physical deformation using similarity (Figure 4.6a). The adsorption of

Al_2S_n species tends to correlate charge transfer for several Al_2S_n species (Figure 4.6b). Next further step is to determine if they can also efficiently catalyze the electrochemical conversion of these S_8 and Al_2S_n species.

4.3 Gibbs free energy profiles of sulfur reduction reactions

The sulfur reduction reaction (SRR) in Al-S batteries plays a crucial role in determining the overall performance and efficiency of the batteries. To better understand the electrochemical behavior of Al-S batteries, we investigated the SRR mechanism by referencing analogous studies in Li-S batteries (L. Wang et al., 2022). In all systems, the catalytic properties of the electrode materials are critical for promoting the conversion of polysulfides during the charge-discharge process. Our previous analysis of adsorption and interaction energy highlighted the significant influence of V_2CO_2surfaces, especially when modified with SA or DA, on facilitating polysulfide conversions.

The SRR in Al-S batteries involves a sequence of electron-transfer reactions, wherein high orders of Al_2S_n are reduced stepwise to low order of Al_2S_n species with Al_2S_3 being the final discharge product. This multistep reduction process can be represented as a series of electron-transfer reactions, analogous to the mechanism in Li-S batteries. Each reaction step is accompanied by Gibbs free energy changes, which play a critical role in determining the overall kinetics and overpotential of the SRR. The mechanism and the overall SRR for Al-S batteries can be expressed through the following reaction steps:

$$3S_8 + \frac{4}{3} * + \frac{8}{3}(Al^{3+} + 3e^-) \rightarrow \frac{4}{3} Al_2S_{18}^* \quad (4.9)$$

$$\frac{4}{3} Al_2S_{18}^* + \frac{2}{3} * + \frac{4}{3}(Al^{3+} + 3e^-) \rightarrow 2Al_2S_{12}^* \quad (4.10)$$

$$2Al_2S_{12}^* + 2 * + 4(Al^{3+} + 3e^-) \rightarrow 4Al_2S_6^* \quad (4.11)$$

$$4Al_2S_6^* + 4 * + 8(Al^{3+} + 3e^-) \rightarrow 8Al_2S_3^* \quad (4.12)$$

$$8Al_2S_3^* \rightarrow 8Al_2S_3 + 8 * \quad (4.13)$$

$$3S_8 + 16Al^{3+} + 48e^- \rightarrow 8Al_2S_3 \quad (4.14)$$

The overpotential for SRR (η^{SRR}) is derived from the Gibbs free energy changes and the electron transfer involved in each step. The overpotential is calculated using the following expression:

$$\eta^{SRR} = -max\left(\frac{\Delta G_i}{N_i \cdot e}\right) + U_{eq} \quad (4.15)$$

where ΔG_i the Gibbs free energy change associated with step i, N_i is the number of electrons transferred in that step, e is the elementary charge, and U_{eq} is the theoretical equilibrium potential. In contrast to Li-S batteries, the theoretical equilibrium potential for SRR in Al-S systems is less straightforward to pinpoint due to the multiple discharge steps. We estimated the equilibrium potential to be approximately 0.83 V, based on this number divided by the standard Gibbs free energy (-39.96 eV) of Al_2S_3 formation, and used this value in our overpotential calculations.

$$\Delta G_f^0 = 8G(Al_2S_{3\,bulk})^0 - 3G(S_{8\,bulk})^0 - 3G(Al_{atom})^0 \quad (4.16)$$

We computed the Gibbs free energy profiles for SRR including bare, SA@V_2CO_2, and DA@V_2CO_2. At U = 0 V and U = 0.83 V (equilibrium potential), the Gibbs free energy values for the reduction of Al_2S_n species are summarized in Table A1.

On the bare V_2CO_2 surface, there are some endothermic steps at equilibrium potential as shown in Figure 4.7. It indicates that the bare surface struggles to convert from the solid S_8 to the liquid Al_2S_{18} and liquid Al_2S_{12} to solid Al_2S_6. Furthermore, the negative Gibbs free energy for the non-electron step (-2.35 eV) is thermodynamically unfavorable while the overall SRR is thermodynamically favorable. The non-electron step, which is the Al_2S_3 desorption, faces significant energy barriers that slow down the overall reaction kinetics.

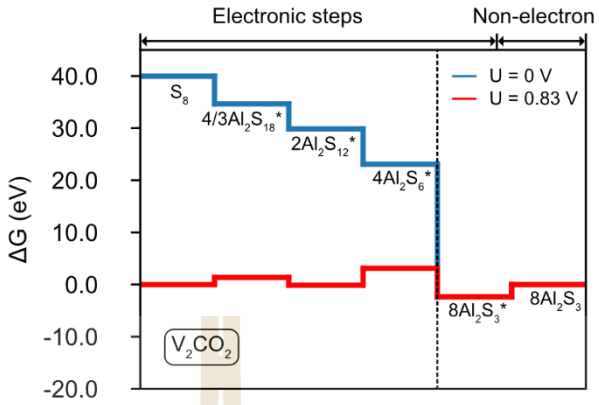


Figure 4.7 Sulfur reduction reaction (SRR) performance of the bare V_2CO_2. Gibbs free energy diagram of SRR for V_2CO_2. at U = 0 V and equilibrium potential (U = 0.83 V).

When SA are introduced on the V_2CO_2 surface, we observed notable improvements in SRR process in Figure 4.8. The conversion from the solid S_8 to the liquid Al_2S_{18} becomes more thermodynamically stable. Some SAs reduce the thermodynamic barriers associated with the conversion from the liquid Al_2S_{12} to the solid Al_2S_6 and promote the Al_2S_3 desorption. For example, in $Cr@V_2CO_2$, the liquid Al_2S_{18} to the solid Al_2S_6 has lower thermodynamic barrier (2.91 eV) compared to the bare (3.24 eV). While the Al_2S_3 desorption is thermodynamically favorable.

For the $Sc@V_2CO_2$, the Gibbs free energy for the conversion from the solid S_8 to the liquid Al_2S_{18} decreases to -1.21 eV However, the conversion from liquid Al_2S_{12} to solid Al_2S_6 remains thermodynamically unfavorable. In the $Sc@V_2CO_2$, the Gibbs free energy for from liquid Al_2S_{12} to solid Al_2S_6 is reduced to 4.17 eV. The Al_2S_3 desorption, however, shows a positive Gibbs free energy (6.03 eV), which could hinder the complete SRR of sulfur species at the equilibrium potential. The $Ti@V_2CO_2$ also shows reduced energy barriers, with a Gibbs free energy of -2.38 eV for Al_2S_{12} and 1.78 eV for Al_2S_6, indicating better catalytic activity than the bare surface.

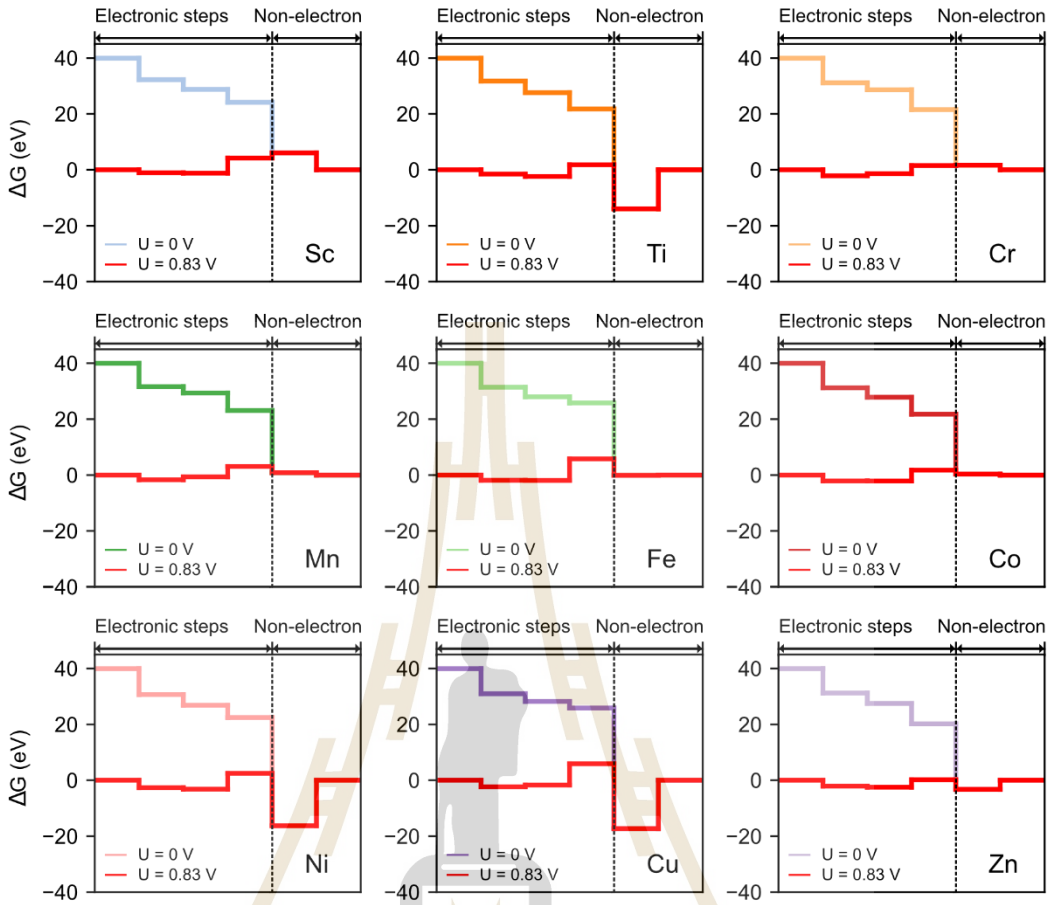


Figure 4.8 SRR performance of 3d-TMs as SA@V_2CO_2. Gibbs free energy diagram of the sulfur reduction reaction (SRR) for SA@V_2CO_2 at U = 0 V and at the equilibrium potential (U = 0.83 V). The diagram illustrates the energy profiles and highlights the impact of different 3d-transition metals on SRR performance.

Our results show that DA@V_2CO_2 significantly improved the conversion of S_8 and higher order of Al_2S_n compared the bare and SA systems. For instance, in the d-Cr-no@V_2CO_2, the Gibbs free energy for the conversion from solid S_8 to liquid Al_2S_{18} is reduced to -4.36 eV, while for liquid Al_2S_{12} to solid Al_2S_6 is -14.67 eV, indicating a highly favorable reaction shown in Figure 4.9. Similarly, in the d-Mn-vo@V_2CO_2, the conversion from solid S_8 to liquid Al_2S_{18} and liquid Al_2S_{12} to solid Al_2S_6 are -5.15 eV and -12.67 eV, respectively. These results demonstrate that DA systems offer superior performance in promoting the electronic steps during the SRR process.

Despite their excellent performance in polysulfide conversion, DA@V_2CO_2 encounter significant challenges in the Al_2S_3 desorption. The Gibbs free energy for

Al_2S_3 desorption in DA systems is highly negative, such as -26.12 eV in the d-Mn-vo@V_2CO_2, suggesting that Al_2S_3 is too strongly adsorbed to the DA-modified surface. Furthermore, the V_O in DA systems including d-Cr-V_O and d-Mn-V_O provide stronger adsorption strength compared to non-vacancy systems. This excessive adsorption strength leads to thermodynamically unfavorable desorption, which can hinder the overall reversibility of the battery.

Our similarity analysis and deformation energy calculations indicate significant structural changes in the adsorbed Al_2S_3 species, exacerbating the desorption issue. The distortion arises from the strong interaction between Al_2S_3 and the dual active sites provided by the DA catalysts, which stabilizes the polysulfides but hinders the desorption of the final sulfur product.

In contrast, the SA@V_2CO_2 and the bare V_2CO_2 surface do not perform as well in the conversion of higher orders of Al_2S_n. However, these systems show more favorable desorption for Al_2S_3. This implies to the weaker adsorption strength in SA and bare systems allows for easier desorption of Al_2S_3.

We also considered the limiting potential and overpotential, following the methodology used for ORR and other metal–sulfur batteries. Despite improvements in the phase transition steps for SA systems, we observed high overpotentials in several cases, as shown in Figure 4.10a This finding suggests that the conversion of liquid Al_2S_{12} to solid Al_2S_6 is the critical step for evaluating catalytic performance. In contrast, DA systems display the highest limiting potential.

Recognizing the importance of the liquid Al_2S_{12} to solid Al_2S_6 transition, we further investigated the stronger interactions lead to better SRR catalytic performance, as these species act as bridges for the liquid–solid transition during SRR. Our findings emphasize the importance of the relationship between the adsorption strength of Al_2S_n (n = 12 and 6) species and the SRR overpotential. Our results show a linear correlation between the interaction energy of Al_2S_{12}/Al_2S_6 and the SRR overpotential, as illustrated in Figure 4.10b. Clearly accelerating the conversion from liquid Al_2S_{12} to solid Al_2S_6 throughout the entire reaction process. Overall, our study reveals the dominant role of Al_2S_6 adsorption strength in determining SRR catalytic

performance, providing theoretical guidance for the rapid screening of efficient SRR catalysts.

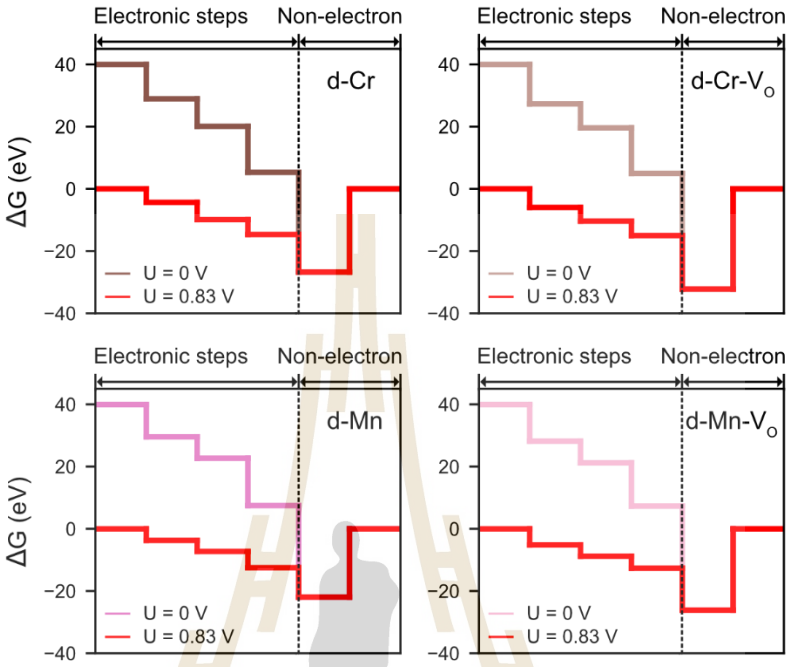


Figure 4.9 SRR performance of 3d-TMs as DA@V_2CO_2 surfaces. Gibbs free energy diagram of the sulfur SRR for DA@V_2CO_2 at U = 0 V and at the equilibrium potential (U = 0.83 V).

In summary, this analysis suggests that the bare surface struggles to convert from the solid S8 to the liquid Al_2S_{18} and from liquid Al_2S_{12} to solid Al_2S_6, and is thermodynamically unfavorable for Al_2S_3 desorption. The 3d-TM decorated systems with SAs show improvement in the S_8 to liquid Al_2S_{18} step due to the stronger adsorption strength for Al_2S_{18}. However, we find that SAs still struggle to convert liquid Al_2S_{12} to solid Al_2S_6, despite thermodynamically favorable Al_2S_3 desorption. Among SA@V_2CO_2, only Cr@V_2CO_2 shows a lower overpotential than that of the bare surface. In the case of DAs, there are no energy barriers for electronic steps, indicating no overpotential. Unfortunately, DAs face a critical challenge in Al_2S_3 desorption. Thus, we need to further investigate the decomposition of Al_2S_3, since this is an important step for the reversible process of Al-S batteries.

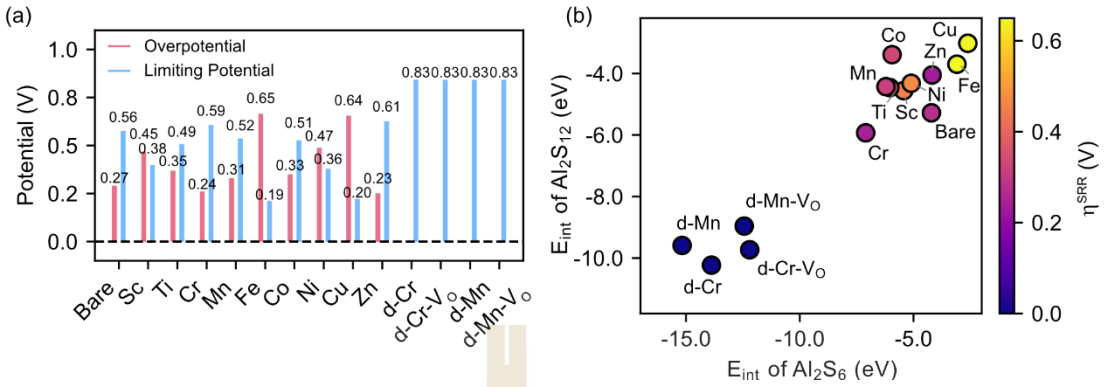


Figure 4.10 (a) A comparison of the calculated limiting potential and overpotential (ηSRR) across all catalyst systems. (b) The relationship between the interaction energy (E_{int}) of Al_2S_{12} and Al_2S_6 and the calculated ηSRR on the bare, SA, and DA systems.

4.4 Decomposition of Al_2S_3

The decomposition of Al_2S_3 is a crucial step in the SRR and the overall charge–discharge process of Al–S batteries. Effective decomposition ensures the battery's reversibility and directly affects the stability and efficiency of the electrochemical cycle. In this study, we investigated the breaking of S and Al atoms (only Al for DA systems), as the decomposition of Al_2S_3 requires the cleavage of both elements. This process begins with the dissociation of the S atom from Al_2S_3. Subsequently, the remaining Al atom is released from Al_2S_2 once the S atom has fully dissociated, as illustrated in Figure 4.11a.

The all-decomposition pathway of Al_2S_3 is presented in Figure A9. We found that S breaking in Al_2S_3 occurs rapidly, making it difficult to identify a transition state due to the swift nature of the reaction pathway. On V_2CO_2, the decomposition of Al_2S_3 is endothermic, with a high energy barrier indicating that both Al and S atoms struggle to dissociate from Al_2S_3. In Figure 4.11b, we found that Al breaking is a less favorable step than S breaking. For SA systems, we focused on Cr and Mn, as these single atoms exhibited the best SRR performance.

The introduction of Cr and Mn significantly enhances the decomposition process of Al_2S_3. The presence of SAs lowers the energy barrier for Al breaking, even

though the barrier for S breaking in Mn and Cr is slightly higher than that of the bare surface. For DA systems, both Cr and Mn significantly enhance the decomposition of Al_2S_3, with the most favorable reaction pathways observed in d-Cr-no and d-Cr-vo. We also observed Brønsted-Evans-Polanyi (BEP) relation between the reaction energy and the energy barrier, as shown in Figure 4.11c. Notably, Cr demonstrates impressive performance in both SA and DA systems.

We also analyzed the Integrated Crystal Orbital Hamilton Population (ICOHP) values of key bonds involved in the Al_2S_3 decomposition pathway in Figure A10. ICOHP provides a quantitative measure of bonding interactions, where more negative values indicate stronger bonds. We found out that the quantitative measure cannot directly examine the key bonds in the decomposition of Al_2S_3 since the complexity of optimized Al_2S_3 configuration on the different systems.

มหาวิทยาลัยเทคโนโลยีสุรนารี

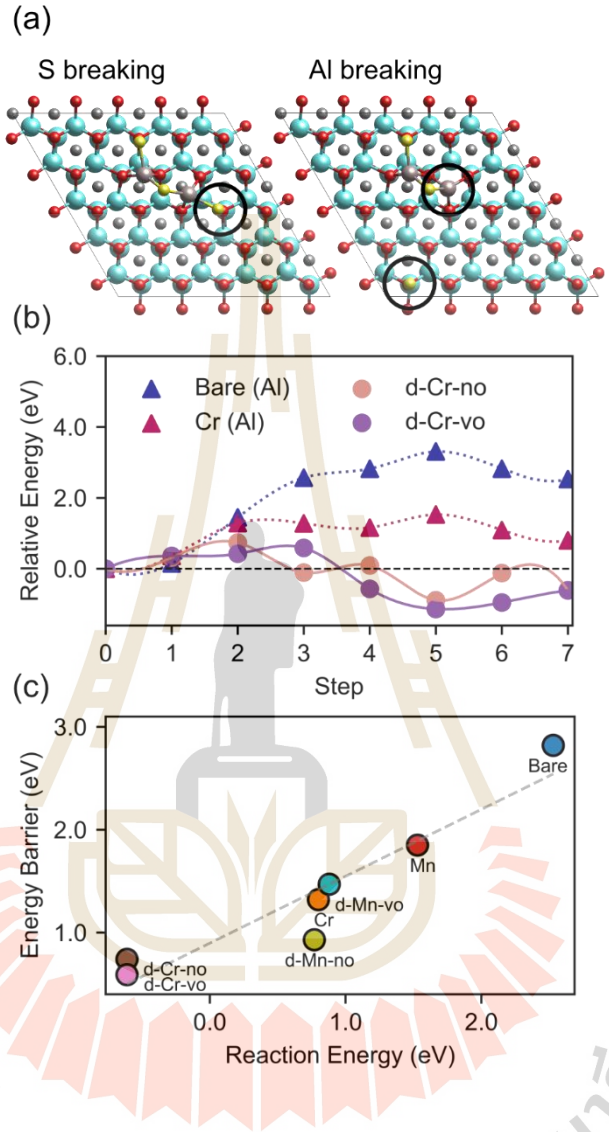


Figure 4.11 The decomposition of Al_2S_3 on bare, $Cr@V_2CO_2$, and Mn and $Cr-@V_2CO_2$ with and without V_O. (a) Schematic of S breaking and Al breaking. (b) The relative corresponding of energy with the decomposition step of Al_2S_3 in each system. (c) The correlation between energy barrier and reaction energy.

4.5 References

Andritsos, E. I., Lekakou, C., & Cai, Q. (2021). Single-Atom Catalysts as Promising Cathode Materials for Lithium–Sulfur Batteries. *The Journal of Physical Chemistry C*, *125*(33), 18108–18118.

Bhauriyal, P., & Pathak, B. (2020). Superior anchoring effect of a Cu-benzenehexathial MOF as an aluminium–sulfur battery cathode host. *Materials Advances*, *1*(9), 3572–3581.

Chen, Y.-H., Qi, M.-Y., Li, Y.-H., Tang, Z.-R., Wang, T., Gong, J., & Xu, Y.-J. (2021). Activating two-dimensional $Ti_3C_2T_x$-MXene with single-atom cobalt for efficient CO_2 photoreduction. *Cell Reports Physical Science*, *2*(3), 100371.

Gao, P., Song, M., Wang, X., Liu, Q., He, S., Su, Y., & Qian, P. (2022). Theoretical Study on the Electronic Structure and Magnetic Properties Regulation of Janus Structure of M'MCO_2 2D MXenes. *Nanomaterials*, *12*(3).

Gu, J., Zhu, Q., Shi, Y., Chen, H., Zhang, D., Du, Z., & Yang, S. (2020). Single Zinc Atoms Immobilized on MXene ($Ti_3C_2Cl_x$) Layers toward Dendrite-Free Lithium Metal Anodes. *ACS Nano*, *14*(1), 891–898.

Ju, S., Yuan, C., Zheng, J., Yao, L., Zhang, T., Xia, G., & Yu, X. (2022). Identifying single-atom catalysts for boosted Al–S conversion reactions. *Energy Storage Materials*, *52*, 524–533.

Singsen, S., Fongkaew, I., Hirunsit, P., & Suthirakun, S. (2022). Suppressing Polysulfides Shuttling and Promoting Sulfur Utilization via Transition Metal and Nitrogen Co-Doping on Graphdiyne Cathodes of Lithium-Sulfur Batteries: A First-Principles Modeling. *ACS Applied Energy Materials*, *5*(8), 9722–9732.

Wang, L., Hu, Z., Wan, X., Hua, W., Li, H., Yang, Q. H., & Wang, W. (2022). Li2S4 Anchoring Governs the Catalytic Sulfur Reduction on Defective SmMn2O5 in Lithium–Sulfur Battery. *Advanced Energy Materials*, *12*(20).

Wang, Z., Zheng, X., Chen, A., Han, Y., Wei, L., & Li, J. (2022). Unraveling the Anchoring Effect of MXene-Supported Single Atoms as Cathodes for Aluminum–Sulfur Batteries. *ACS Materials Letters*, *4*(8), 1436–1445.

Yang, X.-F., Wang, A., Qiao, B., Li, J., Liu, J., & Zhang, T. (2013). Single-Atom Catalysts: A New Frontier in Heterogeneous Catalysis. *Accounts of Chemical Research*, *46*(8), 1740–1748.

Zheng, X., Wang, Z., Li, J., & Wei, L. (2022). Binder-free S@$Ti_3C_2T_x$ sandwich structure film as a high-capacity cathode for a stable aluminum-sulfur battery. *Science China Materials*, *65*(6), 1463–1475.

Zou, F., Cong, Y., Song, W., Liu, H., Li, Y., Zhu, Y., Zhao, Y., Pan, Y., & Li, Q. (2024). Interfacial Properties of Anisotropic Monolayer SiAs Transistors. *Nanomaterials*, *14*(3).

มหาวิทยาลัยเทคโนโลยีสุรนารี

CHAPTER V
CONCLUSIONS

In this study, we employed first-principles DFT calculations to systematically investigate the potential of 3d-transition metal atoms, as both SA and DA, decorated on V_2CO_2 as cathode materials for Al-S batteries. Our findings demonstrate that modifying the V_2CO_2 surface with these atomic catalysts is a crucial and highly effective strategy for addressing the critical challenges that hinder Al-S battery performance, including the shuttle effect, sluggish sulfur reduction reaction (SRR), and the decomposition of Al_2S_3.

Our analysis of adsorption strength reveals a clear performance for anchoring the soluble, high-order Al_2S_n species: Bare V_2CO_2 < SA@V_2CO_2 < DA@V_2CO_2. The bare surface exhibits only weak adsorption strength for Al_2S_{18}, which is insufficient to prevent polysulfide dissolution into the electrolyte. In contrast, the DA systems with V_O like d-Cr-vo@V_2CO_2, show strong adsorption strength. We observed that strong interaction is accompanied by a high energetic penalty. This interaction is governed by significant charge transfer, as quantified by Bader analysis, and results in structural deformation of the Al_2S_n species, confirmed by low similarity scores.

Furthermore, the Gibbs free energy profiles for the SRR show that DA systems show a better catalytic performance. The bare surface and most SA systems suffer from high overpotentials because the critical liquid-to-solid transition ($Al_2S_{12} \longrightarrow Al_2S_6$) is thermodynamically challenging. We identified a strong linear correlation across all systems: catalysts with stronger interaction energies for Al_2S_{12} and Al_2S_6 relate with lower SRR overpotentials, suggesting strong adsorption is key to catalysis.

However, this adsorption strength in DA systems presents a critical trade-off for Al_2S_3 desorption. However, CI-NEB analysis of the Al_2S_3 decomposition shows that DA systems like d-Cr-V_O@V_2CO_2 significantly lower the energy barrier for the cleavage of Al-S bonds. The results show BEP relation between reaction energy and barriers. This

suggests DA system is highly effective at decomposing Al_2S_3, which is the important step for the reversibility process.

In summary, d-Cr@V_2CO_2 and d-Cr-V_O@V_2CO_2, are identified as the most promising candidates, solving both the shuttle effect via strong anchoring and the sluggish via superior catalysis. The primary remaining challenge is balancing this high activity with the need for efficient product desorption to ensure long-term reversibility

มหาวิทยาลัยเทคโนโลยีสุรนารี

APPENDICES

มหาวิทยาลัยเทคโนโลยีสุรนารี

APPENDIX A

THE CONFIGURATION AND PROPERITES FOR 3D-TRANSITION METAL ATOMS DECORATED V_2CO_2

A.1 Optimization of different structures for V_2CO_2 surface

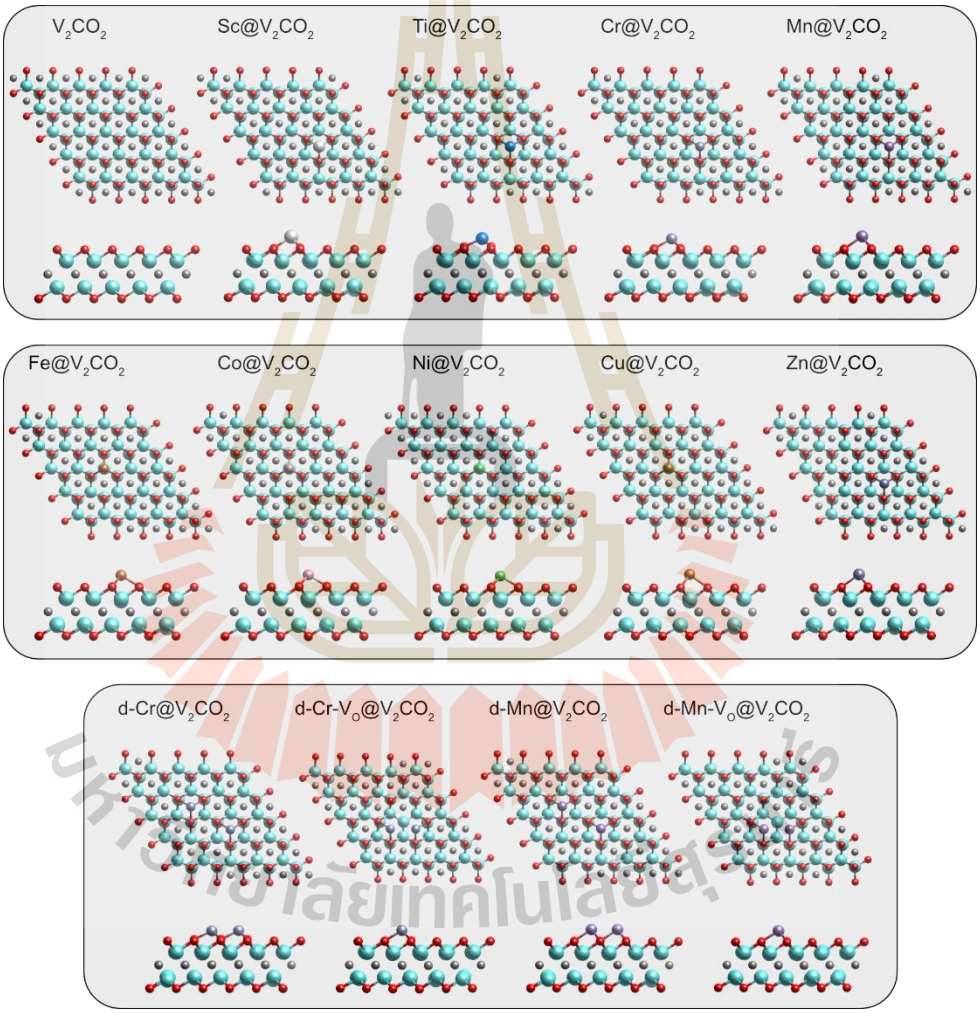


Figure A1 Optimized structures of the V_2CO_2 surface, SA@V_2CO_2 and DA@V_2CO_2.

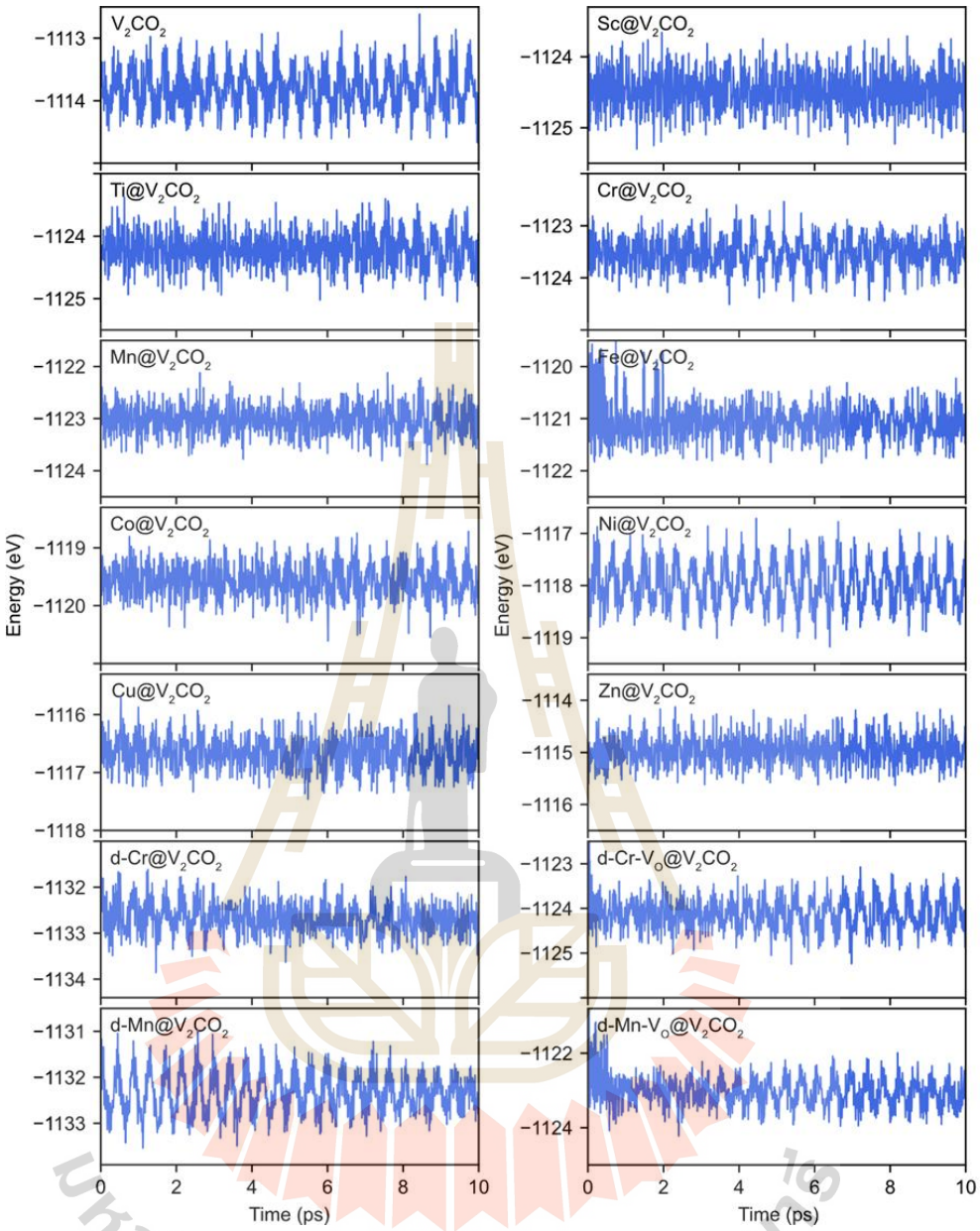


Figure A2 The fructuation of total energy as a function of time along AIMD simulation at 300 K and corresponding initial and final configurations of bare, SA@V_2CO_2, and DA@V_2CO_2, a method used in similar a computational study (Singsen et al., 2022).

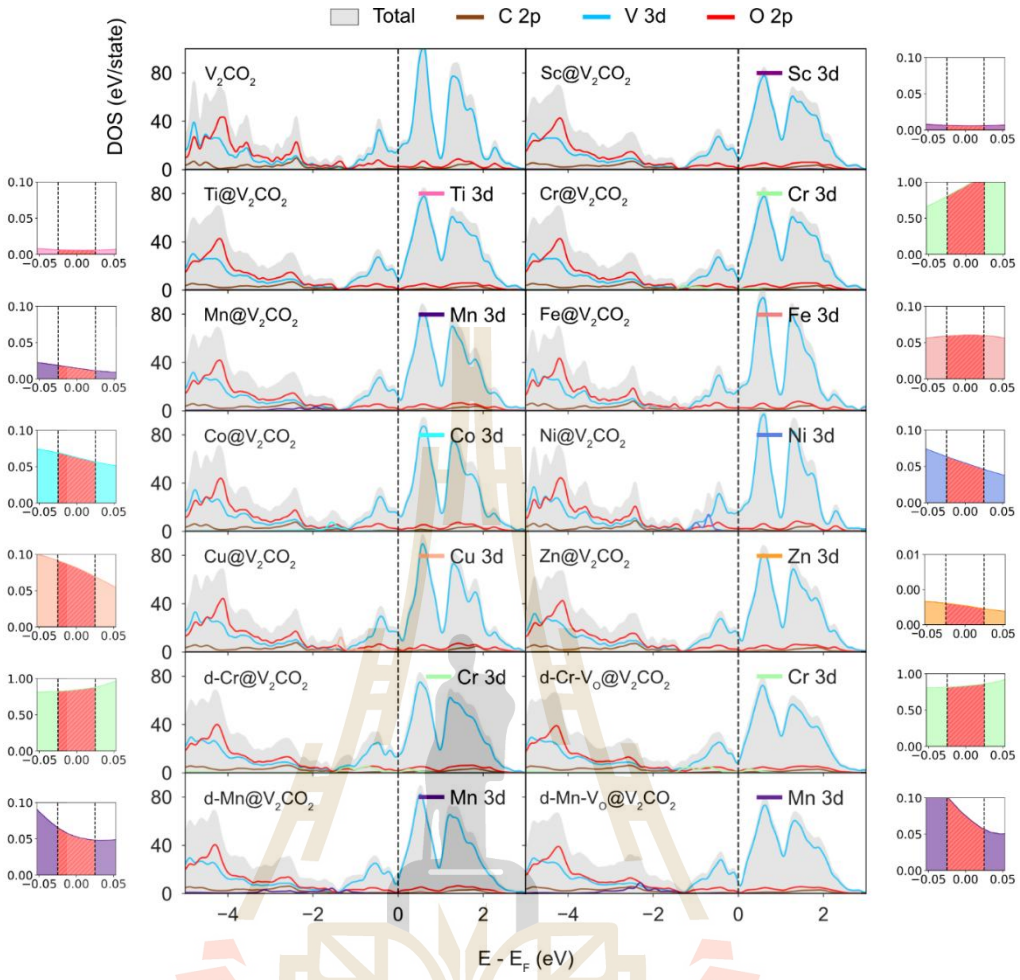


Figure A3 Projected Density of States (PDOS) for the bare, SA@V_2CO_2, and DA@V_2CO_2.

มหาวิทยาลัยเทคโนโลยีสุรนารี

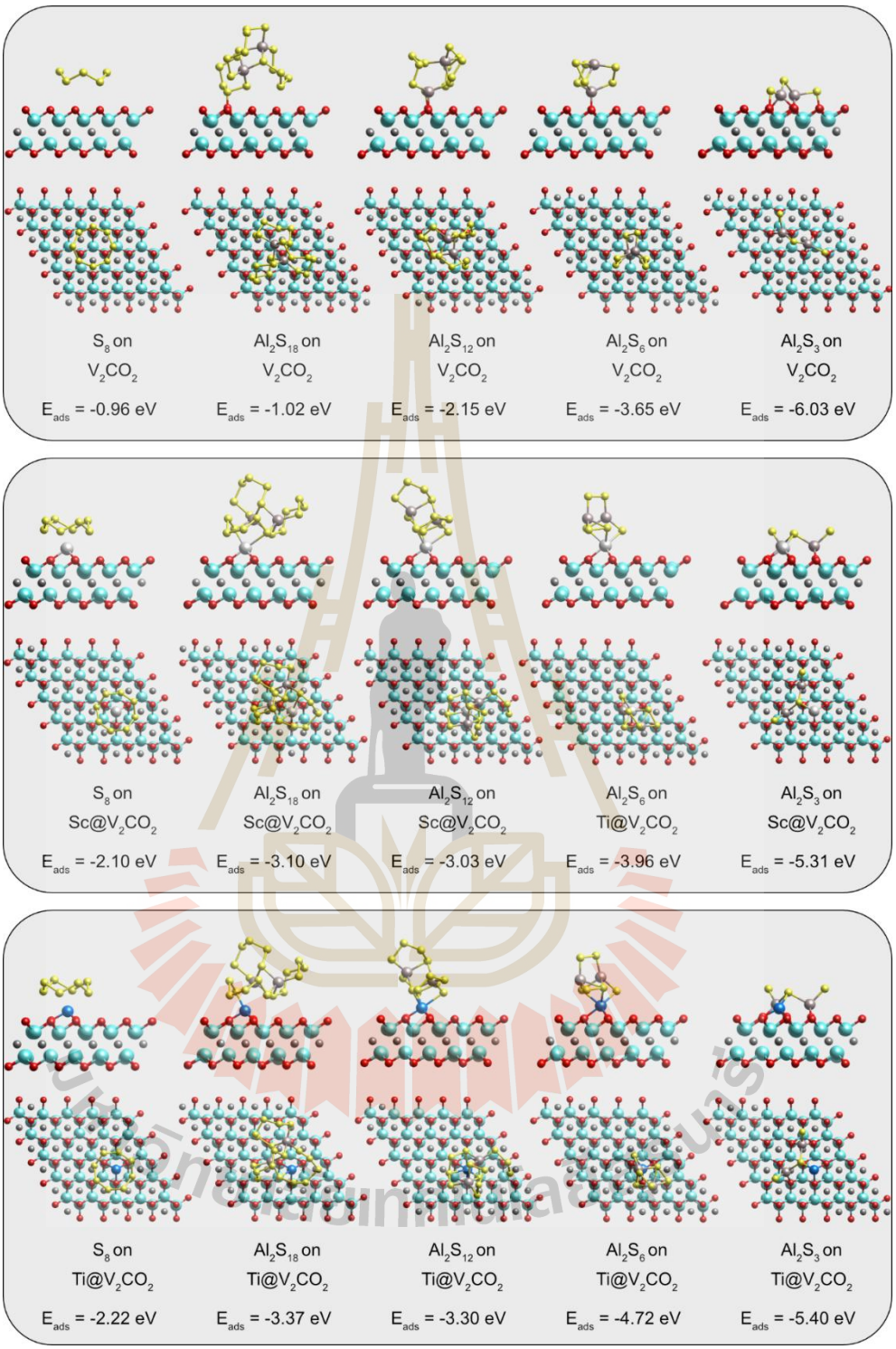


Figure A4 Optimized structures and adsorption energy of S_8 and Al_2S_n speices on V_2CO_2, $Sc@V_2CO_2$, and $Ti@V_2CO_2$.

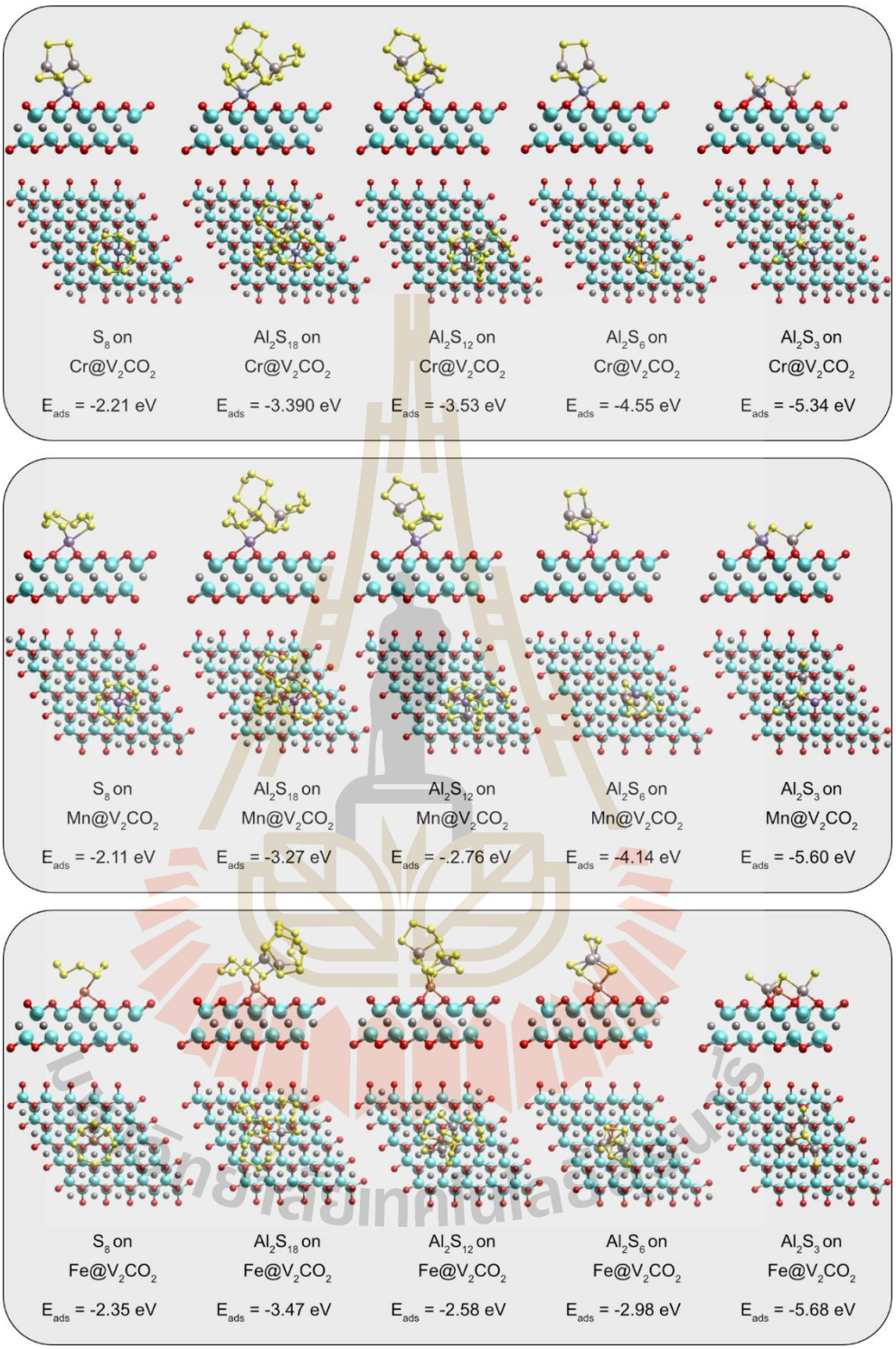


Figure A5 Optimized structures and adsorption energy of S_8 and Al_2S_n speices on $Cr@V_2CO_2$, $Mn@V_2CO_2$, and $Fe@V_2CO_2$.

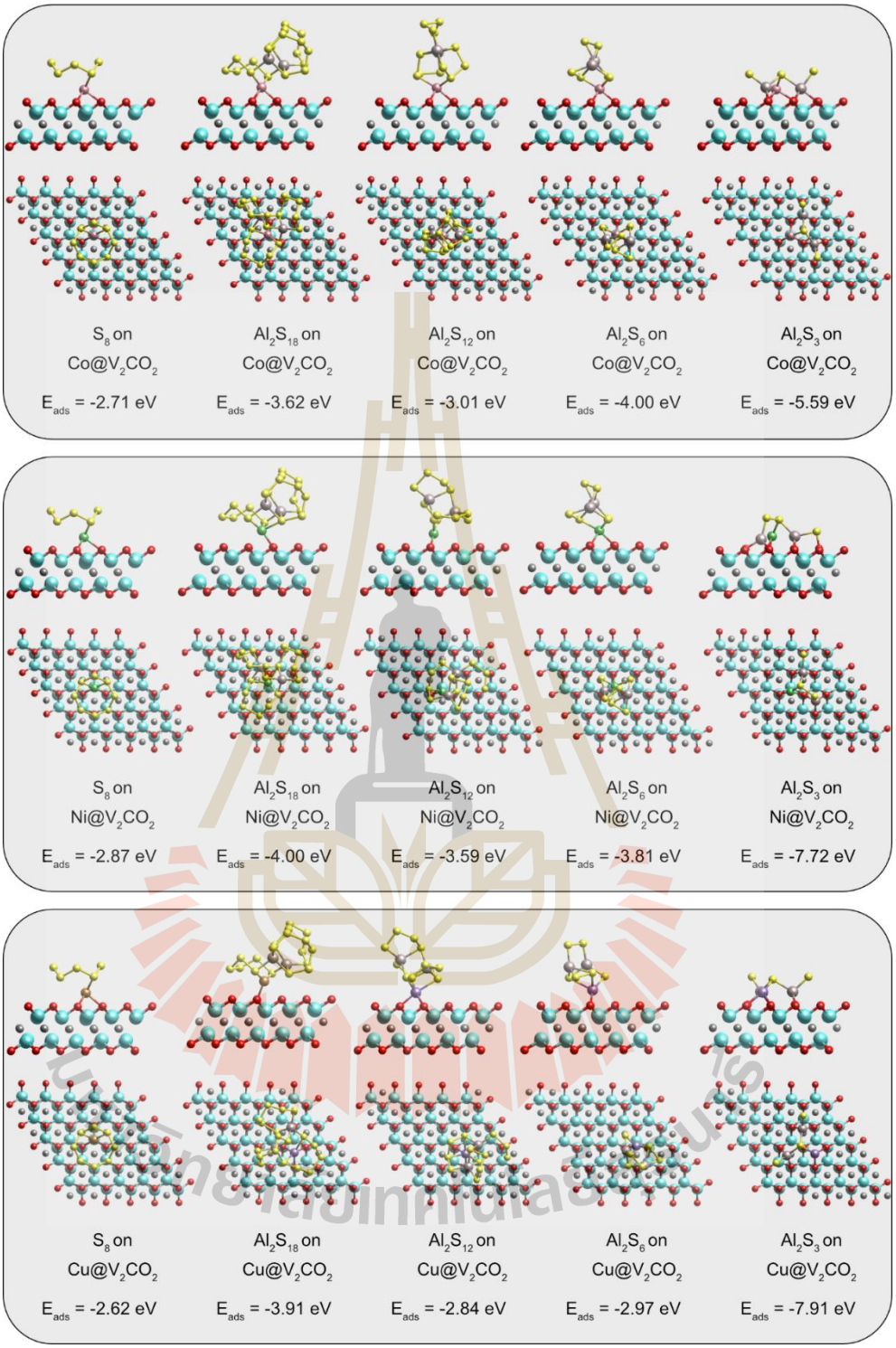


Figure A6 Optimized structures and adsorption energy of S_8 and Al_2S_n speices on $Co@V_2CO_2$, $Ni@V_2CO_2$, and $Cu@V_2CO_2$.

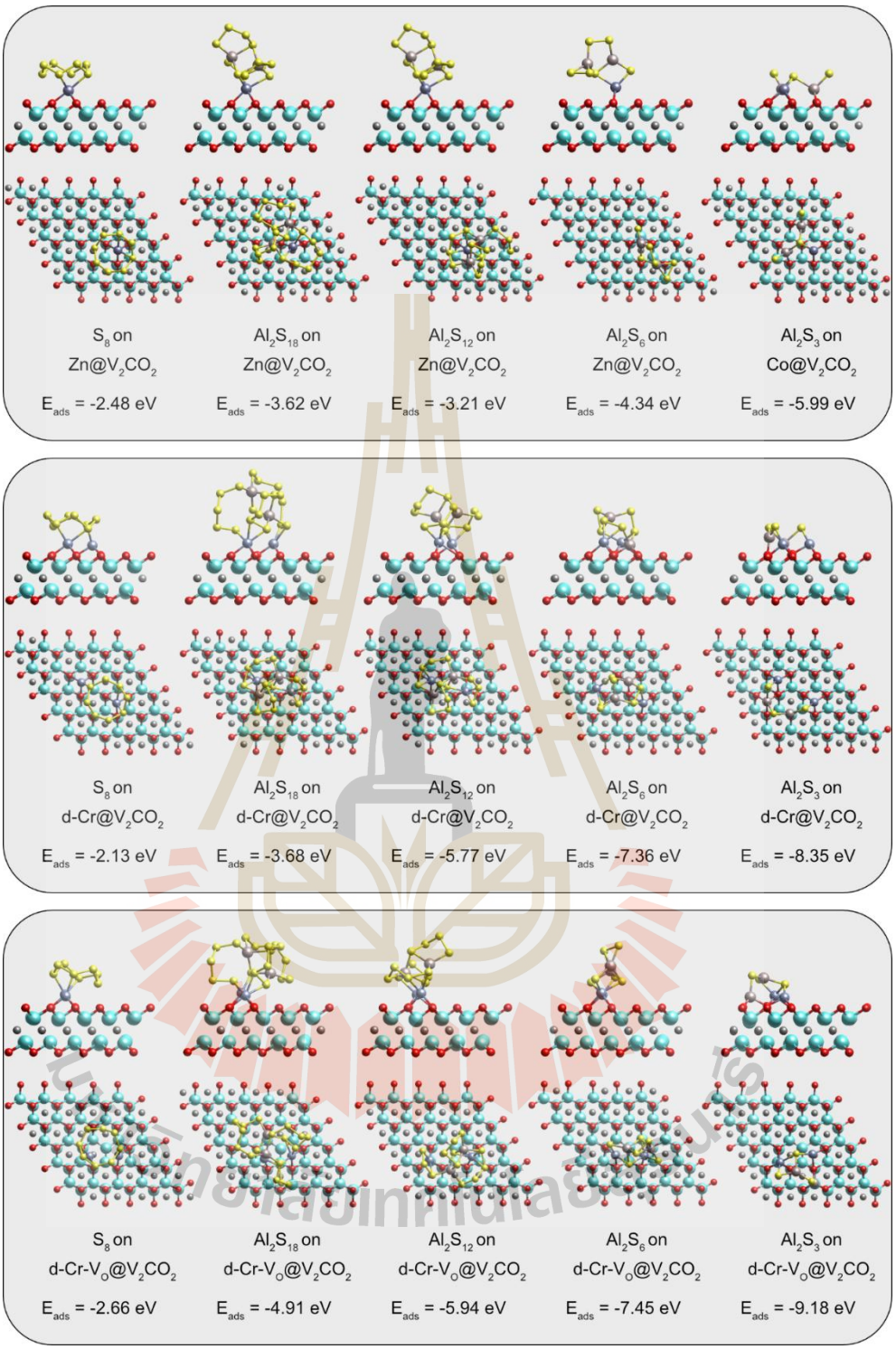


Figure A7 Optimized structures and adsorption energy of S_8 and Al_2S_n speices on $Zn@V_2CO_2$, $d\text{-}Cr@V_2CO_2$, and $d\text{-}Cr\text{-}V_O@V_2CO_2$.

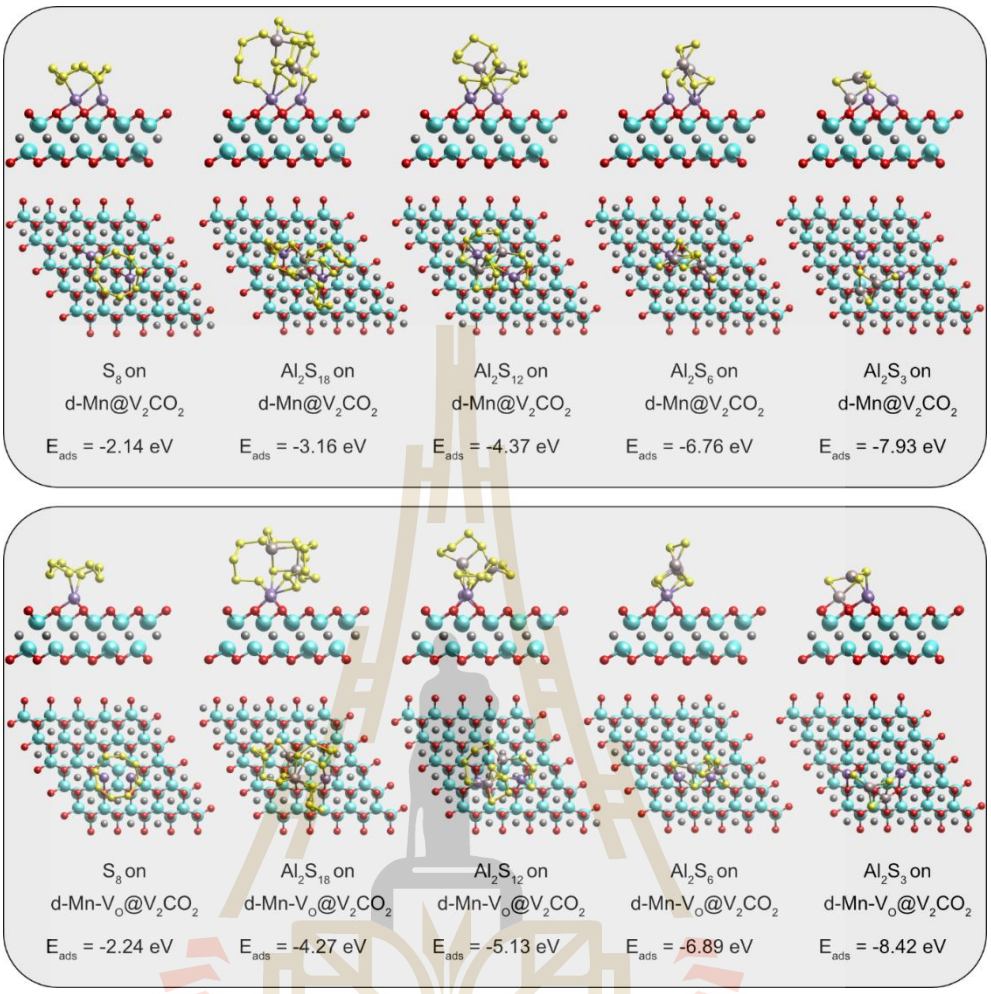


Figure A8 Optimized structures and adsorption energy of S_8 and Al_2S_n speices on d-d-Mn@V_2CO_2, and d-Mn-V_O@V_2CO_2.

มหาวิทยาลัยเทคโนโลยีสุรนารี

A.2 Sulfur reduction reactions and decomposition of Al_2S_3 for V_2CO_2 surface

Table A1 Gibbs free energy values for the reduction of S_8 and Al_2S_n species at U = 0.83 V (equilibrium potential).

Surfaces	S_8	Al_2S_{18}*	Al_2S_{12}*	Al_2S_6*	Al_2S_3*	Al_2S_3
Bare	0.00	1.37	-0.13	3.11	-2.35	0.00
Sc	0.00	-1.08	-1.21	4.17	6.03	0.00
Ti	0.00	-1.53	-2.38	1.78	-13.98	0.00
Cr	0.00	-2.16	-1.36	1.55	1.66	0.00
Mn	0.00	-1.67	-0.63	3.08	0.83	0.00
Fe	0.00	-1.88	-1.95	5.81	-0.10	0.00
Co	0.00	-2.12	-2.13	1.78	0.30	0.00
Ni	0.00	-2.62	-3.16	2.49	-16.28	0.00
Cu	0.00	-2.36	-1.73	5.91	-17.28	0.00
Zn	0.00	-2.07	-2.49	0.22	-3.22	0.00
d-Cr	0.00	-4.36	-9.89	-14.67	-26.71	0.00
d-Cr-V_O	0.00	-5.97	-10.37	-15.05	-32.21	0.00
d-Mn	0.00	-3.70	-7.26	-12.50	-21.93	0.00
d-Mn-V_O	0.00	-5.15	-8.79	-12.67	-26.12	0.00

มหาวิทยาลัยเทคโนโลยีสุรนารี

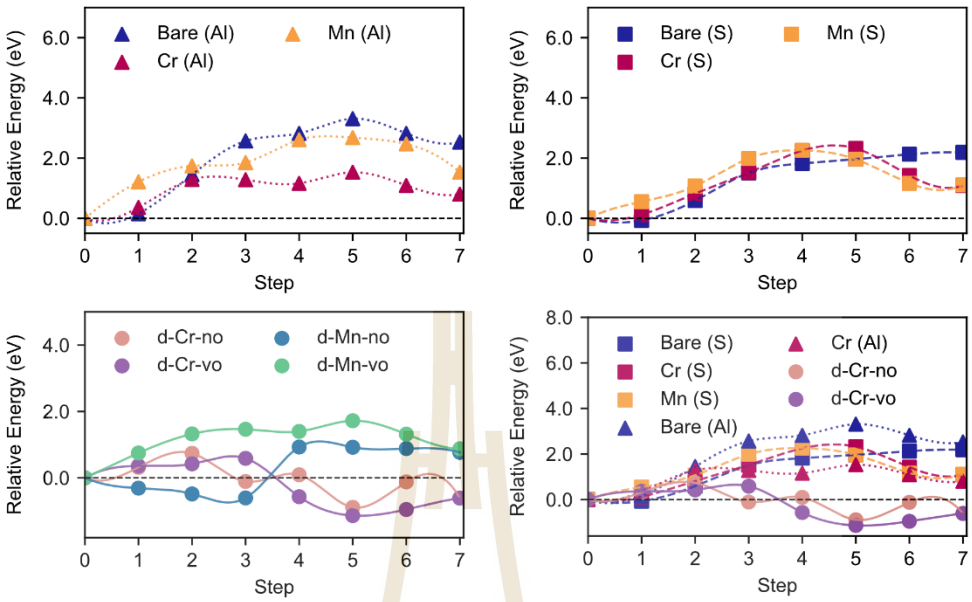


Figure A9 The decomposition of Al_2S_3 on bare, SA@V_2CO_2 including Cr, and Mn and DA@V_2CO_2 with and without V_O including Cr and Mn.

Reference

Singsen, S., Fongkaew, I., Hirunsit, P., & Suthirakun, S. (2022). Suppressing Polysulfides Shuttling and Promoting Sulfur Utilization via Transition Metal and Nitrogen Co-Doping on Graphdiyne Cathodes of Lithium-Sulfur Batteries: A First-Principles Modeling. *ACS Applied Energy Materials*, *5*(8), 9722–9732.

มหาวิทยาลัยเทคโนโลยีสุรนารี

APPENDIX B

PUBLICATION AND PRESENTATIONS

B.1 List of publication

Rattanaumpa, T., Panbo, P., Suthirakun, S., Kaewket, K., Wijitsak, J., Pinyou, P., and Ngamchuea, K. (2024). Catalysis of Oxygen Reduction Reaction by Iron Porphyrin and Its Sensing Application. J. Electroanal. Chem. 973: 118647.

B.2 List of presentation

Panbo, P., Kaewraung, W., K., Junkaew, A., and Suthirakun, S. (2024). First-Principles Study on the Performance of Single-Atom Supported V_2CO_2 as Cathode Materials of Aluminum-Sulfur Batteries. **The 27th International Annual Symposium on Computational Science and Engineering 2024 (ANSCSE27).** 30 July - 3 August 2024, Department of Chemical Engineering, Faculty of Engineering, Chulalongkorn University, Thailand. (Oral presentation)

มหาวิทยาลัยเทคโนโลยีสุรนารี

CURRICULUM VITAE

Pakuna Panbo was born in Nakhon Si Thammarat, Thailand, on January 14, 2000. He received his B.Sc. in Science (first-class honors) in 2022 from the School of Science, Institute of Science, Walailak University, Thailand. He has been a recipient of a scholarship from the Development and Promotion of Science and Technology Talents Project (DPST) since 2016. During his senior year of his bachelor's degree, his research focused on investigating the hydrogen bond formations of polybenzoxazines using molecular dynamics simulation, under the supervision of Assoc. Prof. Dr. Apirak Payaka. During his undergraduate studies, he also published three international articles. In 2023, he began his master's degree program at the School of Chemistry, Institute of Science, Suranaree University of Technology, Thailand, supported by his DPST scholarship. Under the supervision of Assoc. Prof. Dr. Suwit Suthirakun, his research interest is in density functional theory for materials investigation. He has published articles in international journals and participated in international conferences during his master's program.

มหาวิทยาลัยเทคโนโลยีสุรนารี